Self-Assembly and Manipulation of Nanorod Arrays through Liquid Crystal Functionalization

By

Xiang Feng

A thesis submitted to the Faculty of Graduate Studies of
The University of Manitoba
in partial fulfilment of the requirements for the degree of

MASTER OF SCIENCE

Department of Chemistry
Faculty of Science
University of Manitoba
Winnipeg

Abstract

Self-assembly of nanorods (NRs) enhanced by functionalization with liquid crystals (LC) ligands has been demonstrated.

First, CTAB (cetyltrimethylammonium bromide) coated gold NRs were prepared in water through a modified one-step seed growth process. The hydrophilic GNRs were then converted into hydrophobic NRs employing a surface modification process using liquid crystalline organosilanes.

The functionalized GNRs were characterized by TEM (transmission electron microscopy) and SAXS (small angle X-ray scattering) to investigate the packing mode of the GNRs. The results propose models of the assembly of the GNRs depending on nature and connectivity of the attached liquid crystal molecules. Furthermore, a macroscopic orientation of the GNRs doped in LC was achieved via an alignment technique of the liquid crystal host. SAXS analysis of the doped DLC indicated modification of lattice parameters due to the insertion of the DLC-GNRs, which resulted in an enhancement of the charge carrier mobility.

Acknowledgments

This work would not have been possible without the help of many individuals.

First and foremost, I would like to express my heartfelt gratitude to my supervisor Dr. Torsten Hegmann for all the opportunities, trust, guidance and support. I thank my advisory committee members, Drs. Torsten Hegmann, Michael Freund, Philip Hultin from the Department of Chemistry and Derek Oliver from the Department of Electrical & Computer Engineering, for their valuable inputs during the whole period of my study. I thank Dr. Douglas Thomson from the Department of Electrical & Computer Engineering for the help of discussions during the nano-solar group meetings.

I thank former PDFs in the Hegmann group, Drs. Oana Stamatoiu and Umadevi Shivakumar, who worked together with me on this research project. I learned a lot from their persistent pursuit of science and knowledge, cautiously optimistic personalities and brilliant thoughts. I thank all the other Hegmann group members, Javad Mirzaei, Anshul Sharma, Matt Worden and former members Dr. Vinith Yathindranath, Dr. Ganesh Vankatchalam and Dr. Hao Qi for all their help, support, and wonderful time that we spent together. I thank Mr. Andre Dufresne from the Department of Biological Science for his long-term support for obtaining those nice TEM images. I thank Dr. Kevin McEleney for the assistance of SAXS operation and data processing and discussions. I thank the department head Dr. Peter Budzelaar, the former associate head Dr. Helene Perreault, the

graduate chair Dr. Jennifer van Wijngaarden, the office staffs (Mr. Keith Travis, Ms. Sharon Mullen, and Ms. Tricia Lewis) for their help and support. I thank Dr. David Herbert for letting me use his lab space and join his group meetings.

Finally, I thank my parents for their love and support throughout, and my gratitude goes to all my family and friends.

Contents

List of Tables

List of Figures

List of Copyrighted Material

1. S. Eustis, M. A. El-Sayed, *Chem. Soc. Rev.* **2006**, *35*, 209-217.
2. Y. N. Xia, P. D. Yang, Y. G. Sun, Y. Y. Wu, B. Mayers, B. Gates, Y. D. Yin, F. Kim, Y. Q. Yan, *Adv. Mater.* **2003**, *15*, 353-389.
3. C. J. Murphy, T. K. San, A. M. Gole, C. J. Orendorff, J. X. Gao, L. Gou, S. E. Hunyadi, T. Li, *J. Phys. Chem. B* **2005**, *109*, 13857-13870.
4. B. Nikoobakht, M. A. El-Sayed, *Chem. Mater.* **2003**, *15*, 1957-1962.
5. K. J. Stebe, E. Lewandowski, M. Ghosh, *Science* **2009**, *325*, 159-160.
6. D. Baranov, A. Fiore, M. van Huis, C. Giannini, A. Falqui, U. Lafont, H. Zandbergen, M. Zanella, R. Cingolani, L. Manna, *Nano. Lett.* **2010**, *10*, 743-749.
7. N. Zhao, K. Liu, J. Greener, Z. H. Nie, E. Kumacheva, *Nano. Lett.* **2009**, *9*, 3077-3081.
8. Z. H. Nie, D. Fava, E. Kumacheva, S. Zou, G. C. Walker, M. Rubinstein, *Nat. Mater.* **2007**, *6*, 609-614.
9. S. Kumar, H. K. Bisoyi, *Angew. Chem. Int. Edit.* **2007**, *46*, 1501-1503.
10. X. B. Zeng, F. Liu, A. G. Fowler, G. Ungar, L. Cseh, G. H. Mehl, J. E. Macdonald, *Adv. Mater.* **2009**, *21*, 1746-+.
11. M. Yamada, Z. R. Shen, M. Miyake, *Chem. Commun.* **2006**, 2569-2571.
12. S. Umadevi, X. Feng, T. Hegmann, *Adv. Funct. Mater.* **2013**, *23*, 1393-1403.
13. X. Feng, L. Sosa-Vargas, S. Umadevi, T. Mori, Y. Shimizu, T. Hegmann, *Adv. Funct. Mater.* **2015**, *25*, 1180-1192.

List of Abbreviations and Symbols

1D	One-dimensional
2D	Two-dimensional
3D	Three-dimensional
5CB	4-Cyano-4'-pentylbiphenyl
8OCB	Octyloxy cyanobyphenyl
CNT	Carbon nanotube
Col_h	Hexagonal columnar phase
Col_{ho}	Ordered hexagonal columnar phase
Col_{hp}	Plastic hexagonal columnar phase
Col_{ob}	Oblique columnar phase
Col_r	Rectangular columnar phase
Cr	Crystal phase
CTAB	Hexadecyltrimethylammonium bromide
DLC	Discotic liquid crystal
DMF	Dimethyl formamide
DSC	Differential scanning calorimetry
GNR	Gold nanorod
H4TP	Hexabutoxytriphenylene

H5TP	Hexapentyloxytriphenylene
H6TP	Hexahexyloxytriphenylene
Iso	Isotropic phase
ITO	Indium Tin Oxide
LC	Liquid crystal
LCD	Liquid crystal display
LSPR	Longitudinal surface plasmon resonance
N_{Col}	Columnar nematic phase
N_D	Discotic nematic phase
N_u	Uniaxial nematic phase
NMR	Nuclear magnetic resonance
ODS	Octadecyltrimethoxysilane
POM	Polarized optical microscopy
SAXS	Small angle X-ray scattering
SmA	Smectic-A phase
SmC	Smectic-C phase
SPR	Surface plasmon resonance
TEM	Transmission electron microscopy
THF	Tetrahydrofuran
TOF	Time of flight
TSPR	Transverse surface plasmon resonance
XPS	X-ray photoelectron spectroscopy
XRD	X-ray diffraction

List of Appendices

Chapter 1

Introduction

Traced back to 1888, when F. Reinitzer[1] was conducting melting point measurements of an organic compound, an opaque cloudy phase was observed during heating before the compound reached the clear liquid phase. One year after, O. Lehmann[2] observed a similar phenomenon and discovered crystalline properties of this new-found liquid mesophase. However, academia had not paid too much attention to this new state of matter until the publication of a review article by G. H. Brown[3] from Kent State University, which covered almost 500 papers published from 1888 to 1956. Researchers from various nations started to work on this new field and many interesting features of liquid crystal materials have been discovered since then, such as electro-optic switching and a fascinating array of self-assembled structures. Nowadays, research topics that relate to liquid crystal materials are crossing the boundaries of all kinds of research fields including electronics, optics, nanotechnology, polymers, biology, and medical treatments etc.

Currently, nanotechnology has become one of the most attractive research topics worldwide. The importance of nanotechnology has been acknowledged both by academia and industry. The most straightforward example is the rapid development of semiconduc-

tor chip industry. The exponential growth of both the calculation speed and the storage capacity of computers (4 times in every 3 years) are achieved by reducing the sizes of every unit in the chips employing nanolithography technology. However, the limited resolution of lithography makes this technique not able to etch scales smaller than several tens of nanometers. Self-assembly of premade nanoparticles into certain designed alignment is considered to be a feasible bottom-up approach for fabricating the new generation of nano-sized devices. The beauties of nanotechnology are far more than just small size. Due to quantum confinement effects, nano-scaled materials may show unique features in many properties such as thermodynamic, optical, electrical, magnetic, and chemical, compared with the corresponding bulk phase. The macroscopic properties of nanomaterials are not only decided by the size and the shape of the nanoparticle, but also affected by the arrangement, the self-assembly of the nanoparticles.

1.1 Liquid Crystals

Most pure organic compounds have sharp melting points, turning into a clear isotropic liquid directly from the anisotropic crystal when heated. On the other hand, some compounds (such as cholesterol esters) will experience mesophases during melting, which appear to be a cloudy liquid, before turning into a completely clear liquid. This optical feature is derived from the anisotropic structure of the mesophase liquid, indicating that there is still a certain degree of molecular ordering character in one or more dimensions. Liquid crystal phases possess both the fluidity and continuity of a liquid as well as the anisotropy of a crystal, hence the name “liquid crystals”.[4] As a matter of fact, liquid

crystals (LCs) can be divided into two categories according to the conditions and components for the formation of LC phases: thermotropic LCs and lyotropic LCs. As the names suggest, thermotropic LCs form due to the change of temperature, and only exist in a certain temperature range. Thermotropic LCs are commonly formed from a single component; while lyotropic LC phases are normally formed from mixtures of compound(s) and solvent(s), and the phases vary depending on the concentrations of the compound(s). In the work of this thesis, only thermotropic LCs have been involved.

1.1.1 Liquid Crystal phases and molecular structures

Thermotropic liquid crystals can be further divided into three types based on the shape of the molecular constituents:[5] (Fig. 1.1) calamitic (rod-like), bent-core (banana-shape) and discotic (disk-like). Generally speaking, the structure of liquid crystal molecules is anisometric (i.e. the length of at least one molecular axis significantly differs from the other two). The LC molecules normally have a rigid aromatic core, and conjugated systems are usually introduced to restrict core deformation and allow for π-π interactions. The formation of LC phases is mainly driven by the segregation of chemically incompatible subunits such as the rigid aromatic core and flexible alkyl chains. Calamitic LC molecules can form nematic, smectic, and even columnar phases [5]. Bent-core LC molecules form mostly smectic phases and even chiral smectic phases, while discotic LC molecules commonly form nematic (N_D and N_{Col}) and columnar phases (Fig. 1.2).

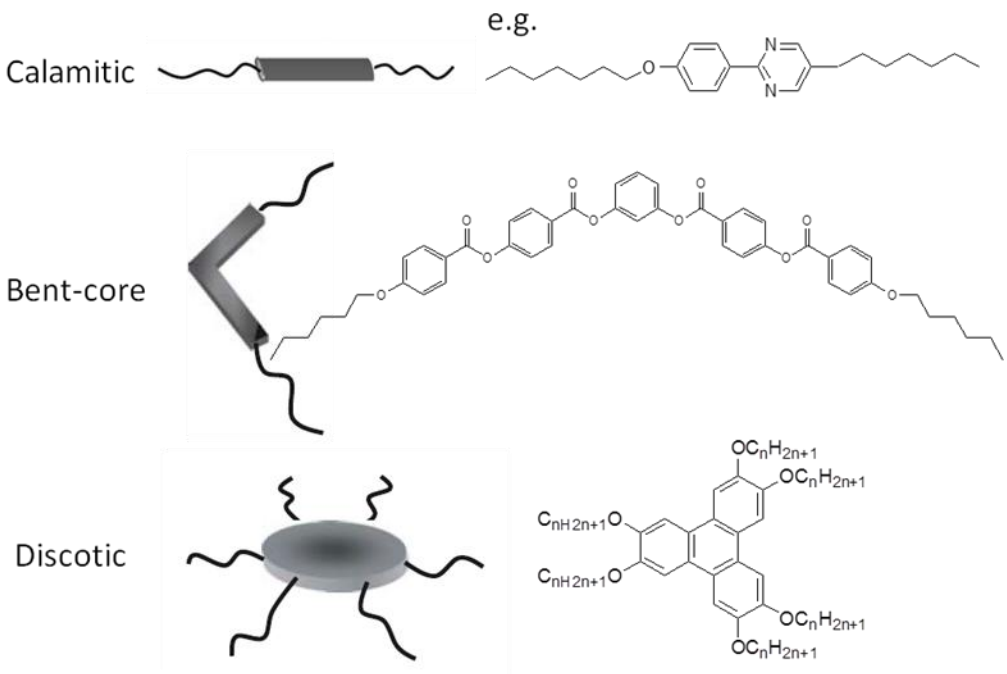

Figure 1.1. Molecular shapes forming themotropic liquid crystal phases. (Adapted from ref. 5)

The nematic phase is the least ordered LC phase. The molecules only possess orientational ordering and no positional ordering (Fig. 1.2). The nematic phase generally forms when the volume fraction of the rigid core is far higher than that of the side chains in the LC molecules.[5] The anisotropic molecules tend to be aligned with their long molecular axis (for calamitic LC molecules) or short molecular axis (in the case of discotic LC molecules) parallel to some common axis, named director ***n***. The direction of ***n*** is arbitrary in space, but in practice can be imposed by external forces such as surface anchoring force and applied electric or magnetic field. The order parameter ***S***[6] can be defined as:

$$\boldsymbol{S} = \frac{1}{2} < 3\cos^2\theta - 1 > \qquad (1.1)$$

where θ is the angle between the molecular axis and the director ***n***. The angular brackets indicate the average value during certain space and time. It is not hard to deduce that ***S*** = 1 when all molecules are parallel to the director ***n*** (θ = 0 °or 180 °). On the other hand, if the molecules are randomly oriented, $< \cos^2\theta > = \frac{1}{3}$, with the result that ***S*** = 0. Typically, the order parameter ***S*** of nematic LCs is in the range of 0.3 – 0.8, which is temperature depended. Increasing temperatures reduce the value of ***S***, and the value becomes 0 when the temperature hits the clearing point, which is the transition temperature between any mesophase and the isotropic liquid phase on heating, indicating that the LC phase turned into an isotropic liquid. The concept of the order parameter ***S*** can be applied to other anisotropic systems, such as nanorods doped into discotic LC phases discussed in chapter 4 of this thesis.

Smectic phases are LC phases with both orientational and positional order (Fig. 1.2). The two most important smectic phases[7] are the smectic A phase (SmA) where the molecules are aligned with the long molecular axis perpendicular (averaged over time) to the layer plane, and the smectic C (SmC) phase where the molecules are tilted from the plane normal. Smectic phases are usually observed for rod-like molecules with longer hydrocarbon chains and normally below the nematic phase on cooling because smectic phases are higher ordered than nematic phases.

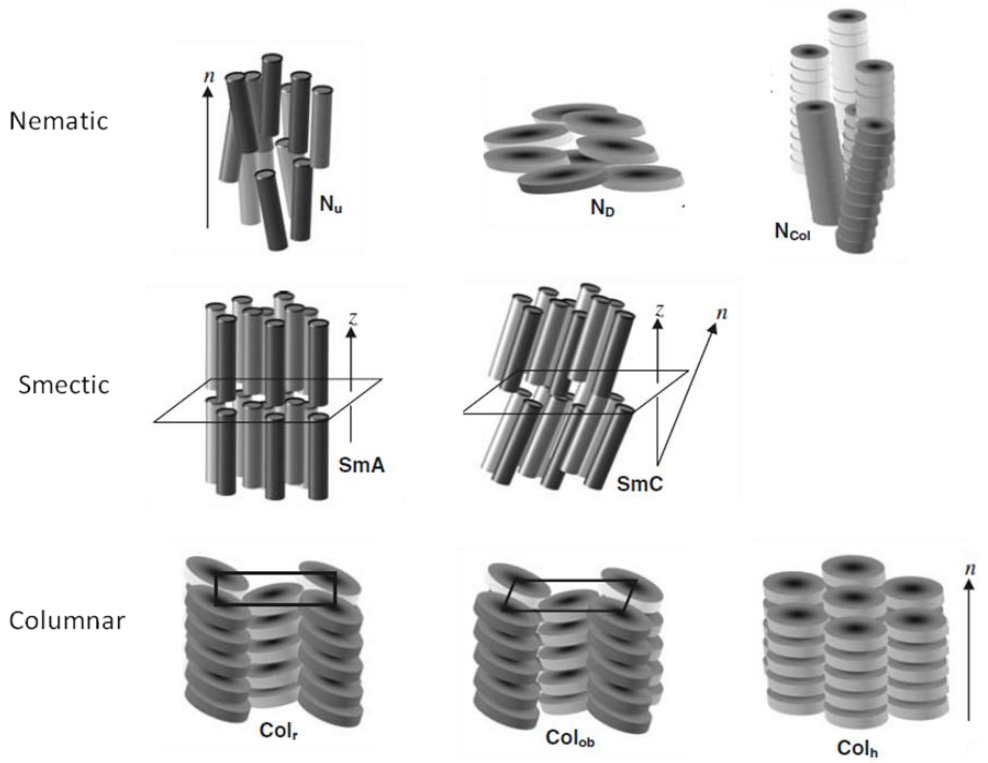

Figure 1.2. Schematic diagrams of the main types of themotropic LC phases structures. Abbreviations: N_u = uniaxial nematic phase, N_D = discotic nematic phase, N_{Col} = columnar nematic phase, SmA = smectic-A phase, SmC = smectic-C phase, Col_r = rectangular columnar phase, Col_{ob} = oblique columnar phase, Col_h = hexagonal columnar phase. (Adapted from ref. 5)

Discotic LCs are comparatively speaking new materials. The first LC phase formed by disk-like molecules was reported by Chandrasekhar[8] in 1977. From the example in Fig. 1.1, a discotic LC molecule is normally composed of an aromatic core (usually polycyclic) and several flexible side chains to prevent the compound from crystallization. The aromatic disk-like core can be composed of various polycyclic aromatic units, such as (a) triphenylene, (b) perylene, (c) coronene, (d) hexabenzocoronene and (e) truxene. In the work of this thesis, only triphenylene based discotic LCs are discussed.

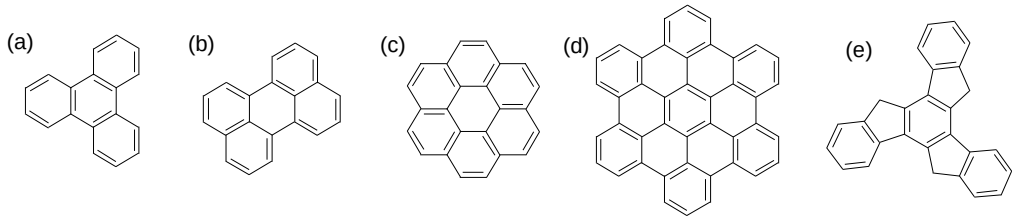

Scheme 1.1. Polycyclic aromatic cores for discotic liquid crystals

Disk-like molecules tend to pack into columns with aromatic planes stacked together due to the strong π-π interactions, and the columns can be further organized into arrays with various symmetries such as rectangular (Col_r), oblique (Col_{ob}), or hexagonal (Col_h) (Fig. 1.2).

As mentioned above, various forces can manipulate the direction of the orientational director ***n***. In fact, the alignment of LCs is one of the most important techniques in the current LC displays (LCD) industry. The orientation of LCs in a LCD device is under very fine control by adjusting the external electric field force against the surface anchoring force to tune the transmittance of light of the LC layer, so that the light intensities of the three-primary colors in each pixel can be varied to give thousands of different colors.

In order to reach homogeneous alignment by surface anchoring forces, the surface of the substrates should be pre-treated, mechanically or chemically. The simplest way to achieve planar alignment, which means the director ***n*** is parallel to the substrate surface, is to rub the surface, normally coated by thin layer of polyimide, with a velvet cloth in some defined direction. For obtaining homeotropic alignment, indicating that the director ***n*** is perpendicular with the substrate surface, the substrate needs to be pre-treated with a surfactant, such as lecithin. In the case of discotic LCs, planar alignment can be achieved by simply shearing the substrate in one direction mechanically. The homeotropic alignment of discotics can be achieved in many ways such as chemical treatment,[9] IR radia-

tion,[10] and the application of an external magnetic field.[11] Magnetic fields have for example been employed for the alignment of nematic and smectic LCs.[12] In fact, most organic aromatic compounds are diamagnetic materials, and their diamagnetic susceptibility is much higher in the direction when the magnetic field penetrates through the ring plane due to the induced circuit of delocalized electrons in aromatic rings ($\Delta\chi = \chi_{\parallel} - \chi_{\perp}$). This anisotropy of the diamagnetic susceptibility aligns the molecules in the magnetic field with the ring plane parallel to the magnetic field to stay in a lower energy state. The magnetic susceptibility of a liquid crystal material is defined as $\Delta\chi' = N\Delta\chi S$, where N is the number of LC molecules and S is the order parameter. The free energy density[6a] of liquid crystals in a magnetic field can be defined as:

$$\boldsymbol{f} = -\mu_0 \Delta\chi' (\boldsymbol{n} \cdot \boldsymbol{H})^2 \qquad (1.2)$$

where μ_0 stands for the magnetic permeability of vacuum, $\boldsymbol{n}$ is the director of the LC phase and $\boldsymbol{H}$ is the applied magnetic field. The equation indicated that the free energy become lowest ($\Delta\chi' > \mathbf{0}$) when the director $\boldsymbol{n}$ parallel with the magnetic field. Theoretically, considering a sufficient number of LC molecules, the free energy should be low enough to overwhelm the thermal agitation energy kT (k is the Boltzmann constant, T is the temperature) and achieve a uniform alignment of the LC molecules controlled by the applied magnetic field.

1.1.2 Characterization of Liquid Crystal phases

1.1.2.1 Polarizing Optical Microscopy (POM)

Due to the anisometric shape of LC molecules and the anisotropic structures of the LC phases formed, LCs possess birefringence, which will give various optical textures for different LC phases under a polarizing optical microscope. Birefringence is the optical property of materials that have different refractive indices of light depending on the propagation direction within the material. When light enters a birefringent material, such as a nematic liquid crystal sample, the incident light will be broken up into a fast (called the ordinary ray) and a slow (called the extraordinary ray) component. Because the two components travel at different velocities, when the rays recombine as they exit the birefringent material, the polarization state will be changed because of this phase difference. Fig. 1.3[13] is the basic configuration of a POM system. Light from the bottom is plane polarized once it passes a polarizer and then hits the birefringent sample where it is split into two orthogonal rays, ordinary and extraordinary. The combined rays can partially pass through the analyzer due to the change of polarization. Rays derived from different spots of the sample have varied phase alteration between the ordinary and extraordinary rays, and because of the interference, the recombined light will have various wavelengths, hence presenting a colorful texture basically indicating some structural information of the analyzed birefringent sample. Without any sample present in the holder, light will not pass the crossed polarizer-analyzer couple, thus the field of view will be completely dark. In addition, when the polarization of incident light is parallel with either the ordinary or extraordinary direction of the sample, light will not be broken up into the two components and no change of polarization occurs. Hence no light will pass through the 90 °crossed polarizer above the sample (the analyzer), which will also lead to a dark field of view.

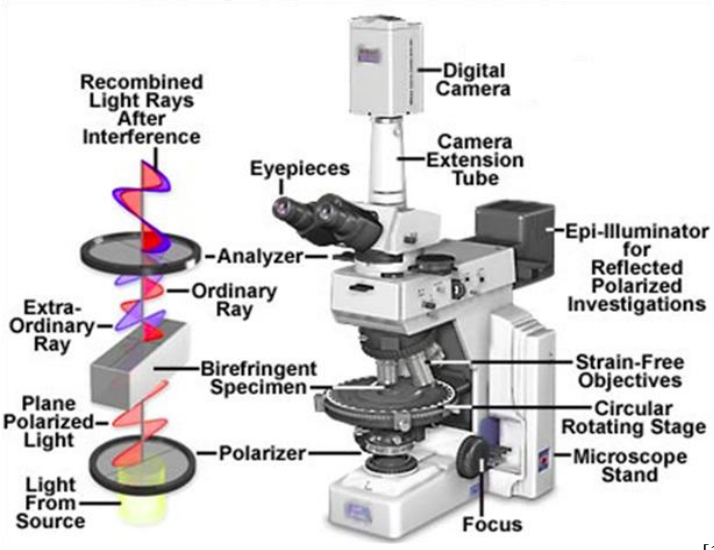

Figure 1.3. Polarizing Optical Microscopy configuration [13c]

Fig. 1.4 shows some typical texture images of LC phases observed by POM. Fig.1.4a is an example of a *Schlieren* texture from a nematic LC phase. *Schlieren* textures exhibit sets of dark brushes, corresponding to local molecular orientations where the director ***n*** of the LC domains are parallel to one of the polarizers. Fig. 1.4b is the POM image of a mosaic texture from a hexagonal columnar LC phase. The texture presents larger areas of segregations of the LC domains, which are separated by grain boundaries. In each domain, the columnar phase has a uniform director orientation, which gives an even optical appearance.

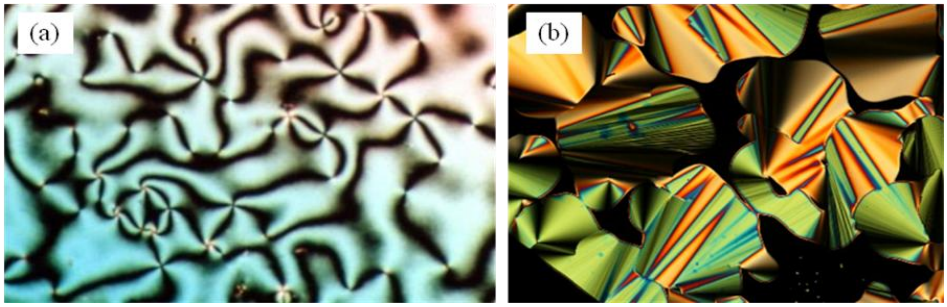

Figure 1.4. Typical LC textures from POM: (a) *Schlieren* texture of nematic phase [13e]; (b) mosaic texture of discotic Col_h phase [13f].

1.1.2.2 Differential Scanning Calorimetry (DSC)

To obtain phase transition temperatures of LCs, DSC is a commonly used approach. The principle of DSC is based on the change of the amount of heat absorbed or released during the phase transition processes. As shown in Fig. 1.5, the sample is first sealed in an aluminum pan, and then placed in a separated furnace from the reference, which is an empty aluminum pan. When phase transitions occur in the sample, heat will be consumed or released from the sample to the environment, which will cause a temperature inequivalence, detected by a number of well-distributed thermocouples. In order to keep the balance between the sample and the reference, power will be applied or removed by the calorimeter to compensate for the energy uptake or release of the sample. The amount of the power required to maintain the system in equilibrium is directly proportional to the energy changes occurring in the sample.

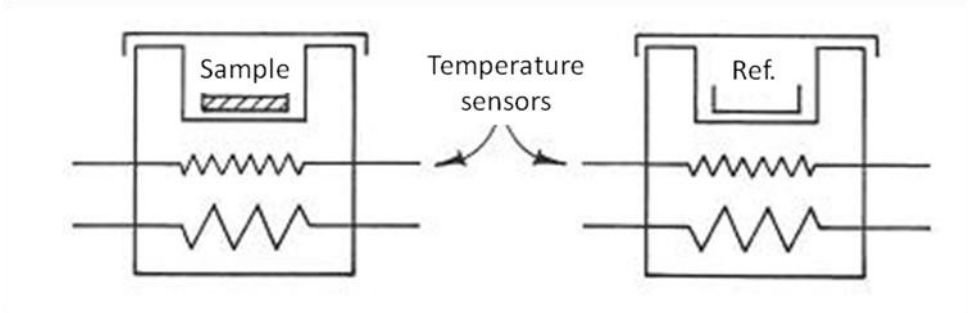

Figure 1.5. Schematic Illustration of the heat-compensation DSC. (adapted from ref. 13a)

Fig. 1.6 is an example of a DSC curve for 8OCB (4-cyano-4'-octyloxybiphenyl) with a phase sequence on cooling of Iso 81 N 67 SmA 26 Cr. The positive and negative peaks are corresponding to the phase transition temperatures during cooling and heating process respectively. Isotropic 8OCB turns to nematic phase at 81 ℃, then to the SmA phase at 67 ℃ and finally crystallizes at 26 ℃. The Isotropic to nematic transition is slightly shifted to lower T values in the upper curve during cooling compared with the heating

run, and partially because of supercooling, partially because of instrumental hysteresis. The SmA to crystal transition is strongly depressed from 55 ℃ (transition temperature on heating) to 26 ℃ during cooling which is mainly due to supercooling of the LC phase.

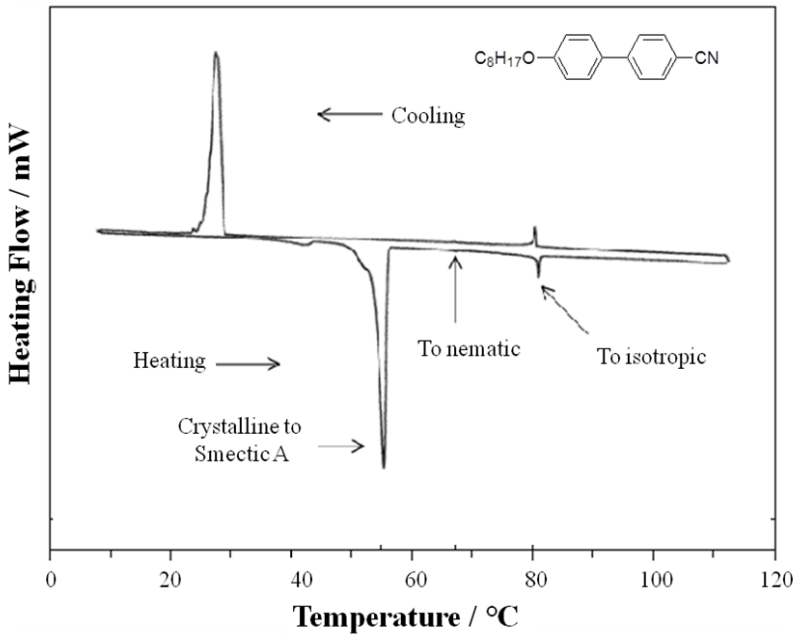

Figure 1.6. DSC plots of 8OCB with phase transitions. (adapted from ref. 13b)

1.1.2.3 X-ray Diffraction

XRD has been used to investigate the microstructure of crystal phases. Diffraction is a phenomenon that occurs when radiation is elastically scattered from atoms in a sample. In a given direction, the intensity of the scattering depends on the spatial distribution of the atoms, which makes XRD a powerful probe in the static structure of ordered crystalline phases. For one particular set of lattices, constructive interference of rays scattered by successive planes will only occur when the path difference ($2d \sin\theta$) equals an integer number of the wavelength of the ray (*Bragg's Law*, Fig. 1.7 a):

$$2d \sin \theta = n \lambda \qquad (1.4)$$

Where d is the space between the planes, θ is the angle of incidence.

Figure 1.7b shows a 2D XRD diffraction pattern of silver behenate, which has a large number of well-defined diffraction peaks especially in the low angle diffraction range, commonly used as a standard compound for calibrating XRD orthogonal plots. Figure 1.7c shows an example of XRD plot of a Col_h phase. The scattering vector $\boldsymbol{q}$ represents the space separation of liquid crystal molecules or subunits ($\boldsymbol{q} = 2\pi / \boldsymbol{d}$). Larger magnitude of $\boldsymbol{q}$ indicates stronger diffraction, corresponding to smaller space distance $\boldsymbol{d}$. In figure 1.7c is a XRD plot of hexahexyloxytriphenylene (H6TP) taken at 80 ℃, where d_3 indicates the space between the stacking of the polyaromatic disks, d_2 represents the space between the alkyl side chains, and d_1 is the distance between the stacked aromatic cores within the columnar aggregates.

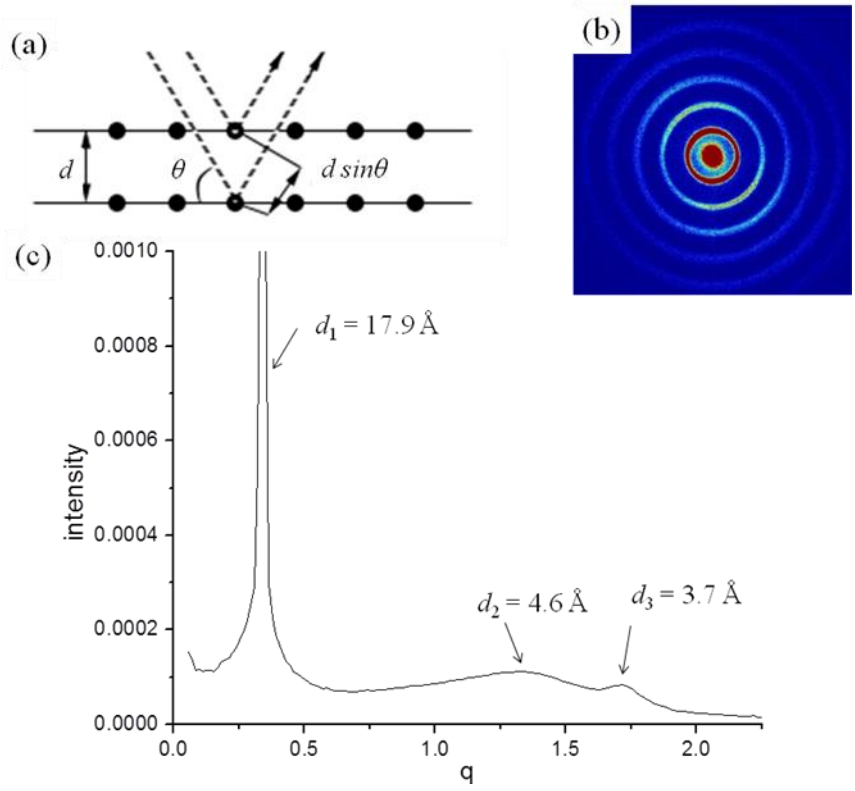

Figure 1.7. a) Bragg's law of XRD in a crystalline lattice (adapted from ref. 13d); b) 2D diffraction pattern of silver behenate; c) A typical XRD orthogonal plot of Col_h liquid crystal phase, *q* is scattering vector.

1.2 Gold Nanorods

Noble metal nanoparticles attract significant attention from ongoing research due to the surface plasmon resonance (SPR) absorption[15]. One of the most obvious phenomena resulting from the SPR is the color variation of the colloidal suspensions depending on the size and shape of the dispersed nanoparticles and the dielectric constant of the surrounding medium[16]. The frequency of surface plasmon oscillations of gold and silver is usually in the visible light region. Free electrons in metals are free to travel within the material. The mean free path of electrons in gold and silver is ~50 nm. Thus, for particles

smaller than this scale, no scattering is expected from the bulk, and all interactions should be with the surface. Fig. 1.8a represents a SPR mechanism derived from coherent interaction of electrons in the conduction band with the incoming light. The electron distribution in the particle is polarized to one end as the wave front of light passes, and oscillates in resonance with the light frequency, causing a strong absorption of the light, which can be determined by absorption and scattering spectroscopy. The spectra are affected by the size and shape of the nanoparticles (Fig. 1.8b). Spherical nanoparticles usually show an absorption band around 500 nm, varying slightly as the size changes. As for anisotropic gold nanorods, the absorption band splits into two, known as transversal (short wavelength) and longitudinal (long wavelength) SPR absorption bands. More interestingly, nanorods possess tunable optical properties. This unique property provides gold nanorods valuable applications in imaging[17], sensing[18], biology, and medicine[19].

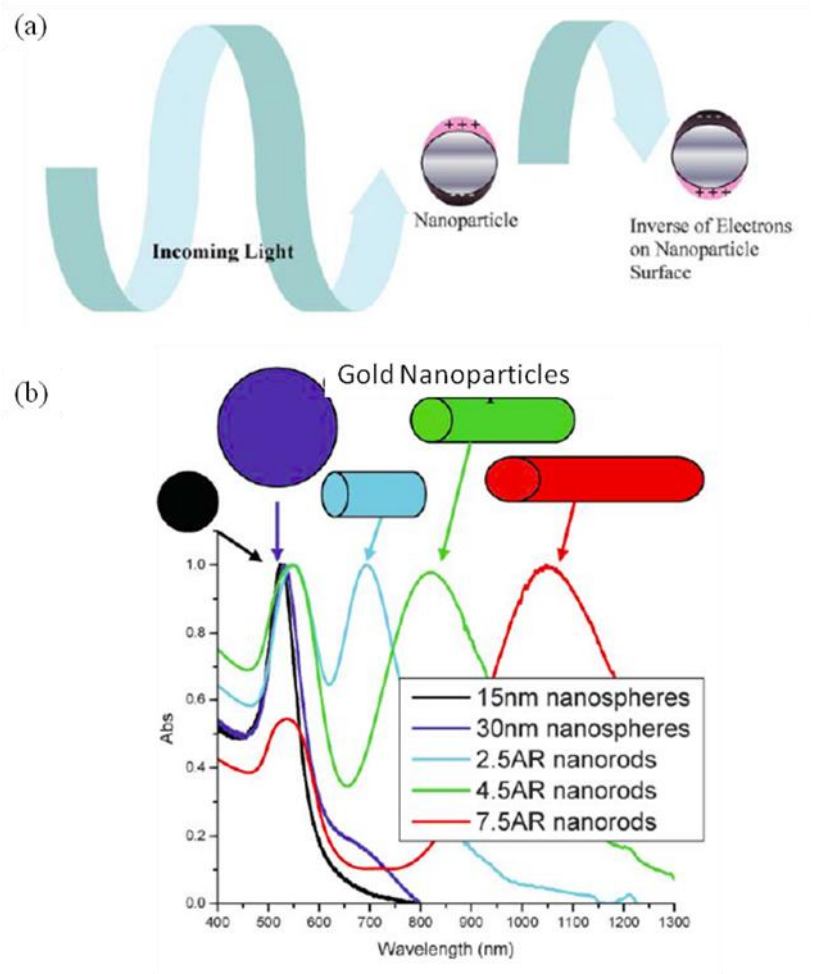

Figure 1.8. a) Origin of surface plamon resonance; b) SPR absorption of various sizes and shapes of gold nanoparticles. (reprinted with permission from ref. 16)

1.2.1 Synthesis of Gold Nanorods

The essence of the formation of rod-like, often termed one-dimensional or 1D nanoparticles such as nanorods and nanowires is crystallization, from a vapor, liquid or ionic state, which involves two steps: nucleation and growth. Fig.1.9 shows some strategies of the synthesis of 1D nanostructures[20]: a) introduction of a liquid-solid interface to confine the growth direction of a seed; b) directed through the use of various templates with 1D mor-

phologies; c) kinetic control through appropriate usage of supersaturate capping agent to modify the growth habit of a seed; d) guided self-assembly of spherical nanoparticles.

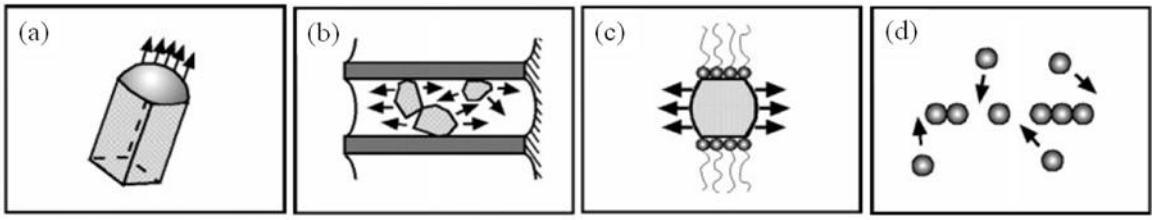

Figure 1.9. Schematic illustrations of some strategies for the achievement of 1D nanostructures. (reprinted with permission from ref. 20)

For the synthesis of metallic colloidal nanoparticles, some approaches involve the usage of capping agents as shown in Fig.1.9c. Gold nanorods can be synthesized in the presence of surfactants in aqueous media by a seed-growth method developed by Jana et al.[21]. A typically reported seed-growth method has two steps. First is the preparation of the seed solution. A $HAuCl_4$ aqueous solution with certain concentration (2.5×10^{-4} M) is mixed with same amount of tri-sodium citrate, followed by adding a small amount of sodium borohydride under vigorous stirring to produce nanoparticles with the size of 3.5 ± 0.7 nm. The second step is injecting a small portion of seed solution into a growth solution made from same concentration of $HAuCl_4$ and 0.1 M hexadecyltrimethylammonium bromide (CTAB), reduced by ascorbic acid (0.1 M) from Au^{3+} to Au^{+}. This method produces gold nanorods with aspect ratio around 4.6. For the synthesis of gold nanorods with higher aspect ratio, a three-step method was developed (Fig. 1.10)[22]. 1.0 mL seed solution was added in to 9.0 mL growth solution to make solution A. After 4-5 h, 1.0 mL solution A was added in to another 9.0 mL growth solution. The resulting solution B was added to 90 mL of growth solution after 4-5 h to make solution C, which contained gold nanorods with aspect ratio 13 after a few hours' growth. One of the weak points of this

approach is that the yield of rod-shaped particles is lower than 50%, and the final solution contains significant amount of spheres and plates, which create challenges for the separation and isolation of nanorods.

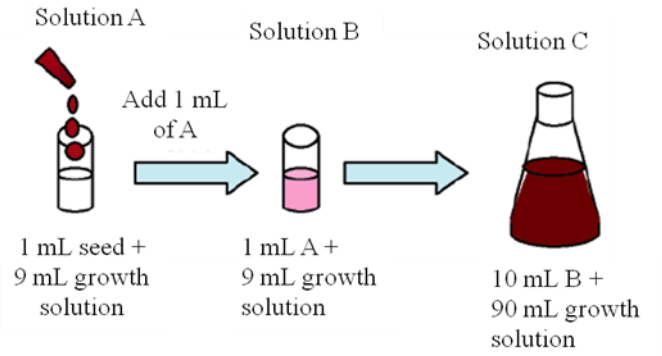

Figure1.10. Three-step seed-growth approach for the synthesis of high aspect ratio gold nanorods. (reprinted with permission from ref. 22)

A modified seed-mediated growth approach reported by El-Sayed *et al.*[23] demonstrated that the yield of nanorods can be almost 100% with very tiny amount of spheres and other shapes less than 1%. The two strategies of modification are replacement of the citrate for seed solution with CTAB, and adjusting the concentration of Ag^+ ions as an additive in the growth solutions. The role of Ag^+ is found to be critical for the growth of gold nanorods. Murphy et al.[24] demonstrated that with the presence of ~5% of Ag^+ the yield of nanorods raised to nearly 100% compared to ~30% in the absence of Ag^+. Moreover, by increasing the Ag^+ concentration, the longitudinal plasmon band red-shifted, indicating an increase in the aspect ratio of the gold nanorods. One possible explanation[23] would be that Ag^+ ions are present as Ag-Br species between the head groups of the surfactant, which may decrease the charge density on the bromide ions resulting in less repulsion between the neighbouring head groups on the surface of the gold particles. In turn, this may assist in the formation of elongated surfactant templates. In exploring the

influence of various synthetic parameters on gold nanorod growth, other parameters in the growth step have been examined. In the two step seed-growth method mentioned above, the concentration of CTAB is required to be as high as 0.1 M for obtaining a high yield of nanorods, and the concentration of $HAuCl_4$ around 0.001 M is demonstrated to be optimized for obtaining high aspect ratio gold nanorods[23]. In addition, gold seeds with smaller size were discovered to produce higher aspect ratio gold nanorods[25].

Other strategies have been developed to grow higher aspect ratio gold nanorods. One example is the use of aromatic additives[26]. The addition of appropriate amounts of sodium salicylate to the CTAB growth solution is an efficient way to synthesize gold nanorods with a longitudinal SPR absorption band greater than 900 nm. This suggests that the mechanism of the influence of the aromatic additives may lie with the modification of the interface or interaction between the cationic CTAB micelles and the developing gold nanorods. Koeppl *et al.*[27] have demonstrated that the average aspect ratio of gold nanorods can be varied between 8 to 19 by adjusting the use of H_2O-D_2O mixtures as the solvent for the growth solution. The most likely mechanism considers involvement of contributions of O-D bond in the rate-determining step, which leads to a slower reduction of Au^+ ions to gold atoms and higher morphological selectivity for the crystallization to form gold nanorods.

The growth mechanism of gold nanorods in the presence of CTAB has been proposed as showed in Fig.1.11[22]. As the nucleation of the gold seed develops to form particles with different crystalline facets, the surfactant molecules may preferentially bind to certain facets. In this mechanism, CTAB molecules are suspected to direct the growth of

gold nanorods by blocking the long axis crystal faces, and so favoring the growth on the short axis faces to make rod-like particles.

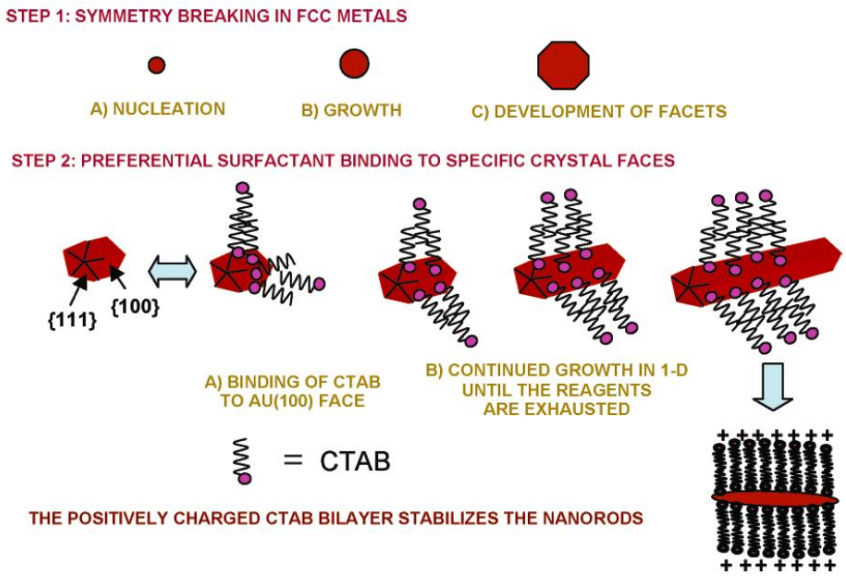

Figure 1.11. Schematic illustration of the growth mechanism of gold nanorods synthesized in supersaturated CTAB aqueous solution. (Reprinted with permission from ref. 22)

1.2.2 Characterization Methods of Gold Nanorods

One of the most attractive properties of gold nanostructures is their SPR optical absorption. As mentioned above, gold nanostructures possess strong absorption in the visible and near IR wavelength range due to the localized SPR of noble metals. The absorption band is highly dependent on the size, the shape, and the dielectric constant of the surrounding medium [28]. For gold nanorods, the longitudinal surface plasmon resonance (LSPR) absorption band depends on the aspect ratio of the nanorods. Fig.1.12[23] is showing the correlation of the LSPR absorption band wavelength and the aspect ratio of gold nanorods. In this thesis, the gold nanorods synthesized have LSPR band around 800 nm,

which corresponding aspect ratio of ~3, confirmed by transmission electron microscopy (TEM).

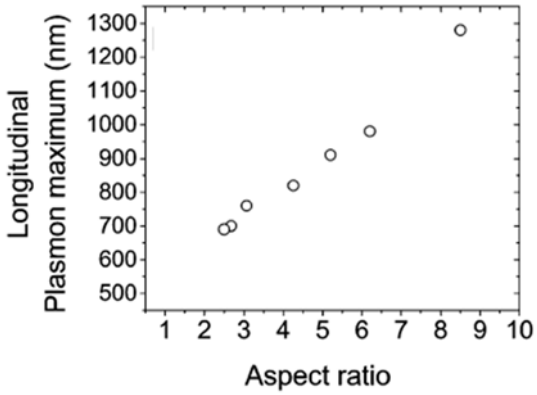

Figure 1.12. The linear plot of the correlation between the LSPR absorption band and the aspect ratio of gold nanorods. (Reprinted with permission from ref. 23)

TEM is well acknowledged to be a more straightforward characterization approach for the morphology determination of nanostructures. The resolution of TEM is decided by the wavelength of the electron beam and the aberrations of the image forming lenses. Modern TEM commonly has a point-to-point resolution of about 0.2 nm, which endows TEM a reliable and accurate solution in the measurement of size, space, shape, and even atomic structure of nanomaterials.

1.3 Self-Assembly of Nanoparticles

Certain applications of nanomaterials require collective properties of nanoparticles for the construction of nanoscale devices[20, 29]. For achieving super-structures of nanoparticle arrays, two strategies are normally applied: a top-down approach from a bulk material through lithographic techniques and a bottom-up approach achieved by the self-assembly

of individual nanoparticles. The latter approach has been broadly investigated by researchers due to the advantage of overcoming the resolution limitation of lithographic techniques confined by the beam wavelength[30]. Moreover, self-assembly of nanoparticles into functional structures enables the fabrication of real 3D nanoscale devices[31]. Especially for non-spherical nanoparticles, 2D or 3D ordered self-assembly is essential for the fabrication of functional nanoscale electronics[32]. The self-assembly process of nanoparticles occurs driven by the energetics of the system to form ordered and functional aggregates. One of the most important principles of self-assembly are the interaction energies between the building blocks, acting as a main driving force of the assembly of the subunits in the resulting super-structure. The interaction energies can be sorted into three categories[33]: molecular interaction energies, macroscopic interaction energies, and interactions based on hydrogen bonding, hydrophobic and hydrophilic effects. Molecular interaction energies include Coulomb interactions, van der Waals interactions and short-range repulsive interaction. Macroscopic interaction energies are mainly decided by van der Waals attraction and electrostatic repulsive energy between two nanoparticles. Hydrophobic surfaces will cause water molecules to reorient themselves with the charges pointing away from the surfaces so that a hydrophobic hydration layer will be produced. As a consequence, hydrophobic attraction occurs between hydrophobic molecules and surfaces, because of the rearrangement of the hydrogen bond configurations in the overlapping salvation zone as the two hydrophobic surfaces come closer. Contrary to hydrophobic molecules, hydrophilic molecules can be associated with water molecules and tend to repel each other in water.

In general, stimulations for inducing the self-assembly of nanoparticles can be divided into four categories[34]: 1) assembly by the attraction forces between nanoparticles occurring in colloidal solutions; an example is shown in Fig.1.13[35]; 2) assembly at various types of interfaces; 3) assembly induced by external fields; and 4) assembly induced by templates.

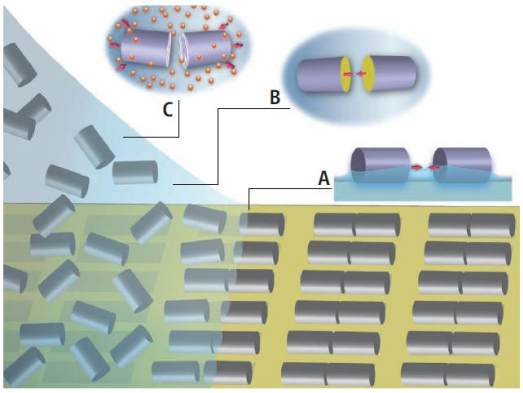

Figure 1.13. Schematic illustration of several self-assembly behaviors of nanoparticles: A) capillary interactions near the contact line; B) hydrophobic interactions created by selective surface functionalization; C) depletion attraction in bulk. (Reprinted with permission from ref. 35)

1.3.1 Self-Assembly of Nanorods

Earlier reports on the self-assembly of nanoparticles mainly involved a solvent evaporation process on suitable substrates to form 2D monolayer arrays[29e, 30, 36]. It did not take too long for the attention on the self-assembly of spherical nanoparticles to turn to 1D nanorods[37].

Kumacheva *et al.*[38] developed a strategy for inducing the self-assembly of nanorods by functionalizing them with hydrophobic ligands (such as polystyrene, octadecylphosphonic acid, or hexylphosphonic acid), followed by adding polar solvents (water or DMF) into nanorod dispersions in non-polar organic solutions (toluene) to reduce the

solubility of the surface ligand, thus causing their attraction to form assemblies of attached nanorods in an end-to-end[38c] (Fig.1.14a) manner. A side-by-side[38b] assembly of Au-tipped CdSe nanorods (Fig.1.14b) has also been achieved by applying this approach.

Manna *et al.*[37g] demonstrated a self-assembly approach for nanorods employing depletion attraction, defined as[55a] an effective attractive force that arises between large colloidal particles that are suspended in a dilute solution of depletants, which are smaller solutes that are preferentially excluded from the vicinity of the large particles. The assembly was triggered by adding additives such as long alkyl chain fatty acids and amines, the liquid crystal 4'-*n*-pentyl-4-cyanobiphenyl (5CB), oleic acid, or polymers (polystyrene, polyethylene glycol methacrylate) into the nanorod dispersions in organic solvents to form close-packed hexagonally ordered monolayer arrays. The exclusion of the additives from between the nanorods resulted in a local concentration gradient, which led to the close packing of the nanorods (Fig.1.14 c & d).

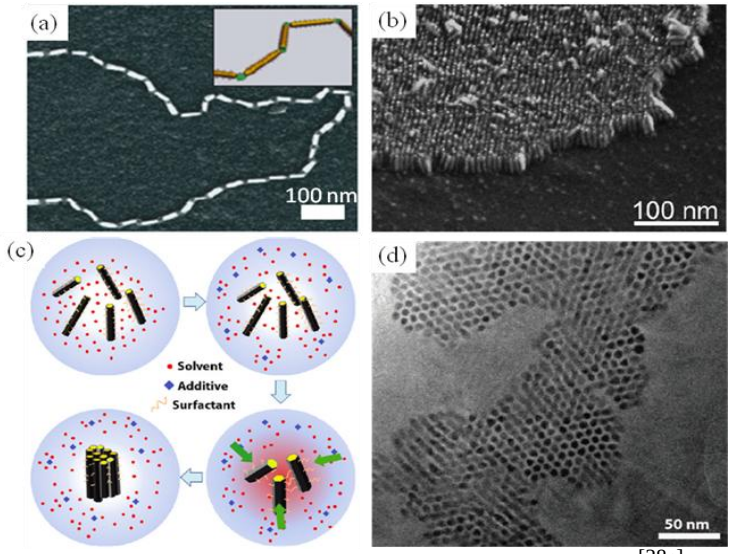

Figure 1.14. a) TEM image of end-to-end assembly of nanorod [38c]; b) TEM image of side-by-side nanorods assembly[38b]; c, d) schematic illustration of depletion attraction of nanorods and TEM image of assemblies[37g]. (Reprinted with permission from ref. 38c, 38b, and 37g)

Hydrogen bonding and electrostatic attraction were also considered to be effective factors for inducing the self-assembly of nanorods. Thomas *et al.*[39] demonstrated that hydrogen bonding between 11-mercaptoundecanoic acid or 3-mercaptopropionic acid molecules attached on the ends of nanorods was the key factor for the nanorods to form end-to-end assemblies. The same research group also reported that gold nanorods functionalized with glutathione and cysteine possessed a high tendency to form end-to-end assemblies due to the cooperative electrostatic attraction between the zwitterionic groups of the functional ligands[40].

The formation of covalent bonds was also investigated as a trigger for the self-assembly of nanorods. Thomas *et al.*[37d] utilized α,ω-alkanedithiols as bridge to connect nanorods to form chains. The kinetic investigation of the formation of nanochains suggested that the assembly process was reaction-controlled due to the large activation energy of nanorod dimerization. Their further work[41] demonstrated that the angle of the nanochain can be modified by changing the rigidity of the bridge molecules (1,2-phenylenedimethanethiol and 1,6-hexanedithiol), which was promising in the studies of plasmon coupling effects (where the coupling of nanorods in well-defined arrays affects particularly the wavelength of loggitudinal SPR band) depending on the packing mode of the nanorods.

Bio-recognition systems are also a promising approach for the assembly of nanorods. The interactions between bioorganic molecules such as oligonucleotides[42], avidin-biotin [37a, 43], and antibody-antigen binding[37c, 44] have been investigated as the driving force for the self-assembly of nanorods. Mann *et al.*[42a] reported gold nanorods functionalized with thiolated complementary oligonucleotides. As a result, large-scale uniaxial organization

of metallic nanorods was tailored by using the specific DNA duplex hybridization formation. With the same strategy, Pan *et al.* [42b] obtained end-to-end self-assembly of gold nanorods. Instead of using complementary oligonucleotides in the earlier report, Pan *et al.* functionalized nanorods with non-complementary thiolated oligonucleotides, and the self-assembly was triggered by adding a target oligonucleotide, which is half-complementary with the immobilized molecules on the nanorods, to construct assemblies (Fig.1.15).

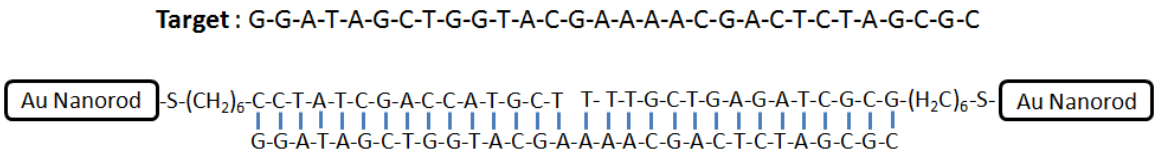

Figure 1.151. Scheme of assembly of oligonucleotide functionalized gold nanorods triggered by adding a target oligonucleotide. (Adapted from ref. 42b)

1.3.2 Self-Assembly of Nanoparticles Guided by Liquid Crystals

Liquid crystals doped with nanoparticles have been investigated for some time and frequently show altered electro-optical properties in emerging display related applications[5, 45]. On the other hand, nanoparticles can show enhanced self-assembly behavior guided by liquid crystal molecules. The first successful attempt of orienting 1D carbon nanotubes (CNTs) was reported by Patrick *et al.*[46]. They have demonstrated that well-established alignment approaches for liquid crystals such as grooved surface and an external magnetic field can be employed for manipulating the orientation of single or multi-walled carbon nanotubes dispersed in room-temperature nematic liquid crystals. Dierking *et al.*[47] further demonstrated that the orientational behavior of carbon nanotubes can be preselected and determined through the self-ordering properties of a nematic LC host,

and the dispersed carbon nanotubes can be reoriented by reorienting the LC director field. Lagerwall *et al.*[48] reported successful uniform alignment of carbon nanotubes dispersed in lyotropic liquid crystals at a relatively large concentration. In order to improve the stability of carbon nanotubes dispersions in LCs, Lagerwall *et al.*[49] indicated that the choice of the molecular structure of the LC host is critical. They also designed functional molecules for stabilizing CNT-LC dispersions, which were composed of a polyaromatic CNT-anchoring group connected with a targeted nematic LC mesogenic unit via a flexible spacer. Kumar *et al.*[50] fabricated single-walled CNTs with triphenylene based discotic LCs and discovered an improved stability of CNTs dispersed in host discotic LCs with a fairly high doping concentration of up to 10% by weight. A minor shift of the phase transition temperatures of the host discotic LC after doping was confirmed by DSC and XRD, and these results proved that the order of the plastic hexagonal columnar phase (Col_p) is destroyed to give normal hexagonal columnar (Col_h) phase. More interestingly, XRD data supported a change in *d*-spacing of the inter-columnar distance. The intercalation of functionalized CNTs into the matrix of the discotic LC host caused a significant shift of the inter-columnar *d*-spacing (increase from 1.60 to 2.39 nm (Fig.1.16).

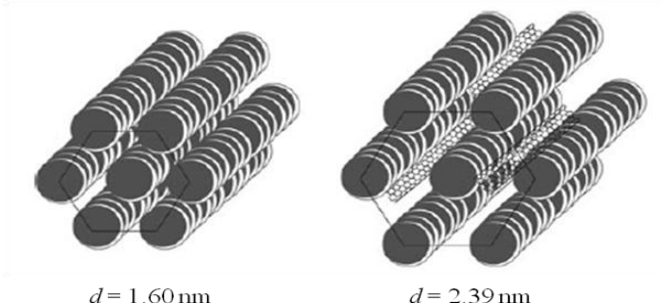

Figure 1.16. Schematic illustration of the insertion of CNTs into hexagonal columnar supermolecular order of a discotic LCs. (reprinted with permission from ref. 50)

Studies focusing on liquid crystal functinalized metallic nanoparticles have also been conducted in the search for novel LC-nanocomposite materials. Mehl *et al.*[51] fabricated gold nanoparticles (~2 nm in diameter) functionalized with a monolayer of calamitic nematic LC mesogens. The functionalization process was achieved by a two-step approach. The gold nanoparticles were first coated with thiolated hydrocarbon chains, and then converted to the desired system by adding thiolated nematic LC molecules. The resulting hybrid materials are chemically stable and exhibit nematic phase behavior observed by DSC and POM. Their further work[52] on this hybrid system discovered 3D ordered strings built by gold nanoparticles coated with LC mesogens (Fig.1.17). The functionalized gold nanoparticles are covered with laterally attached nematogenic LC ligands and alkyl thiols at a ratio of 2:3.

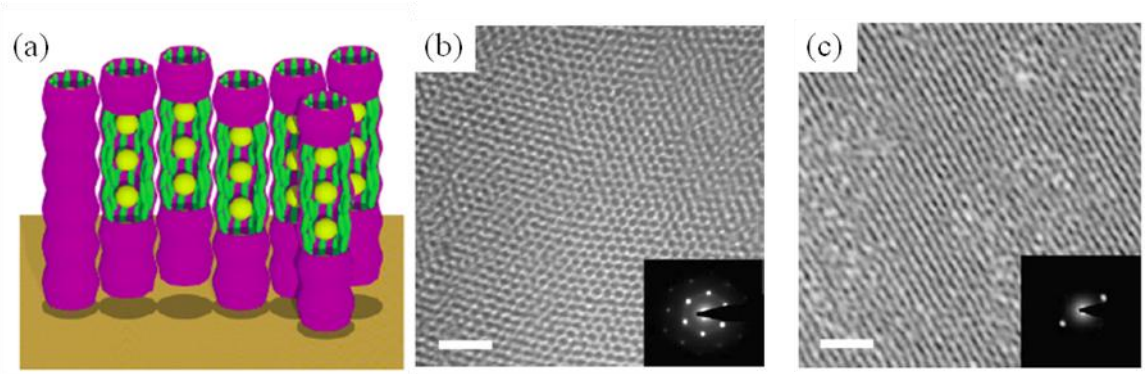

Figure 1.17. 3D assembly of gold nanoparticle coated with nematic LC ligands. a) Schematic illustration of the strings of gold nanoparticles jacketed with LC ligands; b) and c) are the TEM images from different tilted angles, insets are the corresponding electron-diffraction patterns. Scale bar = 20 nm. (Reprinted with permission from ref. 52)

Gold nanoparticles functionalized with triphenylene-based mesogenic groups were synthesized and studied as well[53]. Yamada *et al.*[53b] succeeded to achieve a controllable hexagonal self-assembly of triphenylene functionalized gold nanoparticles by changing

solvent polarities (Fig.1.18). The packing models of the triphenylene group due to the π-π interaction vary in different solvents and thus produce various self-assembled structures of the nanoparticles. Kumar *et al.*[53a, 53c] doped triphenylene functionalized gold nanoparticles into LCs and discovered that their insertion into a columnar matrix of discotic LC hosts contributed to the improvement of the conductivity of more than six orders of magnitude compared with the neat LCs. Further work by the same group[53c, 54] demonstrated that hexagonal columnar LC phases based on hexpentyloxytriphenylene molecules forming nanoribbons out of chloroform-methanol solutions show even further enhanced conductivity values after doping with triphenylene LC-functionalized gold nanorods.

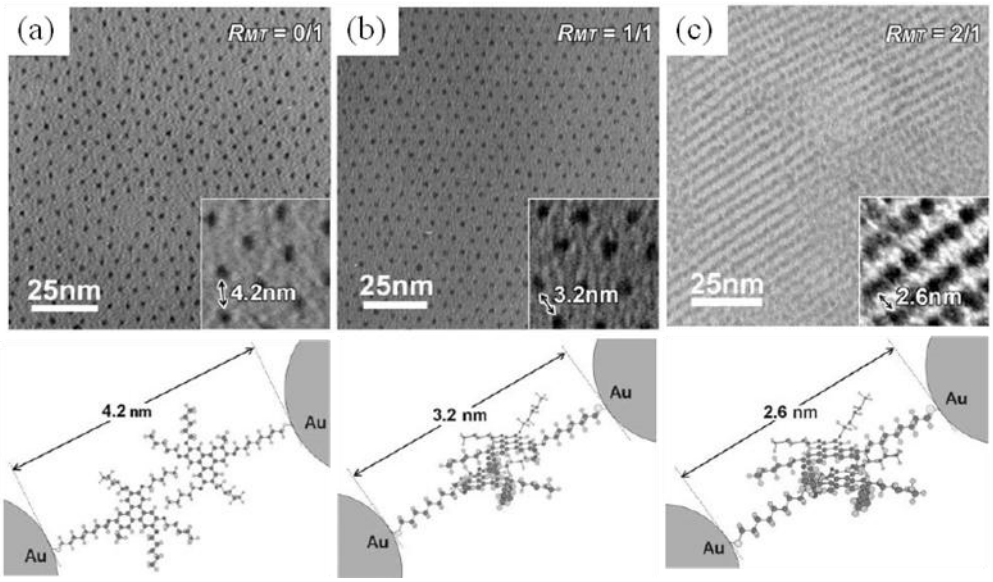

Figure 1.18. Self-assembly of triphenylene functionalized gold nanoparticles controlled by solvent polarity. R_{MT} stands for the ratio of methanol and toluene. (Reprinted with permission from ref. 53b)

1.4 Thesis Overview

The work of this thesis focuses on the synthesis of gold nanorods, their functionalization with LCs ligands through a versatile silane condensation approach, the self-assembly be-

havior of these LC-functionalized gold nanorods and their dispersion and alignment in the parent LC hosts.

Chapter 2 presents a large area self-assembly of nematic LC-functionalized gold nanorods. Two kinds of nematic LC functional ligands were used, terminal and lateral, decided by the anchoring chain to the nanorods, either parallel or perpendicular to the long molecular axis of the LC ligands. The self-assembly in monolayers was first investigated by TEM. The bulk phase packing model was tested by SAXS for both kinds of gold nanorods. Furthermore, the response of these nematic LC functionalized gold nanorods to an external magnetic field was investigated.

Chapter 3 focuses on the fabrication and investigation of discotic LC-functionalized gold nanorods (DLC-GNRs). A triphenylene-based discotic LC was chosen as the functional ligand. Again, the monolayer and bulk self-assembly behavior was investigated by TEM and SAXS, respectively. Mixtures of DLC-GNRs and DLC were made and filled in planar alignment cells. Polarized vis-NIR spectrophotometry was employed to investigate the orientation of the embedded DLC-GNRs, and SAXS was used to analyze the phase parameters of the doped DLC.

References

[1] F. Reinitzer, *Monatshefte für Chemie (Wien)* **1888**, *9*, 421.

[2] O. Lehmann, *Z. Physik Chem.* **1889**, *4*, 462.

[3] G. H. Brown, W. G. Shaw, *Chem. Rev.* **1957**, *57*, 1049-1157.

[4] C. W. Oseen, *Trans. Faraday Soc.* **1933**, *29*, 883-899.

[5] T. Hegmann, H. Qi, V. M. Marx, *J. Inorg. Organomet. Polym. Mater.* **2007**, *17*, 483-508.

[6] a) B. Bahadur, *Handbook of Liquid Crystals, 1st Edition*, J. W. Goodby, D. Demus, G. Gray, H.-W. Spiess, V. Vill (Eds.), Vol. 2A, pp. 257-302, Wiley-VCH, Weinheim, Germany **1998**; b) P. G. de Gennes, J. Prost, *The physics of Liquid Crystals, 2nd Edition*, Oxford University Press, USA **1993**.

[7] G. W. Gray, J. W. Goodby, *Smectic Liquid Crystals: Textures and Structures*, Thompson Sci., **1984**.

[8] S. Chandrasekhar, B. K. Sadashiva, K. A. Suresh, *Pramana* **1977**, *9*, 471-480.

[9] H. Monobe, S. Mima, T. Sugino, Y. Shimizu, M. Ukon, *Liq. Crys.* **2001**, *28*, 1253-1258.

[10] H. Monobe, K. Awazu, Y. Shimizu, *Thin Solid Films* **2009**, *518*, 762-766.

[11] S. Ikeda, Y. Takanishi, K. Ishikawa, H. Takezoe, *Mol. Cryst. Liq. Crys. A* **1999**, *329*, 1201-+.

[12] Y. Uchida, R. Tamura, N. Ikuma, S. Shimono, J. Yamauchi, Y. Shimbo, H. Takezoe, Y. Aoki, H. Nohira, *J. Mater. Chem.* **2009**, *19*, 415-418.

[13] a) http://www.dc.engr.scu.edu/cmdoc/rm_doc/02_Material_props.html; b) http://plc.cwru.edu/tutorial/enhanced/files/lc/phase/phase.htm; c) http://www.microscopyu.com/articles/polarized/polarizedintro.html; d) http://en.wikipedia.org/wiki/Bragg's_law; e) http://chemistry.about.com/od/growingcrystals/ig/Crystal-Photo-Gallery/Liquid-Crystal-Nematic-Phase.htm; f) http://www.lcinet.kent.edu/ilcs/main/page137/page214/page140/page140.html.

[14] I. Dierking, *Textures of Liquid Crystals*, Wiley-VCH, Weinheim, **2003**.

[15] M. A. El-Sayed, *Acc. Chem. Res.* **2001**, *34*, 257-264.

[16] S. Eustis, M. A. El-Sayed, *Chem. Soc. Rev.* **2006**, *35*, 209-217.

[17] I. E. Sendroiu, M. E. Warner, R. M. Corn, *Langmuir* **2009**, *25*, 11282-11284.

[18] C. L. Wu, Q. H. Xu, *Langmuir* **2009**, *25*, 9441-9446.

[19] P. K. Jain, X. H. Huang, I. H. El-Sayed, M. A. El-Sayed, *Acc. Chem. Res.* **2008**, *41*, 1578-1586.

[20] Y. N. Xia, P. D. Yang, Y. G. Sun, Y. Y. Wu, B. Mayers, B. Gates, Y. D. Yin, F. Kim, Y. Q. Yan, *Adv. Mater.* **2003**, *15*, 353-389.

[21] N. R. Jana, L. Gearheart, C. J. Murphy, *J. Phys. Chem. B* **2001**, *105*, 4065-4067.

[22] C. J. Murphy, T. K. San, A. M. Gole, C. J. Orendorff, J. X. Gao, L. Gou, S. E. Hunyadi, T. Li, *J. Phys. Chem. B* **2005**, *109*, 13857-13870.

[23] B. Nikoobakht, M. A. El-Sayed, *Chem. Mater.* **2003**, *15*, 1957-1962.

[24] T. K. Sau, C. J. Murphy, *Langmuir* **2004**, *20*, 6414-6420.

[25] A. Gole, C. J. Murphy, *Chem. Mater.* **2004**, *16*, 3633-3640.

[26] X. C. Ye, L. H. Jin, H. Caglayan, J. Chen, G. Z. Xing, C. Zheng, V. Doan-Nguyen, Y. J. Kang, N. Engheta, C. R. Kagan, C. B. Murray, *ACS Nano.* **2012**, *6*, 2804-2817.

[27] S. Koeppl, F. P. V. Koch, W. Caseri, R. Spolenak, *J. Mater. Chem.* **2012**, *22*, 14594-14601.

[28] M. Hu, J. Y. Chen, Z. Y. Li, L. Au, G. V. Hartland, X. D. Li, M. Marquez, Y. N. Xia, *Chem. Soc. Rev.* **2006**, *35*, 1084-1094.

[29] a) C. Burda, X. B. Chen, R. Narayanan, M. A. El-Sayed, *Chem. Rev.* **2005**, *105*, 1025-1102; b) M. Sastry, M. Rao, K. N. Ganesh, *Acc. Chem. Res.* **2002**, *35*, 847-855; c) C. N. R. Rao, G. U. Kulkarni, P. J. Thomas, P. P. Edwards, *Chem. Soc. Rev.* **2000**, *29*, 27-35; d) M. P. Pileni, *J. Phys. Chem. B* **2001**, *105*, 3358-3371; e) R. L. Whetten, M. N. Shafigullin, J. T. Khoury, T. G. Schaaff, I. Vezmar, M. M. Alvarez, A. Wilkinson, *Acc. Chem. Res.* **1999**, *32*, 397-406; f) A. N. Shipway, M. Lahav, I. Willner, *Adv. Mater.* **2000**, *12*, 993-998; g) S. A. Maier, M. L. Brongersma, P. G. Kik, S. Meltzer, A. A. G. Requicha, H. A. Atwater, *Adv. Mater.* **2001**, *13*, 1501-1505.

[30] C. J. Kiely, J. Fink, M. Brust, D. Bethell, D. J. Schiffrin, *Nature* **1998**, *396*, 444-446.

[31] a) M. Brust, C. J. Kiely, *Colloid Surface A* **2002**, *202*, 175-186; b) V. G. Veselago, E. E. Narimanov, *Nat. Mater.* **2006**, *5*, 759-762.

[32] a) J. T. Hu, T. W. Odom, C. M. Lieber, *Acc. Chem. Res.* **1999**, *32*, 435-445; b) Y. Cui, C. M. Lieber, *Science* **2001**, *291*, 851-853; c) N. I. Kovtyukhova, T. E. Mallouk, *Chem. Eur. J.* **2002**, *8*, 4355-4363.

[33] J. Zhang, Zhong-lin Wang, Jun Liu et al., *Self-Assembled Nanostructures*, Kluwer Academic/ Plenum Publishers **2003.**

[34] K. Liu, N. N. Zhao, E. Kumacheva, *Chem. Soc. Rev.* **2011**, *40*, 656-671.

[35] K. J. Stebe, E. Lewandowski, M. Ghosh, *Science* **2009**, *325*, 159-160.

[36] a) R. L. Whetten, J. T. Khoury, M. M. Alvarez, S. Murthy, I. Vezmar, Z. L. Wang, P. W. Stephens, C. L. Cleveland, W. D. Luedtke, U. Landman, *Adv. Mater.* **1996**, *8*, 428-433; b) W. D. Luedtke, U. Landman, *J. Phys. Chem.* **1996**, *100*, 13323-

13329; c) C. J. Kiely, J. Fink, J. G. Zheng, M. Brust, D. Bethell, D. J. Schiffrin, *Adv. Mater.* **2000**, *12*, 640-643; d) J. Fink, C. J. Kiely, D. Bethell, D. J. Schiffrin, *Chem. Mater.* **1998**, *10*, 922-926.

[37] a) K. K. Caswell, J. N. Wilson, U. H. F. Bunz, C. J. Murphy, *J. Am. Chem. Soc.* **2003**, *125*, 13914-13915; b) M. H. Zareie, X. D. Xu, M. B. Cortie, *Small* **2007**, *3*, 139-145; c) J. Y. Chang, H. M. Wu, H. Chen, Y. C. Ling, W. H. Tan, *Chem. Commun.* **2005**, 1092-1094; d) S. T. S. Joseph, B. I. Ipe, P. Pramod, K. G. Thomas, *J. Phys. Chem. B* **2006**, *110*, 150-157; e) X. G. Hu, W. L. Cheng, T. Wang, E. K. Wang, S. J. Dong, *Nanotechnology* **2005**, *16*, 2164-2169; f) H. Nakashima, K. Furukawa, Y. Kashimura, K. Torimitsu, *Chem. Commun.* **2007**, 1080-1082; g) D. Baranov, A. Fiore, M. van Huis, C. Giannini, A. Falqui, U. Lafont, H. Zandbergen, M. Zanella, R. Cingolani, L. Manna, *Nano. Lett.* **2010**, *10*, 743-749.

[38] a) K. Liu, Z. H. Nie, N. N. Zhao, W. Li, M. Rubinstein, E. Kumacheva, *Science* **2010**, *329*, 197-200; b) N. Zhao, K. Liu, J. Greener, Z. H. Nie, E. Kumacheva, *Nano. Lett.* **2009**, *9*, 3077-3081; c) Z. H. Nie, D. Fava, E. Kumacheva, S. Zou, G. C. Walker, M. Rubinstein, *Nat. Mater.* **2007**, *6*, 609-614.

[39] K. G. Thomas, S. Barazzouk, B. I. Ipe, S. T. S. Joseph, P. V. Kamat, *J. Phys. Chem. B* **2004**, *108*, 13066-13068.

[40] P. K. Sudeep, S. T. S. Joseph, K. G. Thomas, *J. Am. Chem. Soc.* **2005**, *127*, 6516-6517.

[41] P. Pramod, K. G. Thomas, *Adv. Mater.* **2008**, *20*, 4300-4305.

[42] a) E. Dujardin, L. B. Hsin, C. R. C. Wang, S. Mann, *Chem. Commun.* **2001**, 1264-1265; b) B. F. Pan, L. M. Ao, F. Gao, H. Y. Tian, R. He, D. X. Cui, *Nanotechnology* **2005**, *16*, 1776-1780.

[43] A. Salant, E. Amitay-Sadovsky, U. Banin, *J. Am. Chem. Soc.* **2006**, *128*, 10006-10007.

[44] L. B. Wang, Y. Y. Zhu, L. G. Xu, W. Chen, H. Kuang, L. Q. Liu, A. Agarwal, C. L. Xu, N. A. Kotov, *Angew. Chem. Int. Edit.* **2010**, *49*, 5472-5475.

[45] a) H. Qi, A. Lepp, P. A. Heiney, T. Hegmann, *J. Mater. Chem.* **2007**, *17*, 2139-2144; b) M. Urbanski, B. Kinkead, H. Qi, T. Hegmann, H. S. Kitzerow, *Nanoscale* **2010**, *2*, 1118-1121; c) H. Qi, T. Hegmann, *J. Am. Chem. Soc.* **2008**, *130*, 14201-14206; d) H. Qi, B. Kinkead, T. Hegmann, *Adv. Funct. Mater.* **2008**, *18*, 212-221; e) A. Lapanik, A. Rudzki, B. Kinkead, H. Qi, T. Hegmann, W. Haase, *Soft Matter* **2012**, *8*, 8722-8728.

[46] M. D. Lynch, D. L. Patrick, *Nano. Lett.* **2002**, *2*, 1197-1201.

[47] I. Dierking, G. Scalia, P. Morales, D. LeClere, *Adv. Mater.* **2004**, *16*, 865-869.

[48] a) J. Lagerwall, G. Scalia, M. Haluska, U. Dettlaff-Weglikowska, S. Roth, F. Giesselmann, *Adv. Mater.* **2007**, *19*, 359-364; b) J. P. F. Lagerwall, G. Scalia, *J. Mater. Chem.* **2008**, *18*, 2890-2898.

[49] a) M. Kuhnast, C. Tschierske, J. Lagerwall, *Chem. Commun.* **2010**, *46*, 6989-6991; b) S. Schymura, M. Kuhnast, V. Lutz, S. Jagiella, U. Dettlaff-Weglikowska, S. Roth, F. Giesselmann, C. Tschierske, G. Scalia, J. Lagerwall, *Adv. Funct. Mater.* **2010**, *20*, 3350-3357.

[50] S. Kumar, H. K. Bisoyi, *Angew. Chem. Int. Edit.* **2007**, *46*, 1501-1503.

[51] a) L. Cseh, G. H. Mehl, *J. Am. Chem. Soc.* **2006**, *128*, 13376-13377; b) L. Cseh, G. H. Mehl, *J. Mater. Chem.* **2007**, *17*, 311-315.

[52] X. B. Zeng, F. Liu, A. G. Fowler, G. Ungar, L. Cseh, G. H. Mehl, J. E. Macdonald, *Adv. Mater.* **2009**, *21*, 1746-1750.

[53] a) S. Kumar, S. K. Pal, P. S. Kumar, V. Lakshminarayanan, *Soft Matter* **2007**, *3*, 896-900; b) M. Yamada, Z. R. Shen, M. Miyake, *Chem. Commun.* **2006**, 2569-2571; c) S. Kumar, *Liq. Crys.* **2014**, *41*, 353-367.

[54] B. S. Avinash, V. Lakshminarayanan, S. Kumar, J. K. Vij, *Chem. Commun.* **2013**, *49*, 978-980.

[55] a) Y. Mao, M.E. Cates, H.N.W. Lekkerkerker , *Physica A* **1995**, *1-4***,** 10–24;

Chapter 2

Large Area Self-Assembly of Nematic Liquid-Crystal-Functionalized Gold Nanorods

Large Area Self-Assembly of Nematic Liquid Crystal-Functionalized Gold Nanorods

Umadevi Shivakumar[1+], Xiang Feng[1], and Torsten Hegmann[1]*

[1] Department of Chemistry, University of Manitoba, Winnipeg, MB, R3T 2N2, Canada

[*] Chemical Physics Interdisciplinary Program, Liquid Crystal Institute, Kent State University, Kent, OH 44242, USA, E-mail: thegmann@kent.edu

[+] Present address: Central Electrochemical Research Institute, Karaikudi-630 006, Tamilnadu, India

Reproduced with the permission from *Adv. Funct. Mater.* **2013**, *23*, 1393-1403.

 DOI: 10.1002/adfm.201202727

Authors' Contributions

The idea of liquid crystal-functionalized gold nanorods was conceptualized by Dr. Torsten Hegmann. Dr. Umadevi Shivakumar synthesized LC2 silane and LC2-GNRs, conducted TEM, POM experiment on LC2-GNRs. Xiang Feng conducted the synthesis of CTAB-GNRs, developed the silane condensation reaction for attaching LC ligands to GNRs, synthesized LC1 silane and LC1-GNRs, obtained TEM images of LC1-GNRs, conducted SAXS of LC1-GNRs and LC2-GNRs, investigated alignment behavior of LC1-GNRs under strong magnetic field. The original manuscript was prepared by US without data of LC1-GNRs. TH and XF wrote the full paper, as well as the revisions according to the suggestions from the reviewers of *Adv. Funct. Mater.*

Abstract

Fascinating nematic- and smectic-like self-assembled arrays are observed for gold nanorods partially capped with either laterally or terminally attached nematic liquid crystals upon slow evaporation of an organic solvent on TEM grids. These arrays can be manipulated and reoriented by applying an external magnetic field from quasi-planar to vertical similar to a Fréedericksz transition of common organic nematic liquid crystals. Birefringence and thin film textures of these self-assembled gold nanorod arrays observed by polarized optical microscopy are strongly reminiscent of common organic nematic liquid crystal textures between crossed polarizers and, additionally, support the formation of ordered liquid crystal-like anisotropic superstructures. The ordering within these arrays is also confi rmed in bulk samples using small angle X-ray scattering (SAXS).

2.1 Introduction

In the last few years, anisotropic metal nanostructures attract a great deal of interest compared to their spherical counterparts owing to their unique shape dependent properties such as multiple plasmon bands, light absorption in the near infrared, enhanced electromagnetic fields at nanorod tips among others, promising various potential applications in optics and photonics. [1–7] Gold nanorods (GNRs), in particular have gained significant interest due to their proven applications in sensing, [2–5] cellular imaging [3,8] and cancer therapy. [9] Obtaining ordered assemblies of GNRs over an extended area is an active research topic in nanoscience since the resulting enhanced collective properties of such assemblies differ from the properties of their individual components. Organized GNR assemblies have attractive applications in surface-enhanced Raman spectroscopy and fluorescence sensing. [10] Although great advances have been made regarding the self-assembly of spherical metal nanoparticles, obtaining organized arrays of anisotropic nanorods with a tunable shape and size is still a challenging task because their assembly requires both orientational and positional ordering. Several strategies have been pursued to organize anisotropic nanorods into ordered superstructures. [4–6] Nikoobakth et al. reported superlattices of GNRs by employing a mixture of the surfactants hexadecyltrimethylammonium bromide (HTAB) and tetraoctylammonium bromide (TOAB) as capping ligands. [11] The Langmuir-Blodgett technique was used by Kim and coworkers to demonstrate a pressure induced isotropic-nematic-smectic transitions of inorganic nanorods. [12] Solvent evaporation on TEM grid was shown to result in the assem-

bly of CTAB stabilized GNRs by Sau and Murphy. [13] Sreeprasad et al. utilized the charge neutralization of CTAB-capped GNRs by dimercaptosuccinic acid and EDTA, ultimately leading to the formation of one-, two-, and three-dimensional superstructures of GNRs. [14] Two- and three-dimensional arrays of hydrophobic GNRs by solvent evaporation on a substrate were also reported by Mitamura and co-workers. [15] One of the first examples using soft matter templates was the self-assembly of GNRs into 1D and 2D structures using DNA as template. [16] More recently, three-dimensional superstructures of (1-mercaptoundec-11-yl)-hexa(ethylene glycol)-capped GNRs having a local smectic B order have been described by Hamon et al. [17] They employed a novel drying method in which GNRs crystallization was carried out between smooth surfaces and a topographically patterned stamp.

In many of these above-mentioned systems, the assembly formation is carried out in aqueous medium and further manipulation of the formed assembly is quite difficult or impossible. Therefore, a versatile method for the large scale organization of GNRs allowing for simultaneous formation and control over the morphology of the final self-assembled superstructure would be a great advantage for technological application of these materials.

Herein, we describe a novel strategy to assemble GNRs into ordered superstructures by chemically functionalizing GNRs with an aspect ratio of about four with thermotropic nematic liquid crystals (LCs) simultaneously acting as stabilizing ligand as well as tunable template. Nematic LCs are one-dimensionally ordered fluids whose anisotropic structures gives rise to unique orientational, optical and electro-optical properties that can be easily controlled by external stimuli such as electric or magnetic fields. By associating

LCs with nanoparticles it is possible to impart order and fluidity to nanosystems. More importantly, however, the final self-assembled LC-hybrid nanostructure can be manipulated by external stimuli to bring about morphological changes. All three major type of thermotropic LCs namely the rod-, [18–25] disc- [26,27] and bent-core [28] LCs have been covalently attached to gold nanoparticles (GNPs) and these systems were found to exhibit remarkable self-assembly behavior either on a substrate or in the bulk. LCs have also proven to be promising candidates to assemble GNRs. Park et al. [29] described the self-organization of GNRs either in side-by-side or end-to-end fashion using self-assembled stacks of lyotropic chromonic LC materials. Liu and co-workers [30] demonstrated the bulk alignment of GNRs dispersed in surfactant-based lyotropic LCs and their realignment by shearing or application of a magnetic field. Very recently, we have reported the magnetic field induced formation of self-assembled arrays of nematic LC functionalized GNRs with the mesogens attached to the nanorod surface at one of the terminal hydrocarbon chains via a siloxane linkage (**LC1**), i.e., mesogens and GNR long axes are in theory perpendicular to one another (Figure 2.1a). [31] The silane conjugation approach provides access to thermally and chemically robust GNRs that do not aggregate in solution due to the small quantity of trapped surfactant (CTAB) allowing for sufficient electrostatic repulsion between the GNRs. In this particular case, the mesogens attached to the GNR surface align with the external magnetic field producing a planar array of the GNRs on the transmission electron microscopy (TEM) grid as shown in the TEM image and cartoon in Figure 1a. These examples clearly highlight the significance of LC molecules for the creation and manipulation of anisotropic nanostructures.

To further explore the role of the relative mesogen connectivity to the GNR surface and its impact on GNR self-organization, we synthesized GNRs where the thermotropic nematic mesogens are attached to the GNR surface via a lateral alkyl chain in a side-on rather than an end-on fashion (idealized, mesogen and GNR long axis are parallel), and studied their self-assembly upon slow solvent evaporation on substrates (Figure 2.1b). The preference for this particular ligand type to functionalize GNRs emerges from the fact that laterally substituted LC ligands show the tendency to induce nematic ordering when linked to large molecules such as polymers, dendrimers and even to quasi-spherical (polyhedral) gold nanoparticles (NPs) as shown by Cseh et al. [20] Extensive studies on the mesophase exhibited by these gold NPs revealed highly ordered rhombohedral or hexagonal columnar arrangements of the particles themselves. [22] In order to explain these experimental observations the authors proposed that in the mesophase the NPs are arranged in columns surrounded by a nematic sheath and that these columns spontaneously self-organize yielding complex periodic lattices. Such spatial arrangement would be an ideal platform for creating ordered superlattices of GNRs, by factually replacing the NP columns in Cseh's work with individual LC-capped GNRs (Figure 2.1b).

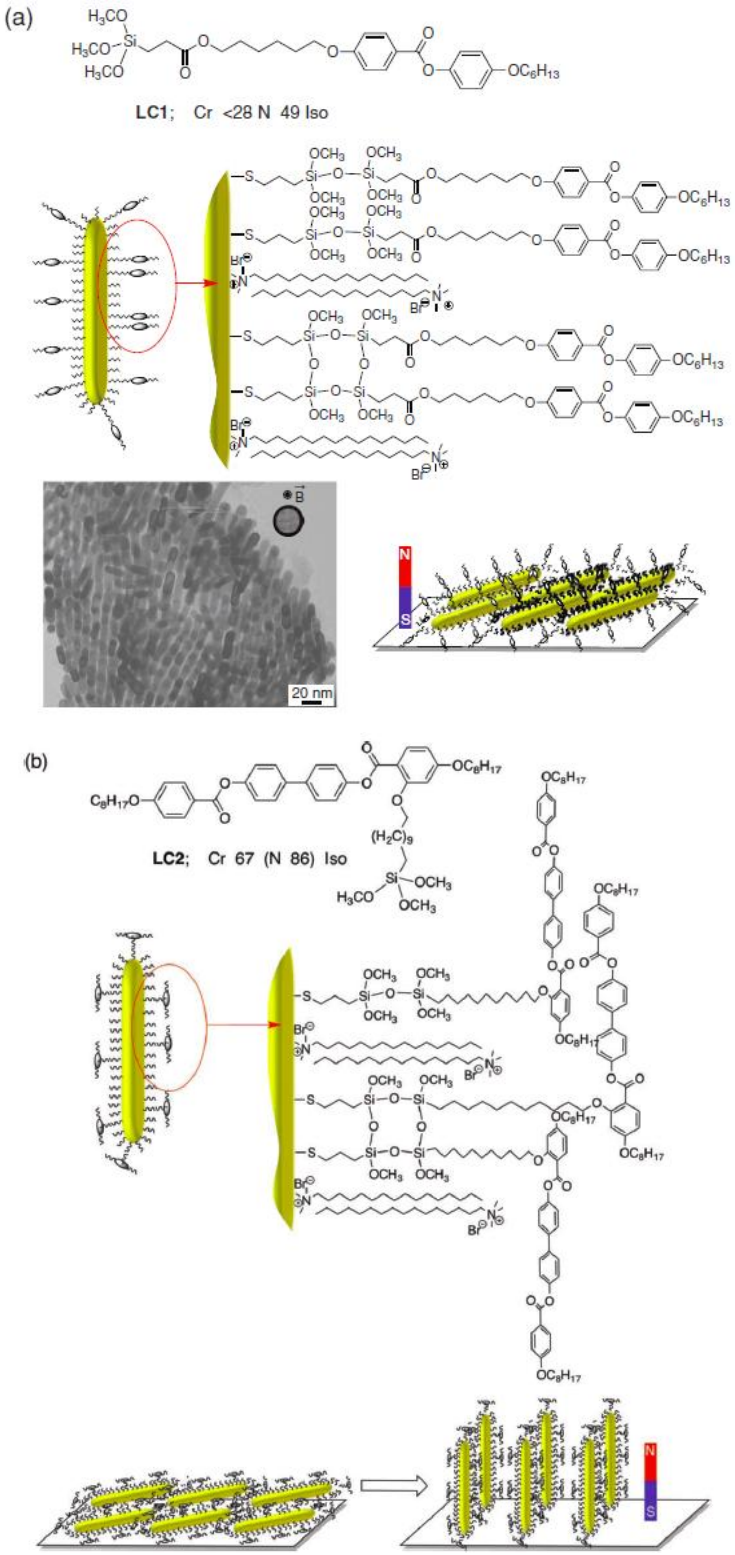

Figure 2.1. Schematic representation of nematic LC-functionalized GNRs and their observed or expected self-assembly upon slow evaporation of the solvent: a) end-on

mesogen attachment. The inset in the TEM image shows the orientation of the magnetic field with respect to the TEM grid [31] and b) Side-on mesogen attachment with the proposed Fr éedericksz-type transition of the LC-functionalized GNRs.

2.2 Results and Discussion

The precursor nematic LC (compound **1**) of the rod-shaped nematic siloxane LC2 features two octyloxy chains at the two terminal ends of the rod-like molecules and a vinyl-terminated lateral hydrocarbon chain. Compound **1** was prepared following a procedure previously reported in the literature. [32] The compound exhibits a nematic phase with the following phase transition temperatures (°C): Cr 91 N 146 Iso on heating (reported transition temperatures (°C): Cr 93 N 141 Iso) [33] and crystallizes well below room temperature on cooling. The terminal alkene of mesogen **1** was converted to a trimethoxysilane end group by a hydrosilylation reaction as shown in Figure 2a. The procedure followed to prepare silane **LC2** from **1** along with its analytical data are provided in the experimental section. POM observation of this silane showed a monotropic nematic phase with the following transition temperatures (°C): Cr 67 (N 86) Iso. The precursor CTAB stabilized GNRs were prepared at 30 °C by a single step, non-seeding method. [31,34] The rods were characterized by UV-Vis-NIR and TEM. The UV-Vis-NIR spectrum of these GNRs showed two absorption maxima, situated at 512 nm and 759 nm corresponding to the transversal surface plasma resonance (TSPR) and the longitudinal surface plasma resonance (LSPR), respectively (Figure 2.2c). The relative narrow width of the LSPR indicated the monodispersity of the formed nanorods, which was further confirmed by TEM imaging (Figure 2.2b), and the low degree of aggregation. It can be seen from the TEM image that the percentage of the unwanted spherical particles is comparatively low. The

length and diameter of the rods are 28.6 ± 2 nm and 6.5 ± 1.5 nm, respectively, leading to an aspect ratio of ≈ 4.3, as determined by TEM. Also, it is apparent from the image that the rods show only short-range side-by-side assembly with no in-plane correlation.

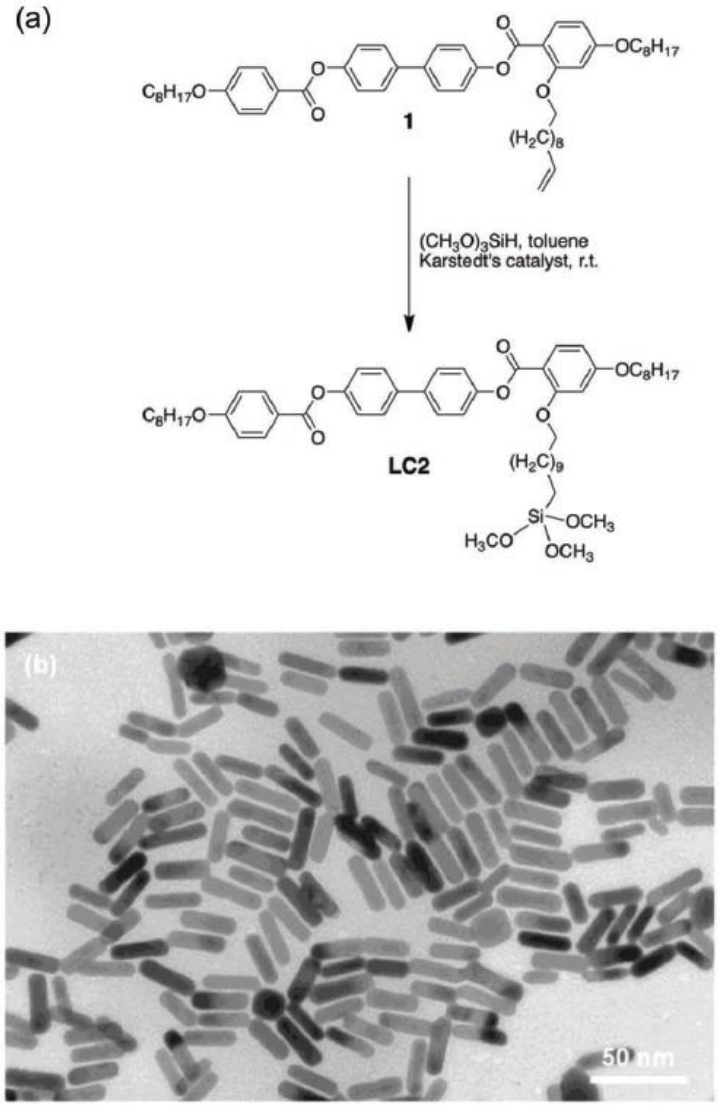

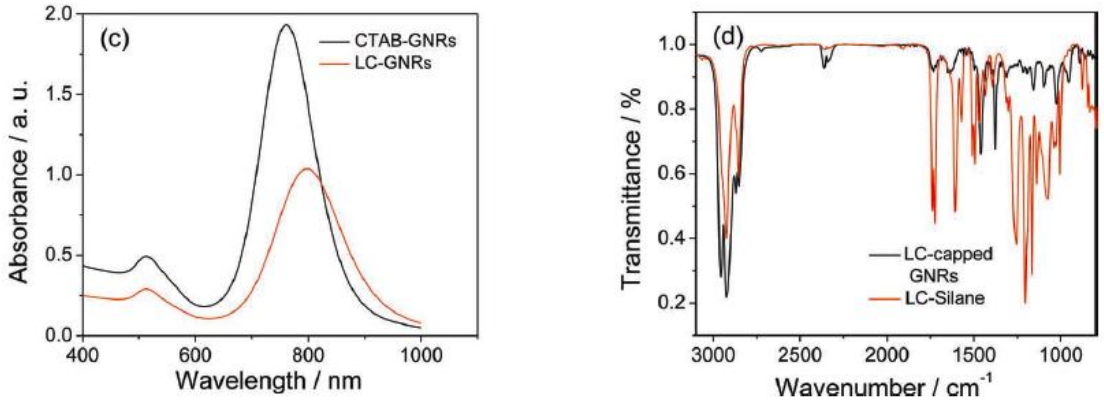

Figure 2.2. a) Synthesis of the LC silane LC2. b) TEM image obtained for CTAB stabilized GNRs in water. c) UV-Vis-NIR spectra recorded for the CTAB capped GNRs and LC2 -capped GNRs. d) Overlapped IR spectra of the LC2 -capped GNRs and LC-silane.

The exchange of the CTAB capping on the GNRs with the nematic silane **2** was carried out in a two-step silane condensation reaction as described by us recently. [31] In the first step, some of the CTAB ligands on the nanorod surface were replaced by a mercaptotrimethoxy silane (MPS), which binds to the GNR surface through a strong Au-S covalent linkage. In the second step, the nematic silane was added followed by base to bring about the hydrolysis of trimethoxy silane groups and subsequent condensation among the silanols to provide a stable, partial or patchy oligo(siloxane) network around the GNRs. The phase transfer of GNRs from aqueous to organic phase upon ligand exchange can be visually observed as a change in color of the aqueous and organic phases (see appendix A, Figure A1).

The capping exchange from CTAB to LC silane was confirmed by both UV-Vis-NIR spectrophotometry and IR spectroscopy. After the exchange process, the maximum of LSPR band red-shifted from 759 nm to 798 nm (Figure 2.2c), which is an indication of the change in the dielectric environment surrounding the GNRs. The maximum wave-

length, λ max, of the LSPR is particularly sensitive to changes in the surrounding dielectric (i.e., changes of the refractive index of the surrounding medium due to the nature of the coating; a CTAB vs. LC silane exchange leads an increase in the dielectric constant of the surrounding medium). [35] A red shift of the LSPR of around 30 nm is commonly observed for replacements of CTAB with other capping agents. [35,36] Further, IR provided clear evidence for the presence of the LC ligand on the nanorod surface. The IR spectrum obtained for the well-washed sample of LCcapped GNRs (no excess free LC silane) displayed all the bands characteristic of the LC-silane along with a Si-O-Si stretching vibration corresponding to siloxane bonds (Figure 2.2d). Overlapping the IR spectra of the LC-coated GNRs with that of the LC-silane clearly illustrates that the IR pattern of the former follows that of the latter with only one exception, the bands are slightly shifted to lower wavenumbers. The sharp bands at 2957, 2918, 2859, 1457, and 1378 cm^{-1} correspond to the antisymmetric stretching of CH_3 groups, antisymmetric stretching and symmetric stretching of CH_2 groups, bending mode of CH_2 groups and rocking vibrations of CH_3 groups, respectively. More importantly, the spectrum shows stretching bands at 1733 and 1158 cm^{-1} (and 1023 cm^{-1}) corresponding to ester – C = O and – C - O stretching modes. Further, the spectrum shows bands in the region 1000 – 1100 cm^{-1} (1096, 1025 and 953) that are due to the Si-O-Si stretching mode of the siloxane bond (1096 and 1025 cm^{-1}) and the Si-O-C stretching mode of trialkoxysilane groups (1090 and 953 cm^{-1}). Incidentally, corresponding peaks at almost matching wavenumbers have been reported for other silane condensations on GNRs [31] and other substrates (1090 cm^{-1} and 1033 cm^{-1}). [37] As seen from the spectrum, some of the bands recorded for functionalized GNRs are broad as expected for such hybrid nanomaterials. The occurrence the Si-O-C stretching

band in the GNR hybrid spectrum suggests the presence of non-hydrolyzed trimethoxy groups of the silane. However, the ^{1}H NMR spectrum of the supernatant obtained right after the coating exchange clearly indicated that overall at least one methoxy group of the silane was hydrolyzed and hence available for condensation. This analysis was performed by integrating the area under the peak at 3.6 ppm corresponding to the methoxy groups linked to the Si (see appendix A, Figure A2). The spectrum also showed that the ester linkages in the silane remain intact under the basic condition used for the silane condensation. Hence, only a partial or "patchy siloxane network" is formed during the two-step GNR surface modification step, which nonetheless produced GNRs that are thermally, chemically and colloidal stable over extended time periods.

To investigate if decorating GNRs with nematic LCs via lateral hydrocarbon spacers produces well-organized superstructures with one- or two-dimensionally ordered nematic and smectic-like morphologies we performed detailed, extensive TEM and high-resolution TEM studies.

A 2–3 μL drop of the colloidal solution of the once-washed GNR sample (taken from a 1 mL GNR dispersion containing ≈ 150 μL of 10 mM free ligand; i.e., about 5 wt% free vs 95 wt% bound to the GNR surface) in toluene was drop-casted on carbon-coated copper grids and allowed to dry under ambient conditions. Among the various solvent systems and solution concentrations examined for the self-assembly process, a highly concentrated sample (absorbance of the nanorod dispersion at 798 nm was ≈ 3.5 in a 1 cm path length cuvette) in toluene was found to give remarkable results. The observation of such a sample using TEM revealed highly ordered 3D superstructures of GNRs in almost every part of all grids investigated. In addition, assemblies with different morphologies

were seen in different regions of the same grid for any given sample. This might be due to the high concentration of the sample causing the thin solvent film to break into un-symmetrical regions over the grid before the solvent evaporation takes place, ultimately resulting in different local GNR concentrations. [13,38] Figure 2.3 shows representative TEM images of the densely packed, highly organized 3D patterns of the **LC2** coated GNRs. It can be seen from Figure 2.3a,b that the rods assume a staggered arrangement near the ends of the assembly; however they gradually translate to form an end-to-end, eclipsed chain-like pattern in the vicinity of the center. Further, it is interesting to point out here that these chains are spaced evenly next to each other. In this assembly, some of the rods appear to be shorter (for example, those circled in red) than their original size (rods circled in yellow), likely because these rods are oriented at an angle (between 0 and 90 °) to the substrate and not perfectly parallel to the substrate. Very few axially oriented (at a 90 ° angle) rods can also be seen at the top left corner (green circle) of the Figure 2.3a. Similar end-to-end attached parallel wavy structures of the rods in two different regions of the same grid, extending over several hundred nanometers are shown in Figure 3b, c. Another fascinating well-oriented multilayer 3D smectic-like pattern is shown in Figure 2.3d. The dark region towards the right side of the figure indicates the increased thickness of the assembly.

In other areas of the TEM grid, unique superstructures were observed in which smectic arrays of GNRs were self-assembled in two different fashions, situated next to each other as shown in Figure 2.4a. In the left region of Figure 2.4a the GNRs form parallel packed end-to-end connected chains extending over several hundred nanometers. The thickness of the assembly increases from top to bottom as indicated by the increased darkness at the

bottom regions of the image. The end-to-end eclipsed arrangement of the nanorods is so precise that these chains appear as perfectly uniform lines, making it very difficult to even visually isolate individual nanorods. Further, one can also see the regularity in the inter-chain distances. The right half of the figure displays a 3D smectic-like structure generated by a parallel orientation of the rods with respect to one another. In particular, this highly ordered structure consists of several layers of side-by-side arranged rods forming 3D assemblies (see multilayer pattern in the right top area of Figure 2.4 a).

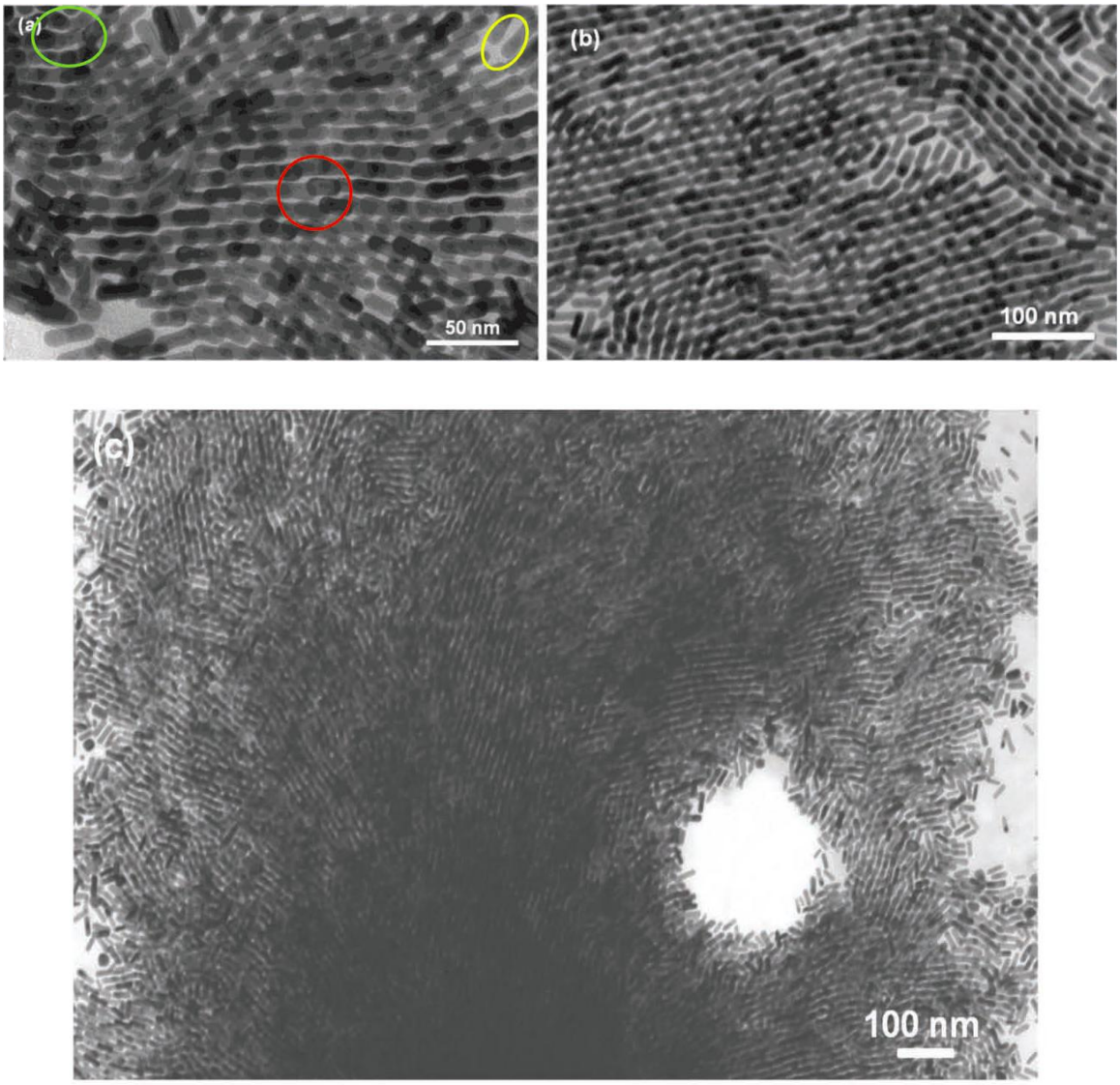

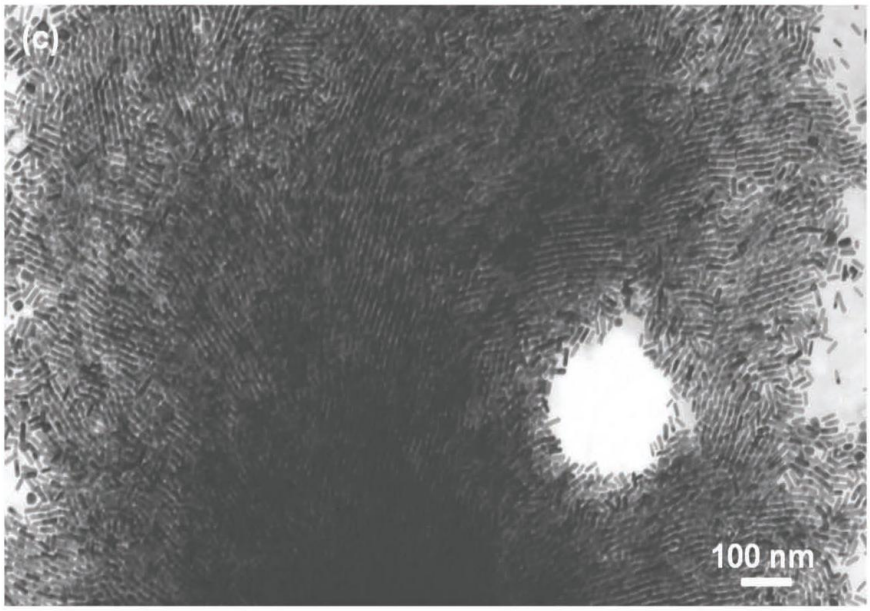

Figure 2.3. a–c) TEM images showing the highly organized assemblies of LC2 functionalized GNRs in different regions of the same grid. d) 3D smectic array of the GNRs.

More interestingly, in some parts of the grid, assemblies extending over several sq μm^2 were observed. One such remarkable superlattice of nanorods is shown in Figure 4b. The inset shows the electron diffraction pattern recorded from a part of this area. The observed ring pattern indicates that the entire self-assembly is composed of local ordered domains. Each domain has a superlattice structure with no in-plane orientational correlation among the domains, similar to a non-aligned nematic or smectic liquid crystalline phase. The various, local concentration-dependent packing type also prevented a clear assignment of the ordering of the GNRs in SAXS experiments, because different types of smectic- and nematic-like ordering coexist as shown in Figure 2.4.

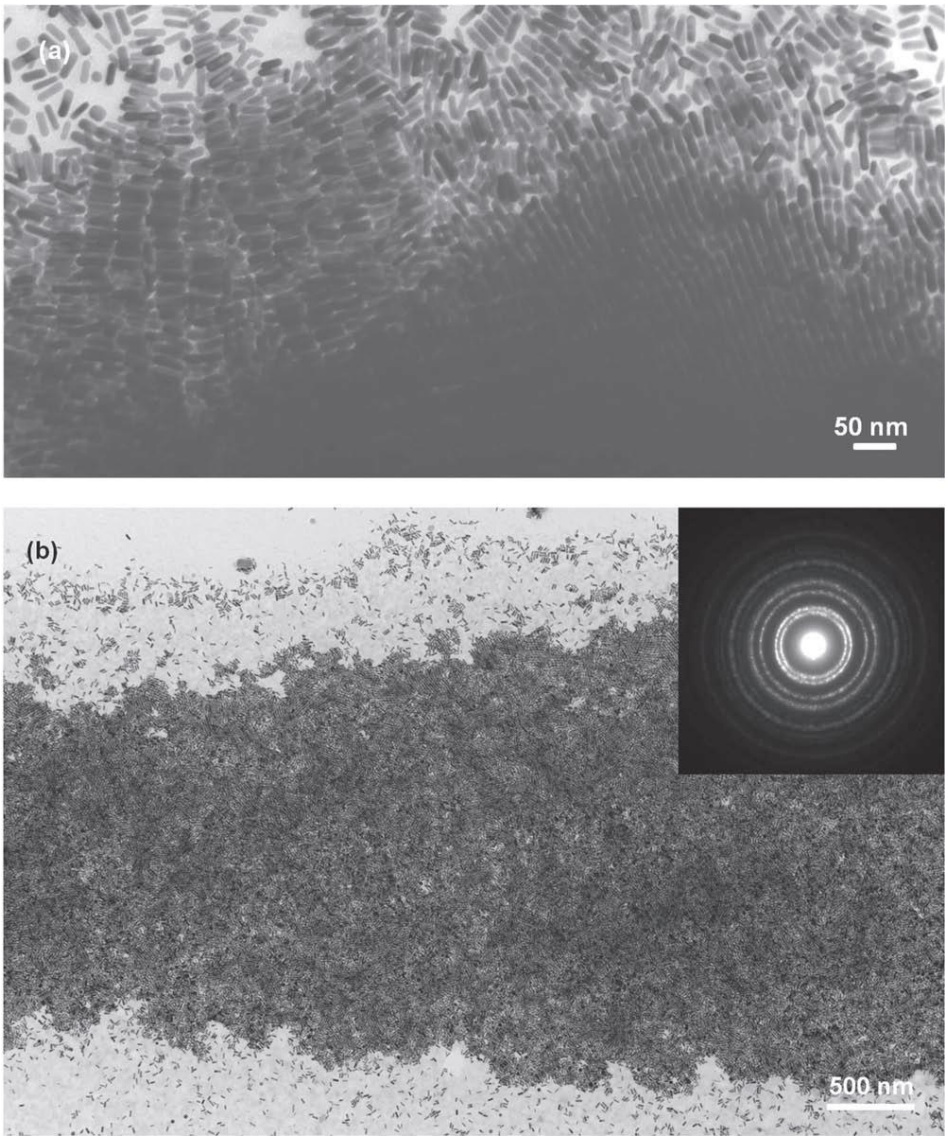

Figure 2.4. a) TEM image showing the smectic arrays of LC-capped GNRs arranged in two different fashions next to each other. b) A large area TEM image of the LC-coated GNRs displaying a micrometer scale assembly; inset shows the typical gold electron diffraction pattern (small selected spot size for selected area electron diffraction).

The distances between the GNRs in these assemblies were measured from intensity cross-section profiles of HR-TEM images. One such image is shown in Figure 2.5a. If we assume that the aromatic parts of the LC ligands on the neighboring GNRs overlap, then the distance between the adjacent rods in a side-by-side orientated assembly would corre-

spond to twice the length of the lateral chain connecting the LC ligand to the rod (total length including MPS + side chain of LC), which is ≈ 4.8 nm, calculated by assuming an all-trans conformation of the hydrocarbon chains in a 3D optimized structure (see appendix A, Figure A3). This value matches well with the measured distances between the rods in a staggered arrangement (from TEM), which was determined to be 4.5 ± 0.5 nm (Figure 2.5a). The colored lines at the top of the figure and in the center indicate the number of rods considered to plot the intensity cross-section profiles. The spacing between the end-to-end eclipsed rods in the middle of the assembly (Figure 2.5a) is surprisingly very small (≈ 1.63 nm) compared to those in the staggered conformation, which is initially puzzling. However, the experiments we performed by tilting the TEM grid (≈ 30 °, see Figure 2.5b, c) clearly indicate that these eclipsed rods still maintain a distance of around 4.5 nm between themselves, but they are oriented at an angle to the substrate (green circle in Figure 2.5c). Thus, it is the viewing angle that gives the false implication that the rods are overlapping on each other, while these rods are situated at an angle to the substrate and maintain a regular distance between them supporting the suggested 3D arrangement (for different projection elucidated by tilting experiments see Figure 2.5d). The same behavior is observed in most of the formed assemblies. These observations support the assumption that the rod-shaped aromatic parts of the LC ligands overlap (π-π interaction as a driving force) thereby bringing the rods together and inducing a high orientational influence on them. This would explain the perfect line-like assemblies (Figure 2.4a) formed from the end-to-end attached rods (slightly tilted rods). These results strongly suggest that tuning the number of attached LC ligands and hence their density on the rod surface,

should allow for inducing true, fluid nematic or smectic phase behavior in the composite, which is one of our future interests.

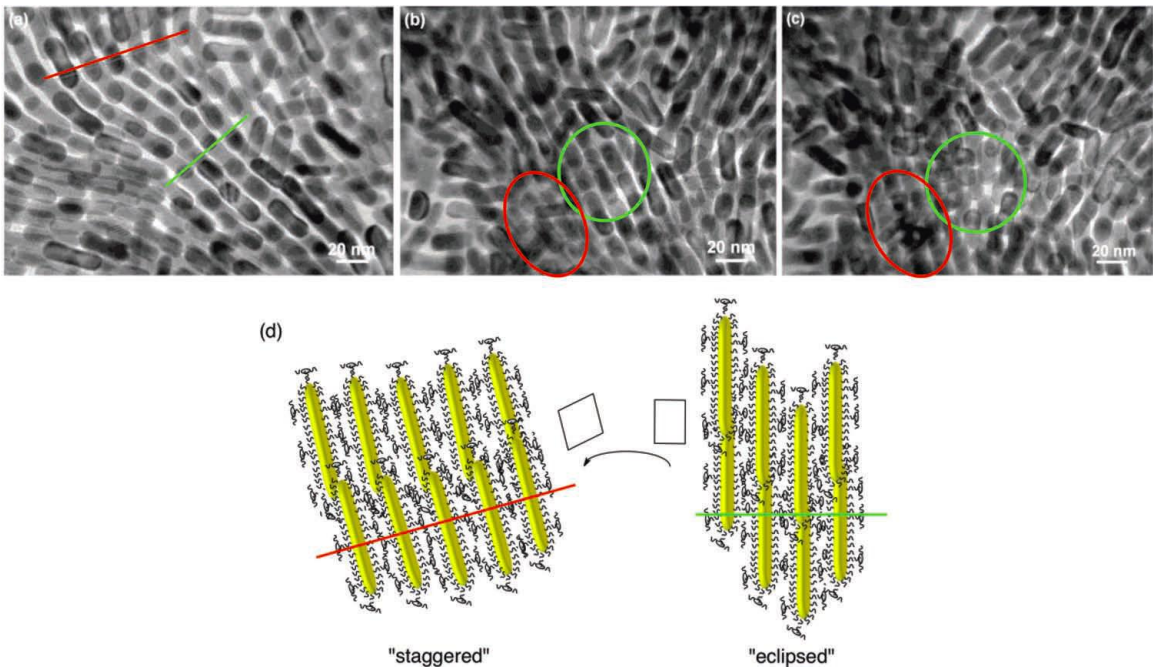

Figure 2.5. a) HR-TEM image of the GNRs used to measure the distance between the rods in staggered (red line) and eclipsed arrangement (green line); b, c) HR-TEM image of the GNRs at 0 °tilt and at 30 °tilt of the grid, respectively. Scale bars in all three images: 20 nm. On carrying out this operation, the top right corner seems to be unaffected. Red circle: staggered arrangement to eclipsed, green circle: vice versa; d) The cartoon, related to the TEM image in (a), illustrates the different projections of the GNR arrays as observed by TEM. TEM tilting experiments as shown in images (b, c) were used to establish the average side-by-side distance between the GNRs of 4.5 ± 0.5 nm.

It is noteworthy to mention here that the TEM of the well-washed sample showed only short-range side-by-side assembled structures (see appendix A, Figure A4). These patterns exhibit merely a local order with no in-plane correlation and isotropic behavior over a large extended area. Li and coworkers recently reported similar short-range side-by-side assemblies for perylene thiol-capped GNRs, where π-π stacking was assumed as a packing force. [39] One possible reason for this behavior could be that the density of the LC ligands on the pure functionalized rods (referred to here as “well washed”) is not suffi-

ciently high to induce an orienting influence on the rods over large extended areas. On the other hand, once-washed samples with a miniscule amount of the free **LC2** ligand present, exhibit highly ordered patterns as shown above. The unbound LC molecules in the composite are highly compatible with the ligands on the GNR surface (because they are structurally identical). Hence, the two components form a homogenous colloidal mixture. The free, unbound LC molecules fill the available space, act as mediators, and provide the necessary interactions, required stability as well as directional orientation to the composite thereby assisting the formation of highly ordered arrays of nanorods. More images supporting the remarkable self-assembly of these GNRs are provided in the Supporting Information (Figure A5–A11).

To ascertain that the GNR nanostructured assemblies form indeed over larger areas and not just in smaller sections on TEM grids we also performed SAXS experiments on both samples, the GNRs with end-on (terminal, **LC1**) as well as side-on (lateral) affixed nematogens (**LC2**). As shown in Figure 2.6, the azimuthally averaged intensity data derived from the 2D scattering pattern show only one broad peak corresponding to distances between the **LC1**-capped GNRs from 8.8 nm (side-by-side distance) to 17.7 nm (overlapping longitudinal distance) and for the **LC2**-capped GNRs from 10.2 nm (side-by-side) to 21.5 nm (overlapping longitudinal). These periodicity values are in perfect agreement with the distances measured in the various TEM images and the calculated molecular dimensions of the nematic molecules (with silane conjugation) on the surface of the two GNRs (side-by side for **LC2** and interdigitated for **LC1** as show in the insets of Figure 2.6a, d). The 2D SAXS patterns also match perfectly with the Fourier transforms (FFT) of the TEM images as shown in Figures 2.6c, f (shown in the same scale as

the 2D SAXS pattern). The different types of GNR arrays detectable in the TEM images, such as different extents of GNR overlap, some more smectic-type arrays, or the few, random isolated rods, most likely cause the lack of two distinct broad scattering maxima in the SAXS pattern one would expect for an unaligned nematic phase with GNRs constituents.

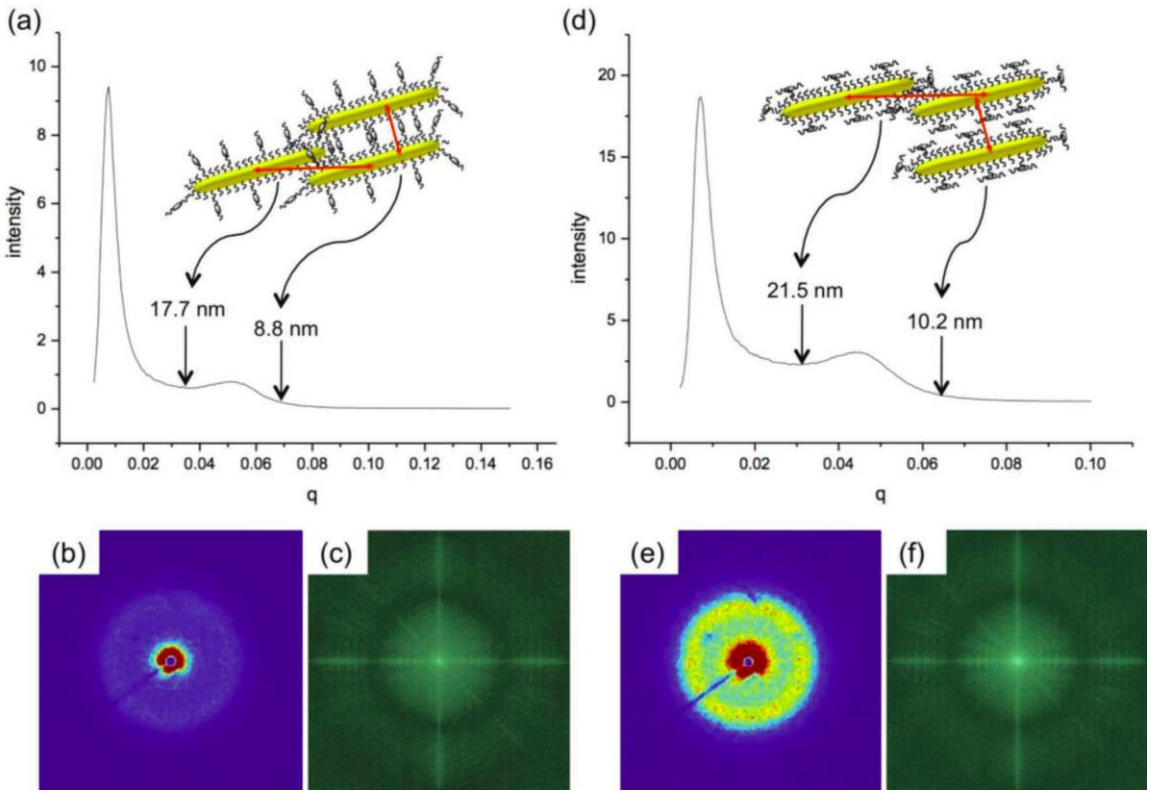

Figure 2.6. LC1-capped GNRs: a) azimuthally averaged intensity data of the scattering vector (q in $Å^{-1}$) vs. intensity from 2D SAXS pattern shown in (b); c) Example of a Fourier transform (FFT) obtained from TEM images such as the one shown in Figure 1a. LC2-capped GNRs: d) azimuthally averaged intensity data of the scattering vector (q in $Å^{-1}$) vs. intensity from 2D SAXS pattern shown in (e); f) example of a Fourier transform (FFT) obtained from TEM images such as the ones shown in Figure 3–5 and Supporting Information Figures S5–S11. Insets in (a) and (d) show cartoons demonstrating typical GNR distances found in the arrays imaged by TEM. Hence, the lateral spacing measured by SAXS (≈ 10.2 nm) confirms the average side-by-side spacing of 4.5 ± 0.5 nm obtained from TEM images (vide supra) considering the width of the GNRs (6.5 ± 1.5 nm). SAXS samples on Kapton windows were prepared similar to TEM samples on Cu grids. The peak at low q is from scattering around the high flux beam stop.

Polarized optical microscopy studies also showed that despite the rather low fraction of free, non-bound nematic LC molecules (only 5 wt% free vs. 95 wt% bound to the GNR surface) in the investigated 'once-washed' GNR composite, birefringent textures are observed between crossed polarizers as shown in Figure 2.7a, b. These textures are non-specific and extremely viscous (to some extent resembling nematic and smectic *Schlieren* textures of high molecular weight or polymeric organic LCs on first heating from an amorphous solid). However, even the well-washed GNR sample with no free, non-bound LC shows birefringence when viewed between crossed polarizers. For the image shown in Figure 2.7c, the polarizers were slightly uncrossed because of the very high optical density (absorbance) of the sample.

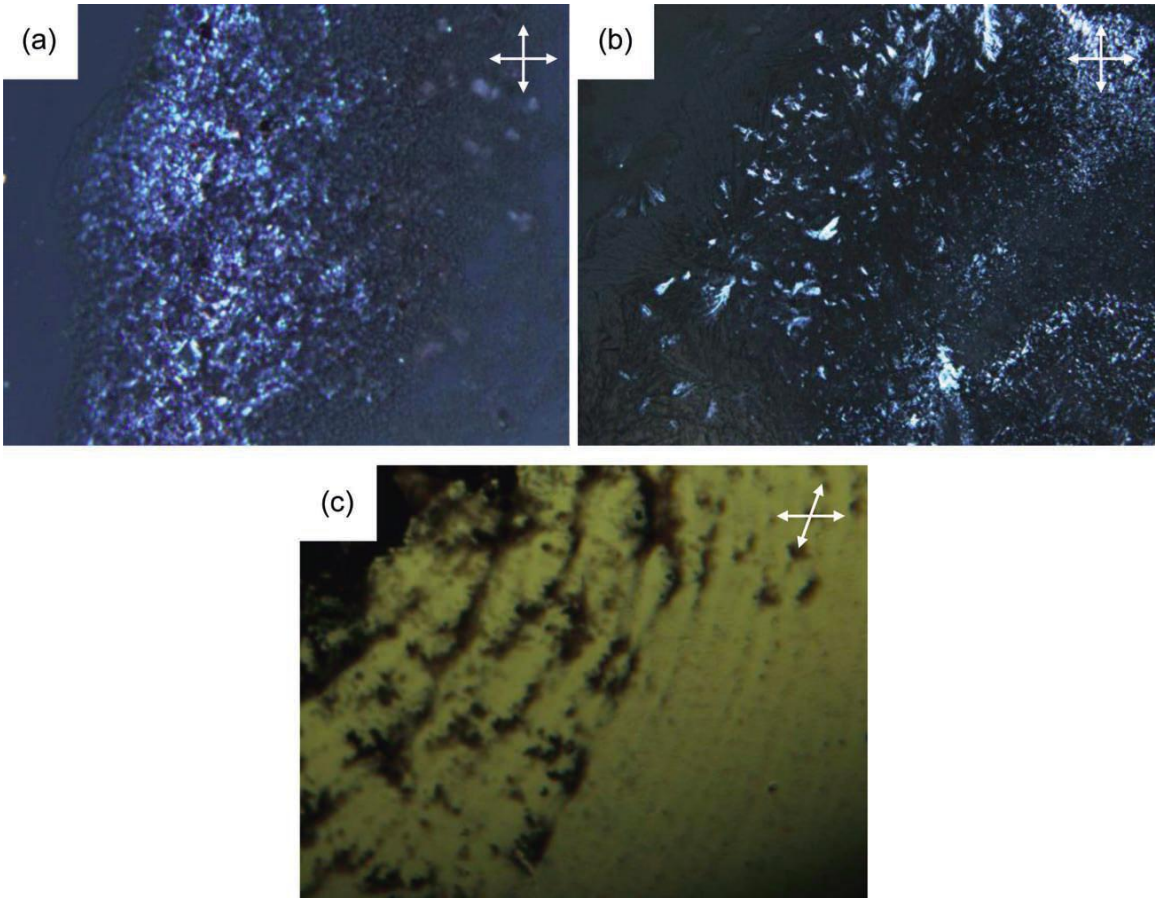

Figure 2.7. Polarized optical photomicroscopy images of: a,b) the once-washed GNRs on cooling at 75 ℃ between crossed polarizers (white arrows) and c) the well-washed GNRs on cooling at 80 ℃ between slightly uncrossed (15 °) polarizers.

Considering the various methods to assemble GNRs, most are restricted to aqueous medium, produce more confined arrays, and are largely based on electrostatic interactions between the dynamic surfactant molecules on the GNR surface and added external additives. [10–15] In contrast, our approach of covalently functionalizing the nanorods with a suitable liquid crystal molecule (in the presence of a small amount of free LC) offers more dynamically organized patterns, which could potentially be further manipulated by external stimuli through LC-mediated reorganizations. Recently we have reported the magnetic field induced orientation of nematic LC end-capped GNRs as discussed earlier

(Figure 2.1a). [31] In the present case, application of a weak magnetic field from a handheld rare earth magnet resulted in the reorientation of the GNR arrays in several areas of the TEM grid as shown in Figure 2.8a–c. This reorientation of the GNRs, achieved at temperatures were the pure **LC2** forms a nematic phase, is here the result of the magnetic field-induced Fr éedericksz transition of the **LC2** ligands linked to the GNR surface via silane conjugation assisted by the small quantity of free, non-bound **LC2** molecules in the colloidal mixture (only 1% by weight of the total mixture correspond to non-bound LC molecules). If both, the quantity of free LC molecules is enhanced (by adding an additional quantity of a room temperature nematic mixture; here E7), i.e., promoting attractive interactions between the rods as well as diluting the sample to encourage monolayer formation on the grid, and the magnetic field strength increased to 1.3 T using an electromagnet, reorientation of **LC1** -capped GNRs into hexagonal-ordered arrays extending several hundred nm 2 can be achieved (Figure 2.8d).

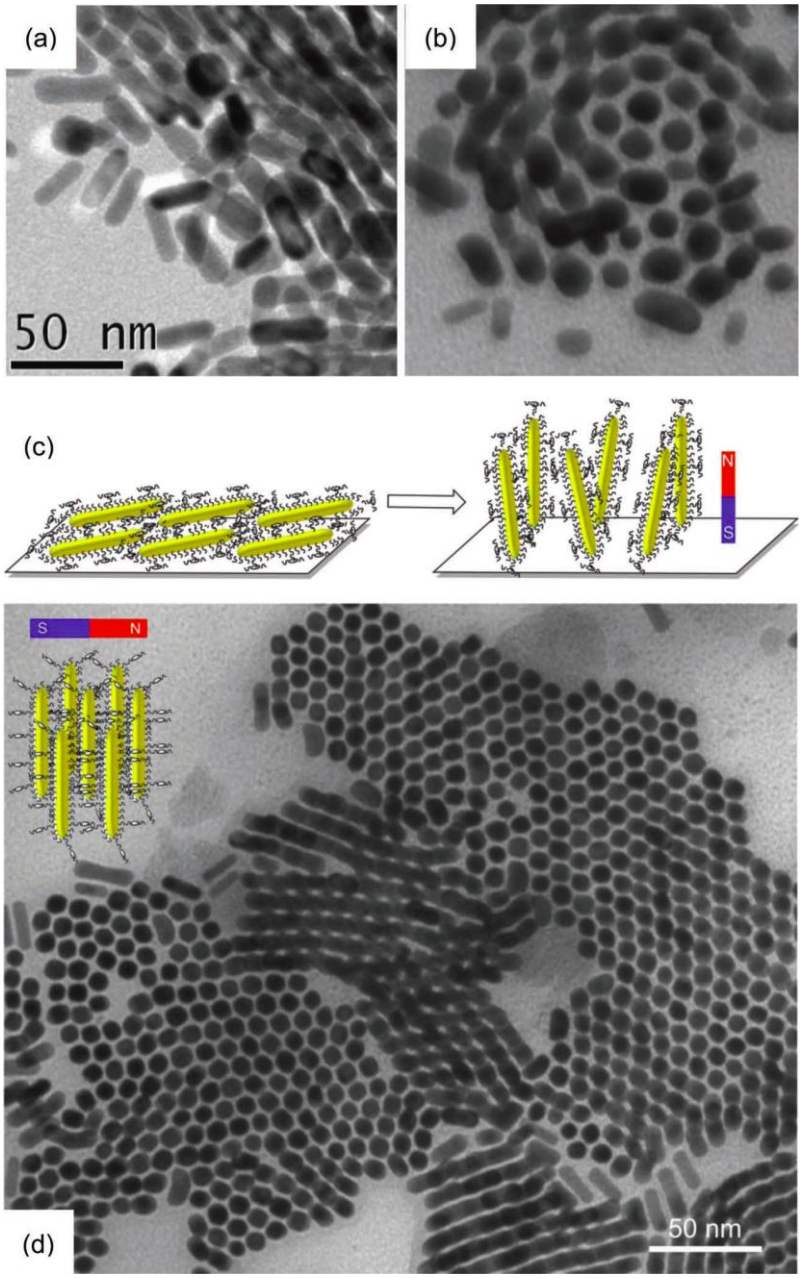

Figure 2.8. a, b) HR-TEM images of LC2 -capped GNRs: a) prior to applying a magnetic field and b) after applying a magnetic field (using 1 cm in diameter rare earth disc magnets) at elevated temperature (within the nematic phase range of LC2). Scale bar in (a) is valid for both images. The index grid was removed from the TEM instrument and inserted again after the magnetic field was applied. Care was taken to image almost the same area of the indexed grid. c) Schematic presentation of the magnetic field induced reorientation of the LC2-capped GNRs. d) Magnetic field induced assembly and alignment of LC1-functionalized GNRs in a 1:1 (by weight) mixture with E7 (using a LakeShore elec-

tromagnet at 1.3 T). Hexagonal close-packed assemblies can be seen extending hundreds of nm^2.

Overall, these initial experiments with the above-described lateral LC-capped GNRs provide intriguing starting points for further exploration regarding the manipulation of the GNR arrays using thermal annealing methods and/or applied magnetic fields. The described observations clearly highlight both feasibility and versatility of LC-guided self-assembly of GNRs with a unique advantage over other methods provided by the on-demand reorientation of arrays using external stimuli. A related example of such GNR reorientation in electric fields was recently disclosed by Richardson and co-workers for short range ordered hexagonally packed GNR suspended in a nematic liquid crystal (5CB). [40] The key difference in the present work is that the GNRs assemble into nematic and to some degree smectic-type arrays with only a miniscule amount of free liquid crystal molecules (about 1% by weight). Hence, the free liquid crystal acts here as the dopant (or suspended entity promoting attractive interactions between GNRs) in contrast to GNR suspensions investigated by others. Remarkably then, the obtained nematic-type arrays can be magnetically reoriented similar to purely organic nematic liquid crystals. Additional experiments also indicate that it is also possible to extend the self-assembly behavior of nematic LC-capped GNRs to discotic LC-capped GNRs by covalently functionalizing GNRs with suitable discotic LC moieties forming columnar phases in a similar fashion as described here. [41]

2.3 Conclusion

In summary, we described an exceptionally effective and versatile method for the self-assembly of GNRs provided by the functionalization with a laterally linked nematogenic LC ligand. These LC-capped GNRs display a rich variety of reproducible self-assembly leading to large-scale ordered superstructures with a variety of morphologies comparable to nematic to smectic LC morphologies on slow evaporation of the solvent on TEM grids. We report for the first time that GNR superstructures once formed can be reorientated simply by placing the sample in a magnetic field. The birefringence observed for these GNRs in thin film between crossed polarizers additionally supports the formation of self-assembled ordered LC-like anisotropic superstructures. Such systems have great significance as future metamaterials, SERS substrates, nanorod-based high efficiency polarizers, and other prominent applications in biological and technological fields.

2.4 Experimental Section

Synthesis: Compound **1** (0.4 g, 0.5 mmol) was dissolved in dry toluene (10 mL) and trimethoxysilane (0.31 mL, 2.5 mmol) added under nitrogen atmosphere and stirred for 30 min. To this solution, 1,1,3,3-tetramethyldisiloxane Pt-complex (Karstedt's catalyst, 0.1 M) in xylene (50 μ L, 0.01 eq.) was added and stirring continued for further 18 h maintaining the nitrogen atmosphere. The solvent and excess trimethoxysilane was removed under vacuum resulting in a light brown residue. Attempts to purify the silane from this residue using column chromatography (both silica and alumina) were unsuccessful, and the mixture contained mainly silane **LC2** and some isomerized **1** (28% as

calculated from NMR) with a migrated double bond (vinyl → allyl). Cr 67 (N 86) Iso (monotropic nematic phase observed by POM); ^{1}H NMR (300 MHz, $CDCl_3$, δ ppm): 8.19 (d, 2H, Ar-H), 8.06 (d, 1H, Ar-H), 7.66-7.59 (m, 4H, Ar-H), 7.32-7.25 (m, 4H, Ar-H), 6.98 (d, 2H, Ar-H), 6.58-6.51 (m, 2H, Ar-H), 5.42 (m, 0.62H, -CH=CH-), 4.11-4.01 (m, 6H, -O-CH_2), 3.6 (s, 9H, -Si-$(OCH_3)_3$), 1.92-1.80 (m, -*CH_2*-CH=CH), 1.41-1.60 (m, 6H, -O-CH_2-*CH_2*), 1.22 -1.40 (m, 36H, -CH_2-), 1.0-0.82 (m, 9H, -CH_3), 0.68-0.61 (m, 1.44H, -CH_2-Si-$(OCH_3)_3$); IR (KBr): ν_{max} = 2922, 2853, 1739, 1722, 1606, 1569, 1510, 1493, 1467, 1433, 1393, 1254, 1204, 1164, 1135, 1075, 1038, 872, 849, 792, 759, 719, 689, 653 and 507 cm^{-1}.

The percentage of silane in the mixture was estimated using characteristic peaks in the ^{1}H NMR of the residue, i.e. by comparing the ratio of the integration of the methyl peak at 0.65 ppm [(-CH_2-Si-$(OCH_3)_3$) due to compound **LC2**] to the alkene proton peak at 5.42 ppm [(-CH=CH-) due to the migrated double bond in compound **1**], which provided a yield of 72% for the reaction described above. Based on the estimated percentage yield of silane from the NMR, the residue was dissolved in chloroform to make a 10 mM solution, where only the silane will react in the subsequent condensation step.

The coating exchange of CTAB on the GNR surface with nematic ligands was carried out as described below. A measured volume (3 mL) of CTAB-capped GNRs was washed once with an equal volume of chloroform in order to remove the excess free ligand. The washed rods were treated with an appropriate volume (120 μL) of MPS (10 mM solution in ethanol) and vortexed for 2–3 min. The resulting colloidal solution was allowed to stand at room temperature for 30 min. Thereafter, the nematic silane solution (3 mL, 10 mM in chloroform) was added, followed by a base (30 μL, 1 M NaOH), and vortexed

again for 2–3 min. Very soon, the change in the color of the solvent clearly indicated the coating exchange of CTAB GNRs with nematic LC and their subsequent phase transfer from the water to the organic chloroform phase. Upon exchange, the water phase becomes clear and the chloroform phase becomes dark brown in color as shown in Figure S1 (Supporting Information). The organic phase was separated and stirred at room temperature overnight to ensure the completeness of the capping process. The resulting solution was ultra-centrifuged (16 000 rpm, 20 min) to remove the excess free ligand. The nanorod precipitate was redispersed in toluene and centrifuged again. The process of precipitation and redispersion were repeated several times until the last supernatant was free from any residual non-bound silane/ siloxane as confirmed by ^{1}H NMR. This excess ligand-free sample was used for UV-Vis-NIR and FTIR measurements shown in Figure 2. However, our investigations demonstrated that the once centrifuged sample with a small amount of free LC ligand (≈ 150 μL of 10 mM free LC in a 1 mL GNR dispersion, 5 wt% free vs. 95 wt% bound to the GNR surface) present produces exceptional self-assembled superstructures of GNRs compared to the well-washed sample (no free LC).

Acknowledgements

The authors would like to thank the Province of Manitoba for a grant from the Science and Technology International Collaboration Fund, the Natural Science and Engineering Research Council (NSERC) of Canada, the Canada Foundation for Innovation (CFI), and the Manitoba Research and Innovation Fund (MRIF) for financial support. T.H. also

acknowledges financial support from Kent State University and the Government of Ohio's Third Frontier Program for Ohio Research Scholars. Special thanks go to Dr. Kevin McEleney for his help with the SAXS measurements and to Andre Dufresne for all the help and assistance with TEM imaging.

References

[1] S. Link, M. A. El-Sayed, *Annu. Rev. Phys. Chem*. **2003**, *54*, 331.

[2] M. E. Stewart, C. R. Anderton, L. B. Thompson, J. Maria, S. K. Gray, J. A. Rogers, R. G. Nuzzo, *Chem. Soc. Rev*. **2008**, *108*, 494.

[3] P. K. Jain, X. H. Huang, I. H. El-Sayed, M. A. El-Sayed, *Acc. Chem. Res*. **2008**, *41*, 1578.

[4] M. R. Jones, K. D. Osberg, R. J. Macfarlane, M. R. Langille, C. A. Mirkin, *Chem. Rev*. **2011**, *111*, 3736.

[5] L. Xu, H. Kuang, L. Wang, C. Xu, *J. Mater. Chem*, **2011**, *21*, 16759.

[6] K. Liu, N. Zhao, E. Kumacheva, *Chem. Soc. Rev.* **2011**, *40*, 656.

[7] P. R. Sajanlal, T. S. Sreeprasad, A. K. Samal, T. Pradeep, *Nanoreviews* **2011**, *2*, 5883.

[8] (a) X. Huang, I. H. El-Sayed, W. Qian, M. A. El-Sayed, J. *Am. Chem. Soc.* **2006**, *128*, 2115; (b) D. Pissuwan, S. M. Valenzuela, C. M. Miller, M. B. Cortie, *Nano Lett.* **2007**, *7*, 3808; (c) H. Ding, K. T. Yong, I. Roy, H. E. Padavar, W. C. Law, E. J. Bergey, P. N. Prasad, *J. Phys. Chem. C.* **2007**, *111*, 12552.

[9] (a) L. R. Hirsch, R. J. Stafford, J. A. Bankson, S. R. Sershen, B. Rivera, R. E. Price, J. D. Hazle, N. J. Halas, J. L. West, *Proc. Natl. Acad. Sci.* **2003**, *100*, 13549; (b) L.

Tong, Y. Zhao, T. B. Huff, M. N. Hansen, A. Wei, J. X. Chen, *Adv. Mater.* **2007**, *19*, 3136; (c) R. S. Norman, J. W. Stone, A. Cole, C. J. Murphy, T. L. Sabo-Attwood, *Nano Lett*. **2008**, *8*, 302; (d) W. Zhang, J. Meng, Y. Ji, X. Li, H. Kong, X. Wu, H. Xu, *Nanoscale* **2011**, *3*, 3923; (e) K. Y Lin, A. F. Bagley, A. Y. Zhang, D. L. Karl, S. S. Yoon, S. N. Bhatia, *Nano Life* **2010**, *1*, 277.

[10] (a) N. R. Jana, T. Pal, *Adv. Mater*. **2007**, *19*, 1761; (b) K. D. Alexander, K. Skinner, S. P. Zhang, H. Wei, R. Lopez, *Nano Lett*. **2010**, *10*, 4488; (c) L. Zhong, X. Zhou, S. Bao, Y. Shi, Y. Wang, S. Hong, Y. Huang, X. Wang, Z. Xie, Q. Zhang, *J. Mater. Chem*. **2011**, *21*, 14448.

[11] B. Nikoobakht, Z. L. Wang, M. A. El-Sayed *J. Phys. Chem. B* **2000**, *104*, 8635.

[12] F. Kim, S. Kwan, J. Akana, P. Yang, *J. Am. Chem. Soc.* **2001**, *123*, 4360.

[13] T. Sau, C. J. Murphy *Langmuir* **2005**, *21*, 2923.

[14] (a) T. S. Sreeprasad, A. K. Samal, T. Pradeep, *Langmuir* **2008**, *24*, 4589; (b) T. S. Sreeprasad, T. Pradeep, *Langmuir* **2011**, *27*, 3381.

[15] K. Mitamura, T. Imae, N. Saito, O. Takai *J. Phys. Chem. B* **2007**, *111*, 8891.

[16] (a) E. Dujardin, L. Hsin, C. R. Chris Wang, S. Mann, *Chem. Commun.* **2001**, 1264; (b) B. Pan, D. Cui, C. Ozkan, P. Xu, T. Huang, Q. Li, H. Chen, F. Liu, F. Gao, R. He, *J. Phys. Chem. C* **2007**, *111*, 12572.

[17] C. Hamon, M. Postic, E. Mazari, T. Bizien, C. Dupuis, P. Even-Hernandez, A. Jimenez, L. Courbin, C. Gosse, F. Artzner, V. Marchi-Artzner, *ACS Nano* **2012**, *6*, 4137.

[18] N. Kanayama, O.Tsutsumi, A. Kanazawa, T. Ikeda, *Chem*. *Commun*. **2001**, 2640.

[19] I. In, Y. Jun, Y. J. Kim, S. Y. Kim, *Chem. Commun.* **2005**, 2640.

[20] L. Cseh, G. H. Mehl, *J. Am. Chem. Soc*. **2006**, *128*, 13376.

[21] V. A. Mallia, P. K. Vemula, G. John, A. Kumar, P. M. Ajayan, *Angew. Chem. Int. Ed*. **2007**, *46*, 3269.

[22] X. Zeng, F. Liu, A. G. Fowler, G. Ungar, L. Cseh, G. H. Mehl, J. E. Macdonald, *Adv. Mater.* **2009,** *21*, 1746.

[23] H. Qi, B. Kinkead, V. M. Marx, H. R. Zhang, T. Hegmann, *ChemPhysChem* **2009**, *10*, 1211.

[24] M. Wojcik, W. Lewandowski, J. Matraszek, J. Mieczkowski, J. Borysiuk, D. Pociecha, E. Gorecka, *Angew. Chem. Int. Ed.* **2009**, *48*, 5167.

[25] M. Draper, I. M. Saez, S. J. Cowling, P. Gai, B. Heinrich, B. Donnio, D. Guillon, J. W. Goodby, *Adv. Funct. Mater*. **2011**, *21*, 1260.

[26] M. Yamada, Z. Shen, M. Miyake, *Chem. Commun*. **2006**, 2569.

[27] S. Kumar, S. K. Pal, P. S. Kumar, V. Lakshminarayanan, *Soft Matter* **2007**, *3*, 896.

[28] V. M. Marx, H. Girgis, P. A. Heiney, T. Hegmann, *J. Mater. Chem.* **2008**, *18*, 2983.

[29] H. Park, A. Agarwal, N. A. Kotov, O. D. Lavrentovich, *Langmuir* **2008**, *24*, 13833.

[30] Q. Liu, Y. Cui, D. Gardner, X. Li, S. He, I. I. Smalyukh, *Nano Lett*. **2010**, *10*, 1347.

[31] S. Umadevi, X. Feng, T. Hegmann, *Ferroelectrics* **2012**, *431*, 164.

[32] S. Diez, D. A. Dunmur, M. R. De la Fuente, P. K. Karahaliou, G. H. Mehl, T. Meyer, M. A. P. Jubindo, D. J. Photinos, *Liq. Cryst.* **2003**, *30*, 1021.

[33] D. Apreutesei, G. H. Mehl, *Chem. Commun*. **2006**, 609.

[34] N. R. Jana, *Small* **2005**, *1*, 875.

[35] (a) S. Link, M. A. El-Sayed, *J. Phys. Chem. B* **1999**, *103*, 8410; (b) Y. Yu, S. Chang, C. Lee, C. R. C. Wang, *J. Phys. Chem. B* **1997**, *101*, 6661; (c) S. Link, M. B.

Mohamed, M. A. El-Sayed, *J. Phys. Chem. B* **1999**, *103*, 3073; (d) M. M. Miller, A. A. Lazarides, *J. Phys. Chem. B* **2005**, *109*, 21556; (e) H. Wang, D. W. Brandl, F. Le, P. Nordlander, N. J. Halas, *Nano Lett*. **2006**, *6*, 827; (f) T. K. Sau, A. L. Rogach, F. Jäckel, T. A. Klar, J. Feldmann, *Adv. Mater*. **2010**, *22*, 1805.

[36] For examples, see: (a) J. J. Mock, D. R. Smith, S. Schultz, *Nano Lett*. **2003**, *3*, 485; (b) C. Yu, L. Varghese, J. Irudayaraj, *Langmuir* **2007**, *23*, 9114; (c) A. Wijaya, K. Hamad-Schifferli, *Langmuir* **2008**, *24*, 9966; (d) Z. R. Guo, C. R. Gu, X. Fan, Z. P. Bian, H. F. Wu, D. Yang, N. Gu, J. N. Zhang, Nanoscale Res. Lett. **2009**, *4*, 1428.

[37] (a) H. Jiang, Z. Zheng, Z. Li, X. Wang, *Ind. Eng. Chem. Res.* **2006**, *45*, 8617; (b) H. K. Park, T. H. Ha, K. Kim, *Langmuir* **2004**, *20*, 4851; (c) D. Blaudez, M. Bonnier, B. Desbat, F. Rondelez, *Langmuir* **2002**, *18*, 9158.

[38] E. Rabani, D. R. Reichman, P. L. Geissier, L. E. Brus, *Nature* **2003**, *426*, 271.

[39] C. Xue, Q. Birel, M. Gao, S. Zhang, L. Dai, A. Urbas, Q. Li, *J. Phys. Chem. C* **2012**, *116*, 10396.

[40] M. R. Thomas, S. Klein, R. J. Greasty, S. Mann, A. W. Perriman, R. M. Richardson, *Adv. Mater.* **2012**, *24*, 4424.

[41] X. Feng, L. Sosa-Vargas, S. Umadevi, T. Mori, Y. Shimizu, and T. Hegmann, *Adv. Funct. Mater.* **2015**, *25*, 1180-1192.

Appendix A

Supplementary Information for Chapter 2

Measurements, Methods, and other general Information:

Chemicals and solvents were purchased from Aldrich and either used as received or purified by standard methods. E7 was obtained from Merck. ^{1}H NMR (Bruker Avance 300 MHz spectrometer) spectra were recorded using deuterated chloroform ($CDCl_3$) or deuterated dimethylsulfoxide-d_6 (DMSO-d_6) as solvents. Tetramethylsilane (TMS) was used as an internal standard. Thermal behavior and textural observations of the LC samples were carried out using an Olympus BX51-P polarized light microscope (POM) equipped with a Linkam LS-350 heating/cooling stage. UV-Vis-NIR absorption spectra (Varian Cary 5000 UV-vis-NIR spectrophotometer) were recorded using a quartz cell (1 cm path). IR (Bruker Tensor 27 spectrometer) spectra were recorded as KBr discs using the chloroform solutions of the samples. TEM (Hitachi H 7000 transmission electron microscope) images were recorded by drop casting 2-3 μL of the GNR dispersion on carbon-coated copper grids (400 mesh) after drying for one hour under ambient conditions. HR-TEM images were recorded on a Jeol ultrahigh resolution FEG-T/STEM operating at an accelerating voltage of 200 kV. The GNR reorientation studies were performed either using 1 cm in diameter rare earth disc magnets or a LakeShore EM4 electromagnet at 1.3 T. SAXS data were collected using a Rigaku 3-pinhole camera (S-MAX3000) equipped

with a Rigaku MicroMax+002 microfocus sealed tube (Cu K_α radiation at 1.54 Å) and Confocal Max-Flux (CMF) optics operating at 40 W. The system has a 3-m, fully evacuated camera length. The system was also equipped with 200 mm multiwire 2D detector for data collection. We collected SAXS data at $0.008 \leqslant q \leqslant 0.4$ $Å^{-1}$ with 600 s of exposure. The data reduction was performed using Rigaku's SAXGUI data processing software.

Additional Supporting Data, Images, and Figures:

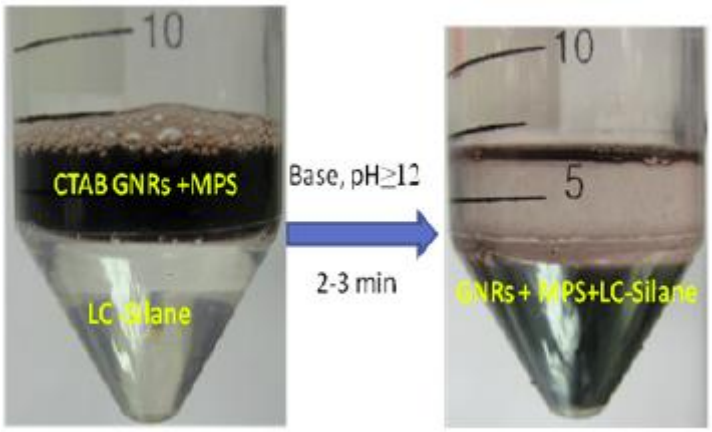

Figure A1. Pictorial representation of the phase transfer of CTAB GNRs from the aqueous phase to the organic phase upon coating exchange with the nematic LC silane, top layer: water, bottom layer: chloroform.

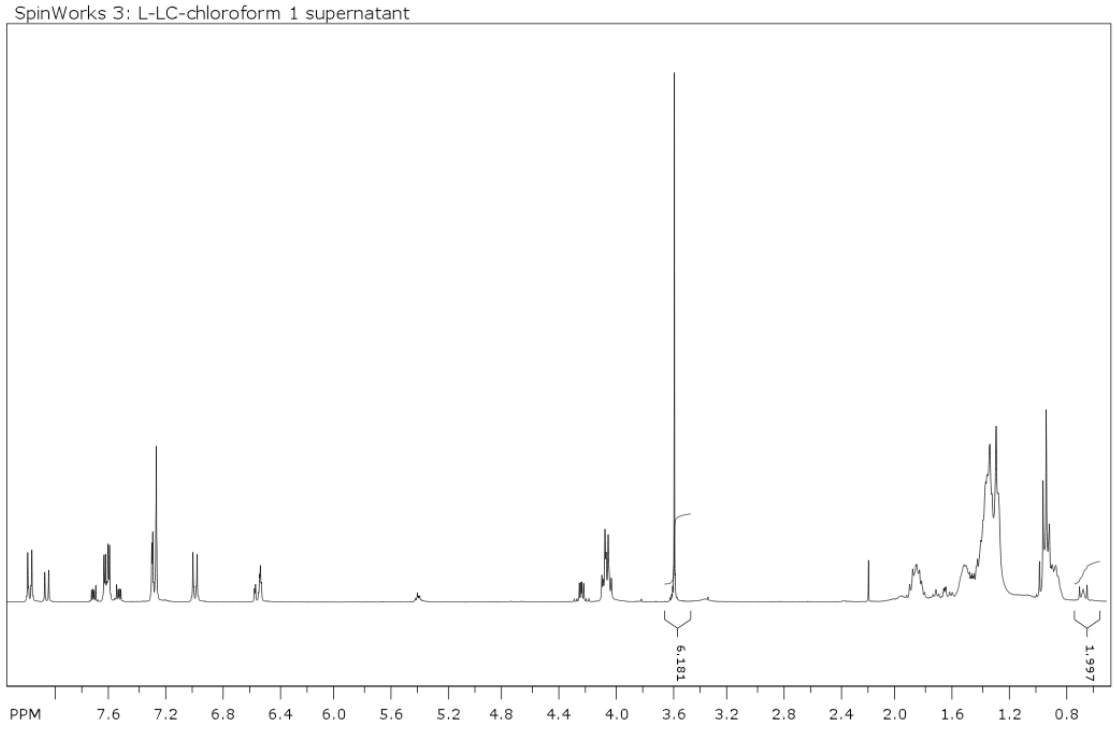

Figure A2. ^{1}H NMR spectrum of the supernatant obtained on precipitation of the rods right after the coating exchange with the LC2-silane.

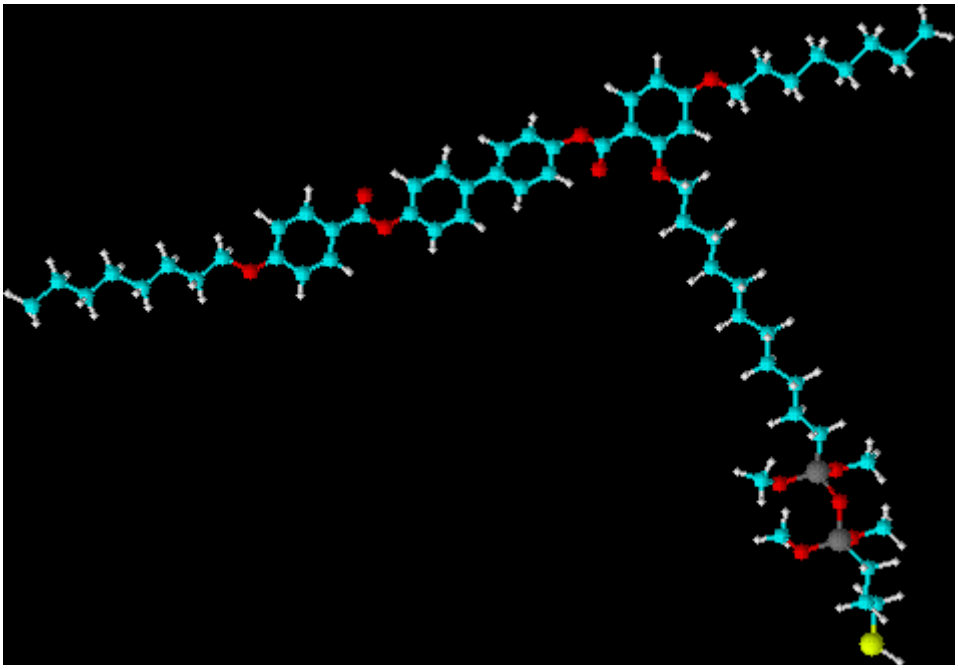

Figure A3. 3D structure of LC2-silane conjugated to MPS supporting the side-by-side self-assembly of the GNRs.

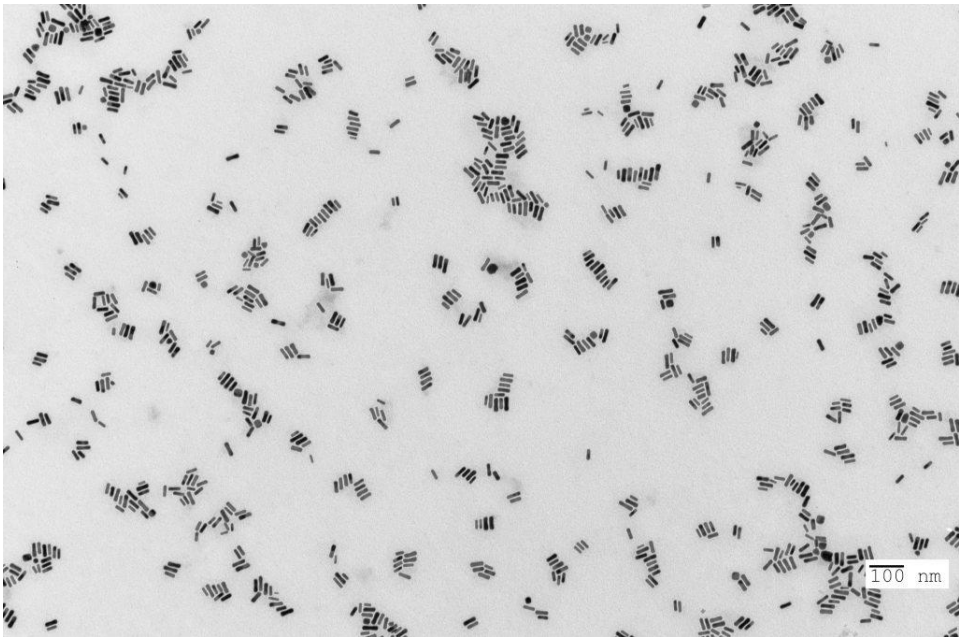

Figure A4. TEM image obtained for the well-washed sample in toluene.

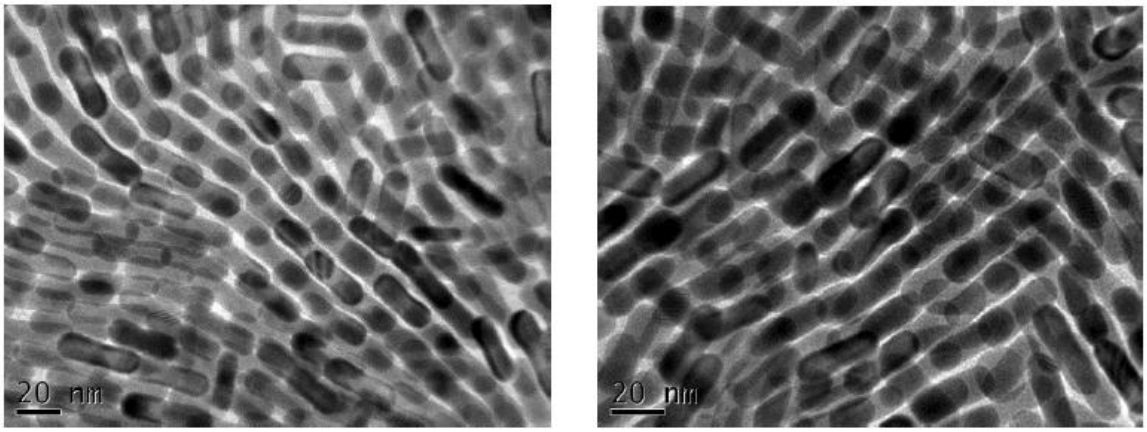

Figure A5. HR-TEM images showing the staggered (left) and eclipsed (right) stacking patterns formed by the LC2-capped GNRs.

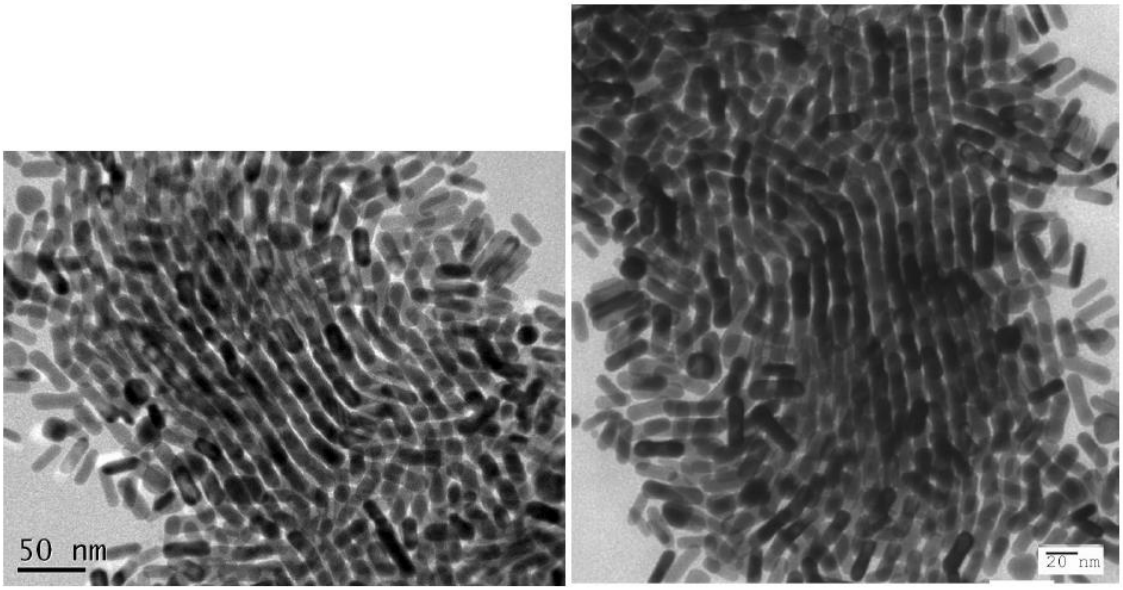

Figure A6. Self-assembled domains of LC2-coated GNRs at two different regions of the grid.

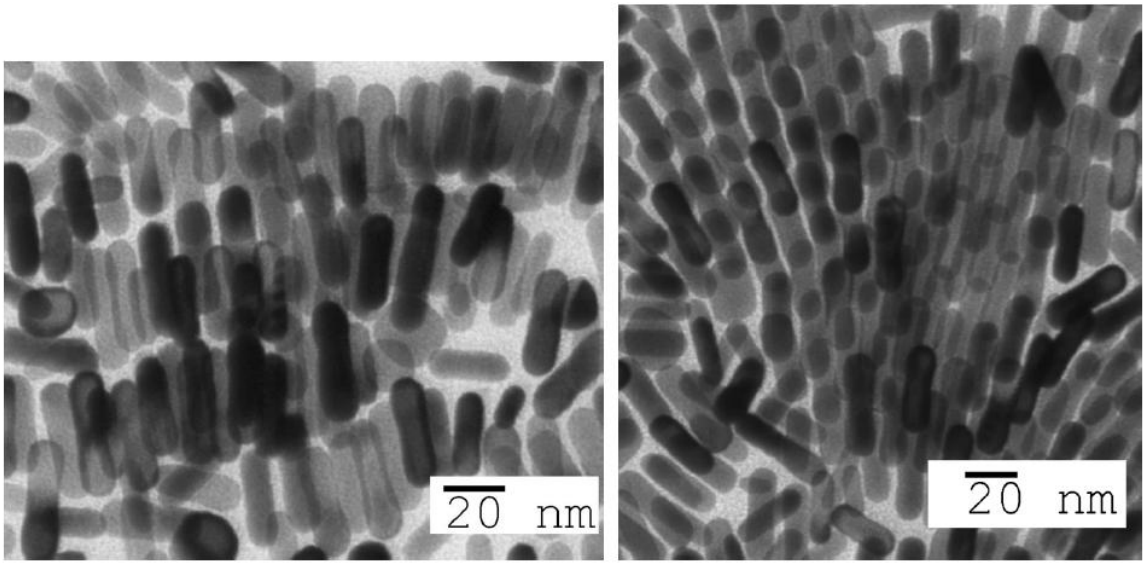

Figure A7. TEM images of the fascinating self-assembled GNRs of LC2-functionalized GNRs.

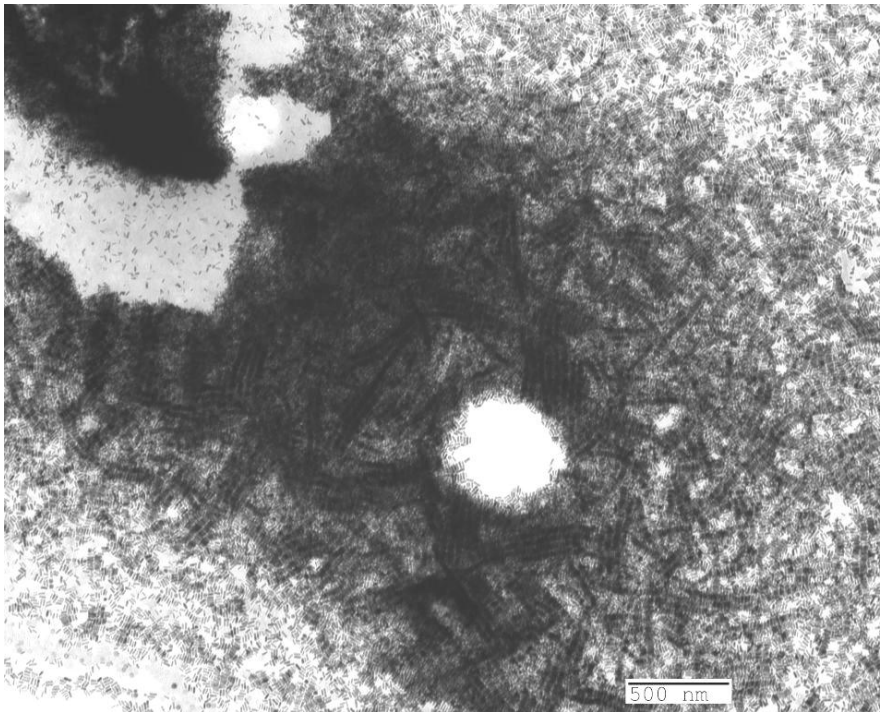

Figure A8. TEM image showing the extended smectic-type arrays of the LC2-functionalized GNRs.

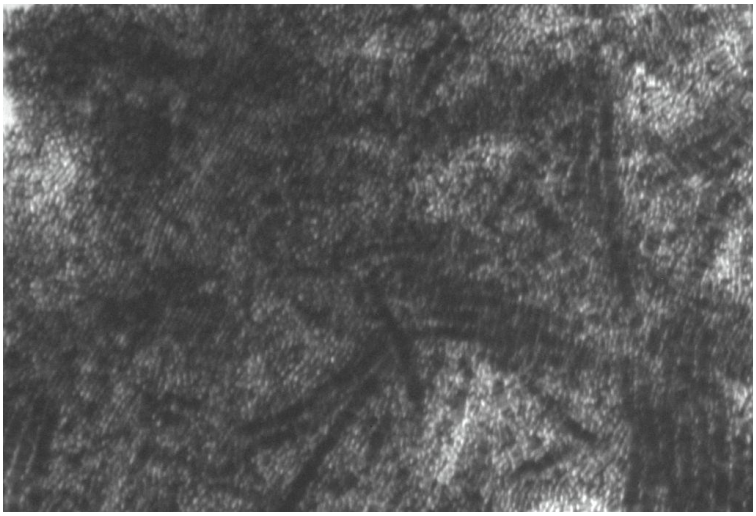

Figure A9. Expanded view of the rectangular selected area of the image shown in Figure A8.

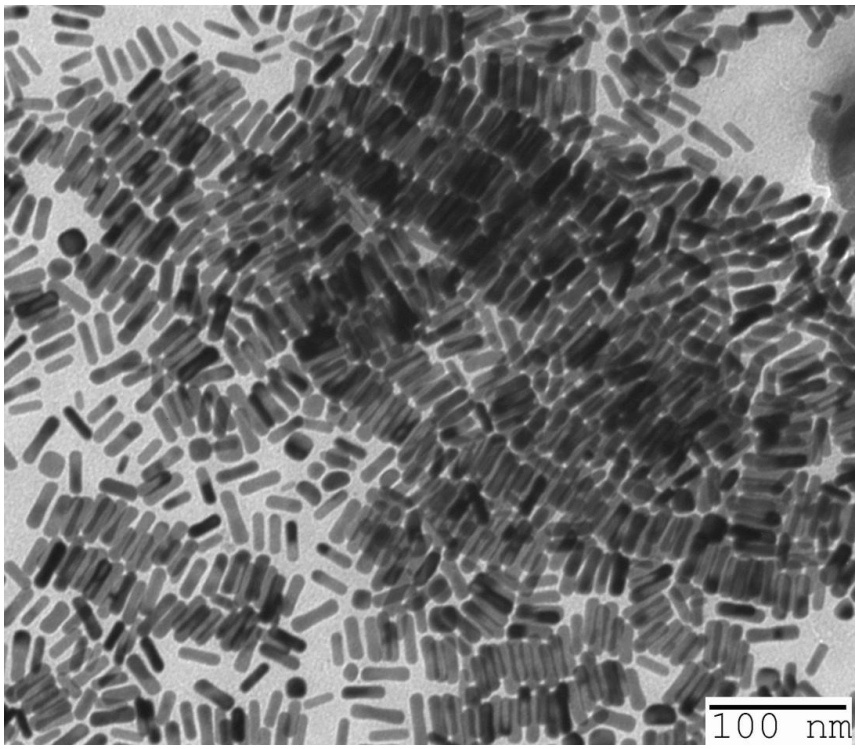

Figure A10. Area showing 3D smectic-like arrays of LC2-functionalized GNRs.

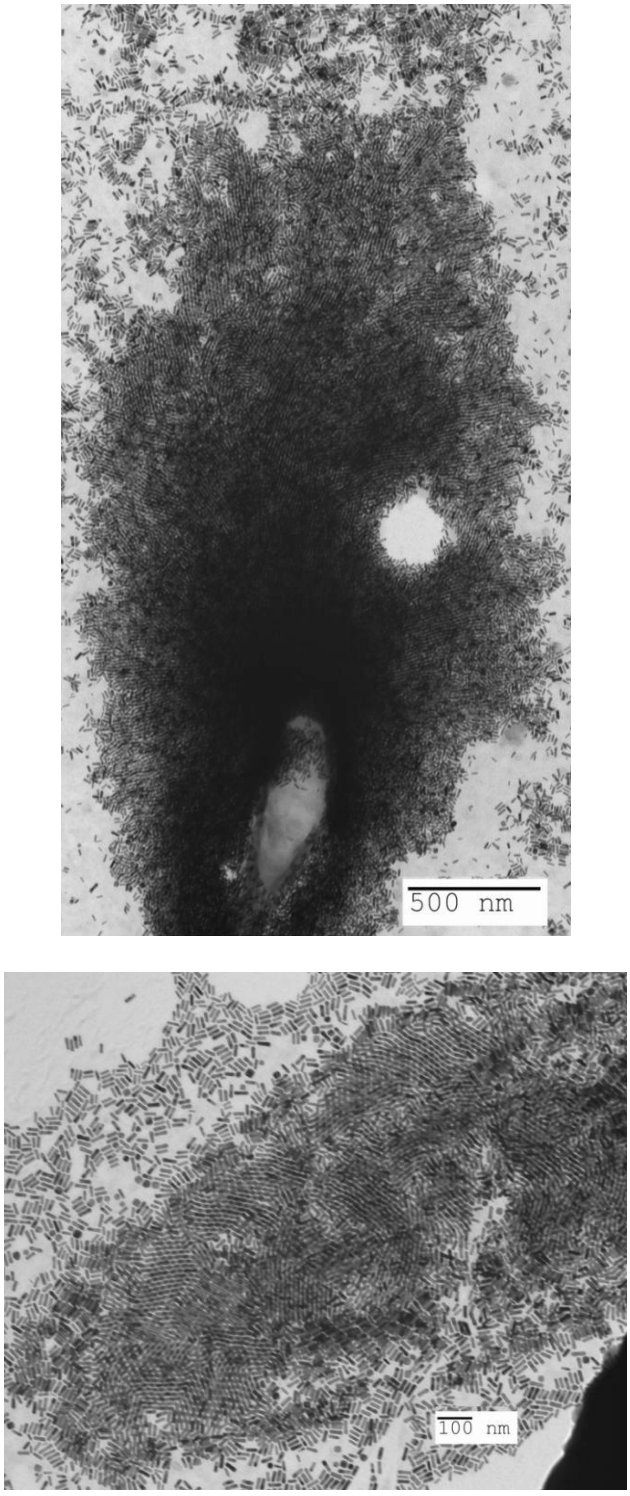

Figure A11. Examples of the large area (several μm^2) assembly of LC2-functionalized GNRs.

Chapter 3

Discotic liquid crystal functionalized gold nanorods: 2- and 3D self-assembly and macroscopic alignment as well as increased charge carrier mobility in hexagonal columnar liquid crystal hosts affected by molecular packing and π-π interactions

Discotic liquid crystal functionalized gold nanorods: 2- and 3D self-assembly and macroscopic alignment as well as increased charge carrier mobility in hexagonal columnar liquid crystal hosts affected by molecular packing and π-π interactions

Xiang Feng,[a] Lydia Sosa-Vargas,[b] Umadevi Shivakumar,[a]# Taizo Mori,[c] Yo Shimizu,[b] and Torsten Hegmann[a, c, d]*

[a] Department of Chemistry, University of Manitoba, Winnipeg (MB) R3T 2N2 (Canada)

[b] Nanotechnology Research Institute, National Institute of Advanced Industrial Science and Technology (AIST), Ikeda, Osaka (Japan)

[c] Liquid Crystal Institute and Chemical Physics Interdisciplinary Program, Kent State University, Kent (OH) 44242 (USA) Fax: (+1) 330-672-2796 Email: thegmann@kent.edu

[d] Department of Chemistry & Biochemistry, Kent State University, Kent (OH) 44242-0001 (USA)

Current address: Department of Industrial Chemistry, Alagappa University, Karaikudi-630 006 (India)

* Author for correspondence

Reproduced with the permission from *Adv. Funct. Mater.* **2015**, *25*, 1180-1192.

 DOI: 10.1002/adfm.201401844

Authors' Contributions

The idea of functionalization of GNRs with discotic LCs and the insertion into parent DLCs was conceptualized by Dr. Torsten Hegmann. Xiang Feng conducted the work of the synthesis of CTAB-GNRs and DLC silane, the functionalization process, measurements by TEM, DSC and UV-Vis-NIR, preparation of DLC-GNRs & DLC mixtures for the polarized UV-Vis-NIR alignment tests, SAXS analysis and TOF conductivity measurement. Dr. Lydia Sosa-Vargas conducted the TOF analysis of the DLC mixtures. Dr. Taizo Mori helped with the construction of the figures for the explanations regarding the insertion of DLC-GNRs in DLCs. Dr. Yo Shimizu helped with the discussion of the enhanced conductivity of the mixtures compared with the neat DLCs. Xiang Feng wrote the original manuscript. XF and TH were responsible for the final revision of the manuscript before publication.

Abstract

Gold nanorods functionalized with triphenylene-based discotic liquid crystal motifs show striking self-assembly behavior both on TEM grids as well as in the bulk enforced by the π-π-stacking of triphenylene groups of adjacent nanorods. TEM images confirm that these discotic liquid crystal nanorods form ribbons of parallel-stacked nanorods several hundred nanometer long. The pursued silane conjugation approach to decorate the nanorods allows for the preparation of dispersions of the nanorods in the hexagonal columnar phases of parent discotic liquid crystals, where the nanorods can be macroscopically aligned with almost 80% efficiency by a simple shearing protocol. Doping the parent host materials with about 1% by weight of the discotic liquid crystal-capped nanorods also reduces the lattice parameter and the intra-columnar packing giving rise to enhanced charge carrier mobility in these hosts as determined by time-of-flight measurements.

3.1 Introduction

Approaches of manipulating anisotropic nanoparticles, in order to arrange the particles into ordered assemblies[1], generated significant interest over the past few years for the creation of metamaterials[2], for optical applications such as high efficiency polarizers[3] and display applications[4], as well as for applications in surface-enhanced Raman spectroscopy[5]. However, the assembly and manipulation of anisotropic building blocks into complex superstructures is still a challenging task in comparison to their corresponding quasi-spherical counterpart nanoparticles[6]. The key-limiting factor most often described is the irreversible aggregation of the anisometric nanomaterial in a given fluid or polymer host medium. It is well understood that the interactions between nanostructures plays a critical role during the self-assembly process[7]. Ionic additives[8] or cationic surfactants[9] have been employed to tune the attraction between nanoparticles in colloidal suspensions and improve the ability of inducing nanorods assemblies.

In an earlier paper, we reported a fascinating large area self-assembly of nematic liquid crystal (LC) functionalized gold nanorods (GNRs) forming nematic and smectic like patterns on substrates, and nematic phase behavior in the bulk[10]. The interaction between the liquid crystal molecules attached to the surface of the GNRs was established as the driving force for the self-assembly of such GNRs. The attached liquid crystal ligands tended to pack together next to each other when the GNRs dispersion became more and more concentrated during solvent evaporation, and attractive interactions between the capping LC ligands facilitated the formation of large area nematic and smectic super-

structures of the GNRs. To extent this concept to higher ordered LC phases that would facilitate long-range order, alignment, and even enhanced photoconductivity, we here present the synthesis, characterization, as well as the surface and bulk self-assembly of GNRs functionalized with discotic triphenylene-based LC (DLC) molecules (Figure 1a). Strong π-π interactions between the triphenylene cores should aid the self-assembly as well as integration and alignment in structurally identical triphenylene hosts. Yamada *et al.*[11] reported a 2D hexagonal superstructure of such DLC-functionalized gold nanoparticles on the substrate of TEM grids after solvent evaporation. The authors concluded that the packing status of the functional LC ligands in the dispersion influenced the self-assembled of the nanoparticles on TEM grids. Kumar and co-workers presented data on such DLC nanocomposites,[12] which show that DLC-functionalized gold nanoparticles[12a] and unmodified carbon nanotubes[12b] enhance the electrical conductivity of the DLC hosts to a very high level compared with the pure DLC. The authors also suggested that the inclusion of shape-anisotropic nanotubes into the DLC matrix leads to not only to a homogeneous dispersion of the nanotubes in the DLC superlattice, and predicted that alignment of one-dimensional nanostructures can be achieved by employing well-established LC alignment technologies.

Herein, we describe for the first time GNRs functionalized with DLC molecules via a silane conjugation approach,[13] the self-assembly in the bulk and on TEM grids as well as their alignment in the superlattices of the parent DLC host in planar alignment cells and the effect of the GNR inclusions on the charge carrier mobility of the DLC host.

3.2 Experimental Section

3.2.1 General Methods

All chemicals were obtained from commercial sources ($HAuCl_4$ ∃H2O, $AgNO_3$, ascorbic acid, $NaBH_4$, CTAB, B-bromocatecholborane, Karstedt's catalyst, octadecyltrimethoxysilane are all purchased from Sigma-Aldrich) and used without further purification. High-purity deionized (DI) water (Millipore, 18 MΩ) and Aldrich purification grade solvents purified *via* a PureSolv solvent purification system (Innovative Technology, Inc.) were used for the synthesis and purification of the presented materials. All glassware used for synthesis and sample handling was cleaned with *aqua regia* and thoroughly rinsed with DI water. The liquid crystal H4TP was available in our laboratory.

UV-Vis-NIR absorption spectra were recorded using an Agilent Cary 5000 UV-Vis-NIR spectrophotometer using a quartz cell (1 cm path length). TEM images were recorded on a Hitachi H7000 microscope. The samples were prepared by drop casting a 5 μL dispersion of the GNR solution onto carbon-coated copper grids (400 meshes) and dried overnight under ambient conditions. Polarized optical photomicrographs were taken using an Olympus BX51-P polarizing optical microscope equipped with a Linkam LS 350 heating/cooling stage. SAXS data were collected using a Rigaku 3-pinhole camera (S-MAX 3000) equipped with a Rigaku MicroMax+002 microfocus sealed tube (Cu Kα radiation at λ = 1.54 Å) and Confocal Max-Flux (CMF) optics operating at 40 W. The system has a 3-m, fully evacuated camera length, and is equipped with 200 mm multi-wire 2D detector for data collection as well as an option to use image plates at various distanc-

es away from the sample. The data reduction was performed using Rigaku's SAXGUI data processing software.

Mechanical shearing was used to obtain planar alignment of the H6TP/GNRs composite in the Col_{ho} phase (85 ℃). The polarized UV-Vis-NIR spectrophotometry was carried at the same temperature using the same Linkam heating stage in the beam path of the spectrophotometer.

The analysis of the charge transport properties of the H4TP doped with 1 wt% and 2 wt% of GNR were carried out by time-of-flight experiments, which is a technique commonly used for estimating mobilities of charge carriers (hole and electron) in a semiconductor or a low-conductivity material (see figure B7). Shorter flying times of hole and electron indicate higher charge carrier mobilities. The samples were injected by capillary action of the isotropic phase into a sandwich-type ITO coated cells (cell gap: 2-3 μm as measured by interferometry). The measurements were carried out on slow cooling from the isotropic to the crystalline phase. Carrier transport was measured using the conventional set-up and a N_2 laser (λ = 337 nm) as excitation source, whilst recording the photocurrents with an oscilloscope. Temperature variation was obtained with a hot-stage and temperature controller.

3.2.2 Synthesis

The synthesis of triphenylene based discotic liquid crystals H6TP (compound **1**) followed the process of intermolecular oxidative aromatic coupling reaction [34] from 1,2-dihexyloxybenzene using $FeCl_3$ as oxidant. The trimerization reaction probably proceeds through a radical mechanism (see figure B8). The alkoxyl substituents can stabilize a rad-

ical intermediate. The mono-functionalized triphenylene derivatives for the conjugation to the GNRs was synthesized according to a previously published procedure,[14] and the hydrosilylation reaction was following the same conditions described in our earlier work.[10] The synthesis of the monoalkene-functionalized hexaalkoxytriphenylene (Scheme 1) was performed as follows[14-15]: A solution of H6TP, **1**, (0.67 g, 0.5 mmol) in anhydrous CH_2Cl_2 (10 mL) was cooled to 0 ℃ before 1.2 eq. (0.12 g, 0.6 mmol) B-bromocatecholborane (dissolved in 1 mL CH_2Cl_2) was added dropwise. The mixture was kept stirring at room temperature for 72 h. Thereafter it was poured on ice water (50 ml) and the water layer was extracted with CH_2Cl_2 (2 times 20 mL). The organic layer was separated by column chromatography (hexanes/ethyl acetate = 30/1). The purified monohydroxy triphenylene compound **2** (0.18 g, 0.24 mmol) was dissolved in 10 ml THF, and KOH (0.0132 g, 0.24 mmol) was added under stirring. The reaction was refluxed for 1 h before 11-bromo-1-undecene (0.174 mL, 0.8 mmol) was injected. The system was kept under reflux for 24 h, and was then poured into 20 mL 1M HCl, and extracted with CH_2Cl_2 (twice 20 mL). The monoalkene compound **3** (Cr 30.5 Col 57.5 Iso) was purified by recrystallization from *n*-hexane. Compound **3** (0.09 g, 0.1 mmol) was then dissolved in 2 mL of dry toluene, and under stirring 64 μL of trimethoxysilane (0.5 mmol) and 20 μL of Karstedt's catalyst (0.1M in xylene) was added subsequently. The reaction was stirred at room temperature for 24 h. The monosilane compound **4** was purified by filtration through a 0.45 μm PTFE syringe micro-filter before silane conjugation to the MPS-coated GNRs. Further details can be found in the Appendix B.

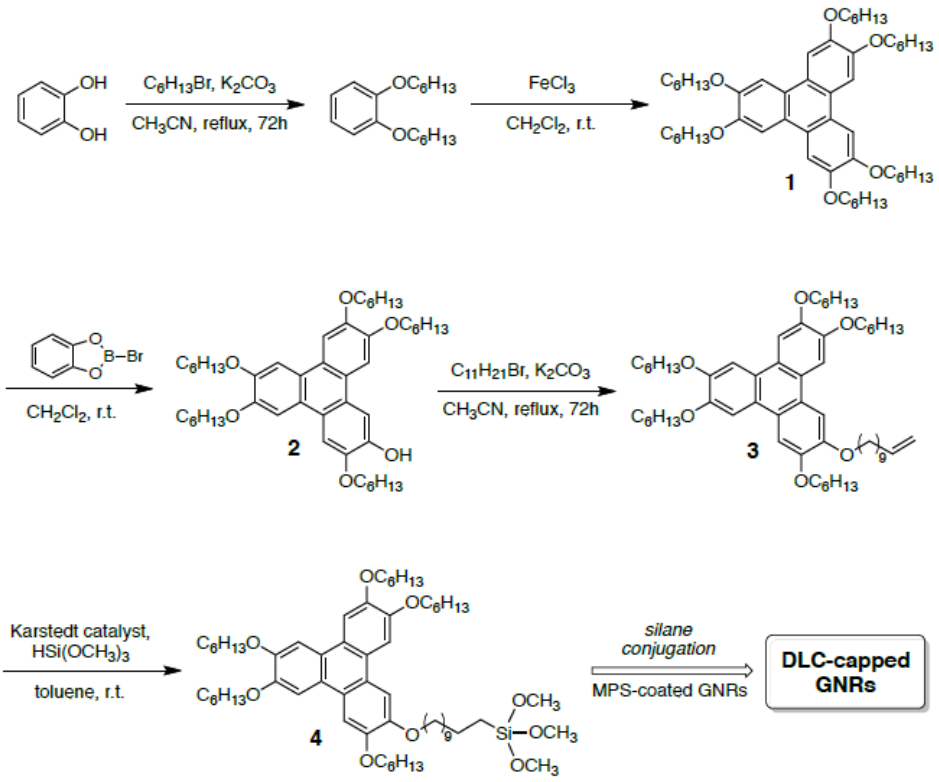

Scheme 3.1. Synthesis route to triphenylene LC-decorated GNRs following a silane-conjugation approach.

Next, the GNRs were synthesized following the modified single-step growth method using cetyltrimethylammonium bromide (CTAB) as initial capping agent, as described in the references[10, 16]. (1) Synthesis of CTAB-GNRs: the CTAB-capped GNRs were synthesized employing a modified one-step method as reported before[10, 16]. A 250 mL water solution containing the following compounds was prepared: [$HAuCl_4 \cdot 3H_2O$] = 1.0 mM, [CTAB] = 0.20 M, [$AgNO_3$] = 0.20 mM, [ascorbic acid] = 2.0 mM. Then 1.87 mL of 0.1 mM ice-cold NaBH4 aqueous solution was added into the mixture under stirring. After 2 minutes, the mixture was kept for 24 h at 30 ° C allowing the growth of the GNRs. The resulting GNRs were washed by repeated agitation with 100 mL DI water and centrifugation at 16,000 rpm for 20 minutes.

The functionalization of the CTAB-GNRs was achieved by a two-step silane hydrolysis condensation step reported previously[10, 16-17]: 3 mL of as-synthesized CTAB-GNRs were washed with 3 mL $CHCl_3$, and then 120 μL of 3-mercaptopropyl-trimethoxysilane, MPS, (10 mM in ethanol, calculated to provide about 30 molecules/nm^2) was added into the CTAB-GNRs in water under vigorous stirring for 30 minutes. Thereafter, 3 mL of a $CHCl_3$ solution (10 mM) of the DLC silane **4** or octadecyltrimethoxysilane (ODS) was added, followed by 30 μL of base (1.0 M NaOH). The two-phase system was vortexed for several minutes until the water phase became colorless and the organic phase turned to red-brown, indicating the functionalization to LC-functionalized, hydrophobic GNRs. The organic layer was separated and the GNRs was isolated by centrifugation (12,000 rpm, 20 min) and washed with toluene.

3.3 Results and Discussion

Figure 3.1a shows the schematic representation of the as-synthesized **DLC-GNR**s and Figure 3.1b shows the UV-Vis-NIR absorbance spectrum of the DLC-GNRs in chloroform. The absorption bands at 520 nm and 820 nm belong to the transversal and longitudinal surface plasmon resonance absorbances of the DLC-GNRs, respectively, indicating that the aspect ratio of the GNRs is about 3 to 4 on average. [18] Moreover, the absorbance bands at 250 to 290 nm belong to the valence electron π-π* transition of the triphenylene core of the DLC molecules. The peak of this band shifted from 285 nm for the free DLC molecules (blue spectrum in Figure 1b) to 260 nm for the GNRs dispersion (red spectrum in Figure 3.1b). This blue-shift can be explained by the enhancement of the local field of

the surface area of the GNRs due to the surface plasmon effect, [19] and was used as an evidence for the DLC molecules attachment to the surface of the GNRs. The 2D simplified cartoon of the **DLC-GNR**s in Figure 3.1a also highlights that during the silane conjugation a small amount of CTAB surfactant is retained on the surface of the GNRs as established in previous work using x-ray photoelectron spectroscopy (XPS). [10, 16]

The self-assembly behavior of the neat **DLC-GNR**s on substrates was first investigated by drop-casting dispersions of the GNRs in toluene on carbon-coated transmission electron microscopy (TEM) copper grids after slow evaporation of the solvent. Figure 3.2 shows some representative TEM images of the **DLC-GNR** samples dried from GNRs dispersion in toluene (about 6 mg/mL). Instead of an even, yet random dispersion on the grid during the solvent evaporation, the DLC functionalized GNRs tend to gather together in a side-by-side fashion to form what is best described as ribbons of nanorods.

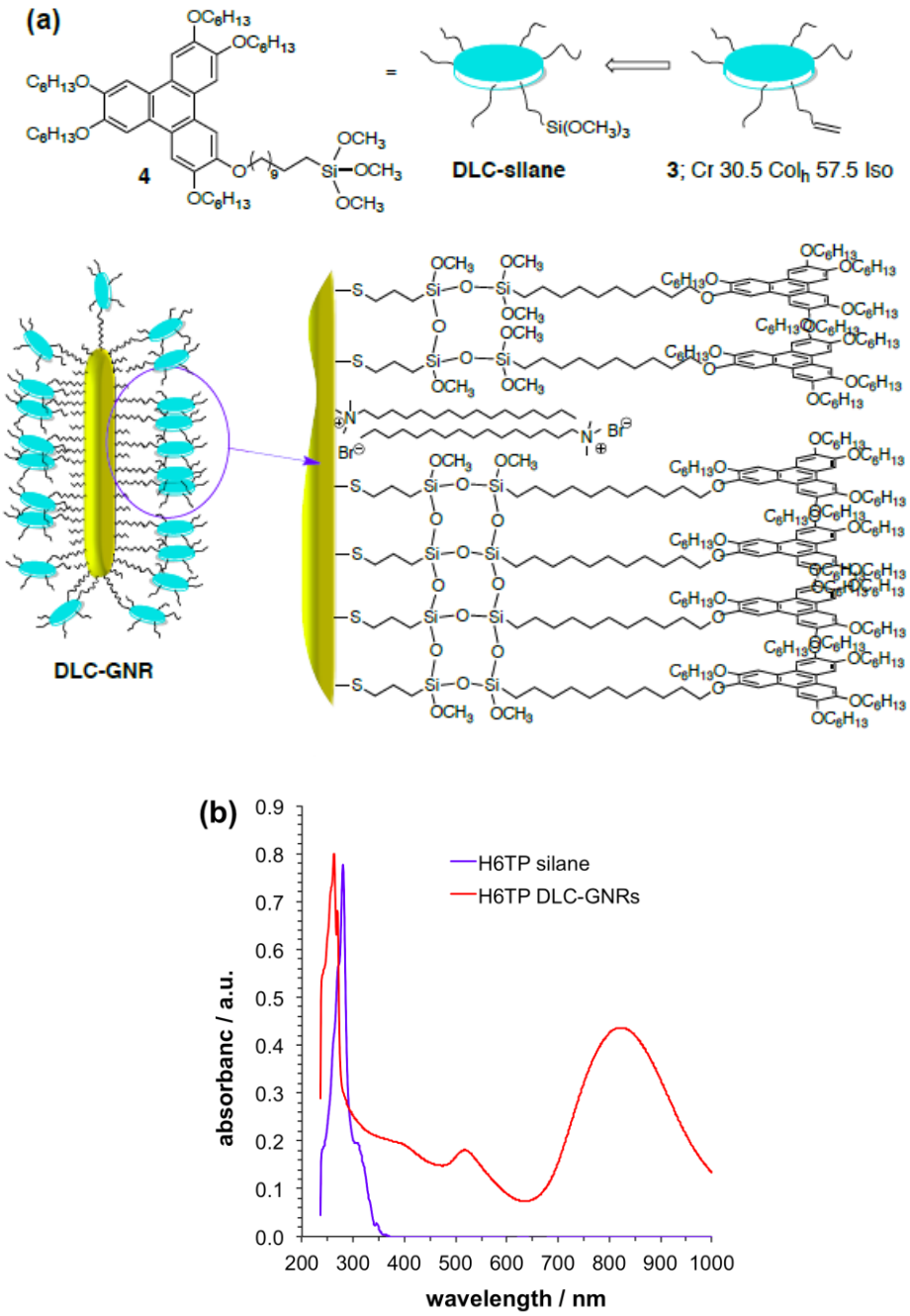

Figure 3.1. (a) Structure and phase transition temperatures of the DLC silane precursor 3 and silane 4 as well as a 2D schematic representation of the DLC-functionalized GNRs (DLC-GNR). (b) UV-vis-NIR spectra of the DLC silane 4 and the DLC-GNRs.

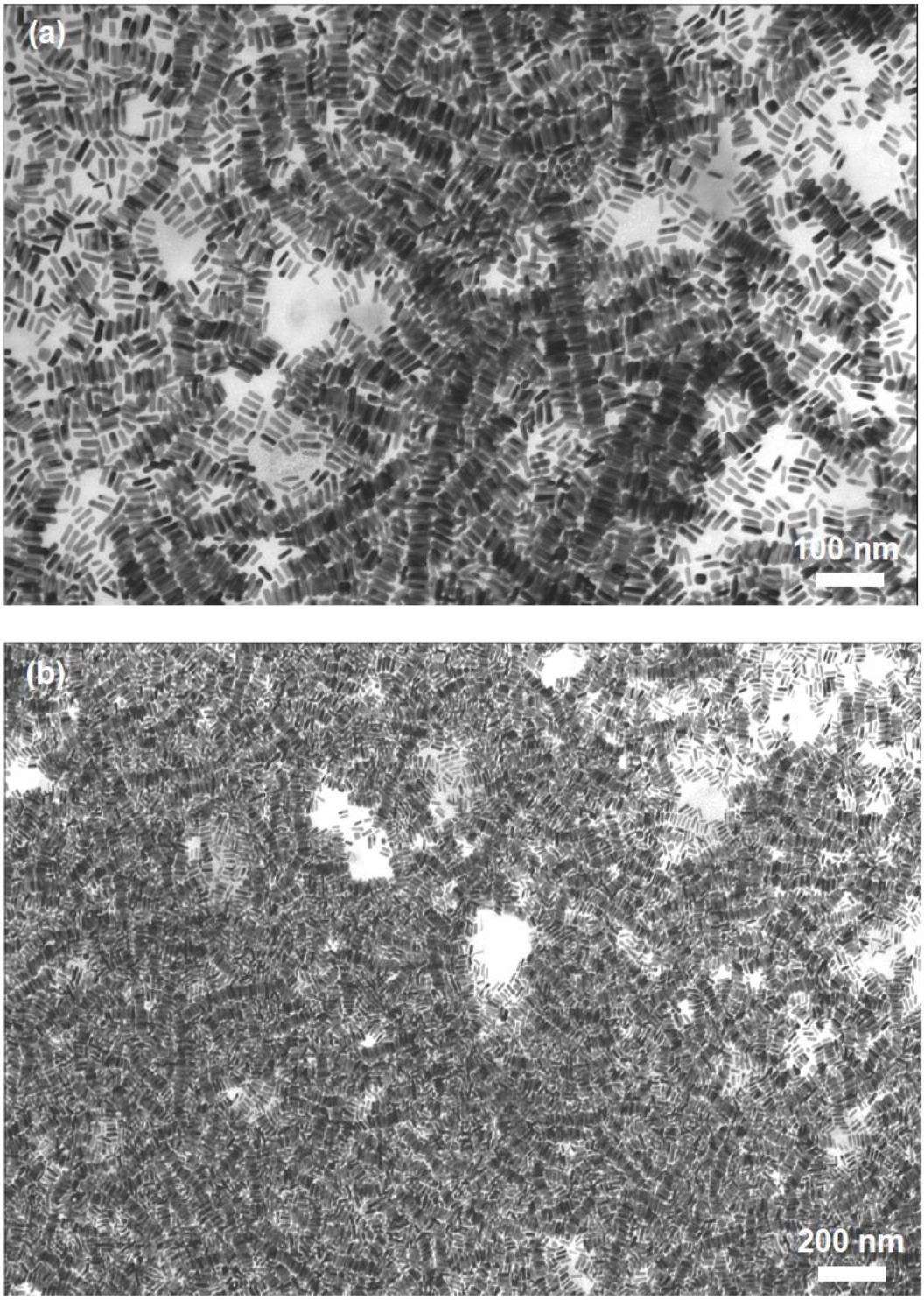

Figure 3.2. Transmission electron microscopy images of the DLC-GNRs dried on TEM grids from dispersion in toluene.

The self-assembly potential of the **DLC-GNR** supported by these images suggests that there are attractive interactions between the GNRs driving the side-by-side long-range assembly. In this case, the major driving forces are π-π interactions between the triphenylene moieties of the DLC molecules in addition to natural side-by-side assembly of anisometric rod-like entities. As sown in Figure 3.3, these assemblies exist over very large areas with several μm^2.

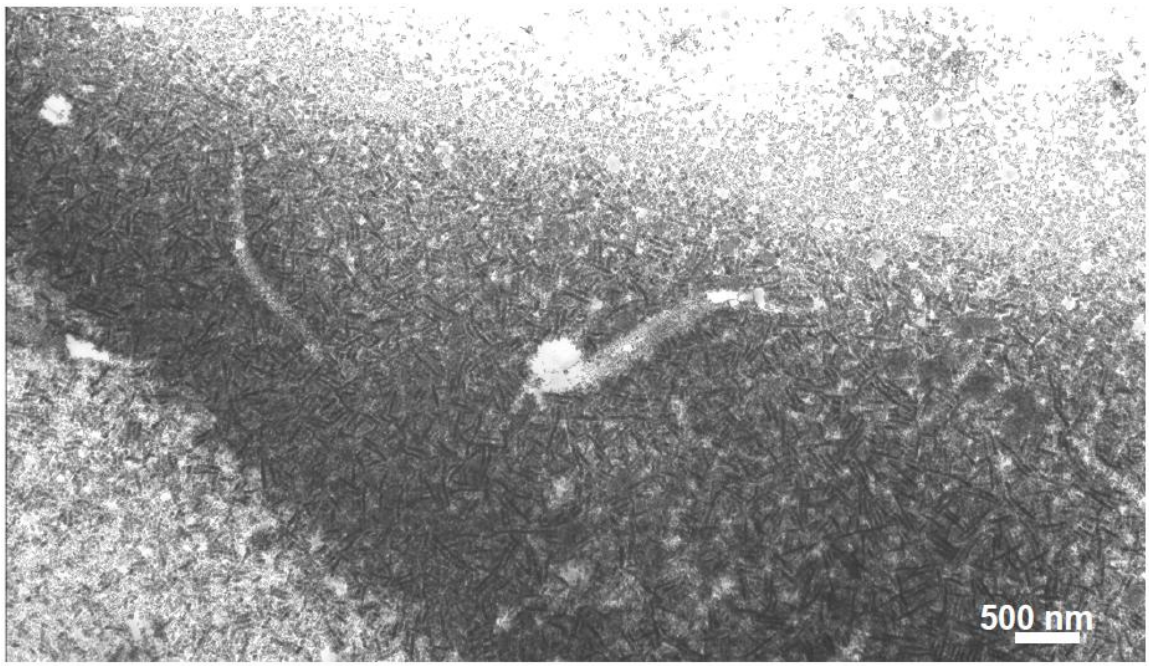

Figure 3.3. TEM image showing the large-area self-assembly of the DLC-GNRs. Several GNR ribbons extend over several hundred nanometers.

To obtain a monolayer of GNRs on the TEM grid that allows us to measure the distance between neighboring GNRs, we also tuned the concentration of the GNRs dispersion. The image in Figure 3.4a and the corresponding cross section profile (Figure 3.4b) shows that the gap between **DLC-GNR**s is about 7 nm on average (peak widths were measured as the full width at half-maximum), which matches perfectly with the length of the stacking molecules from neighboring GNRs with the triphenylene core overlapping

each other (see inset, Figure 3.4a). For comparison, octadecyltrimethoxysilane (ODS)-coated GNRs were also synthesized, and a representative TEM image of the **ODS-GNR**s drop-cast and dried from toluene is shown in Figure 3.4c. From the corresponding cross sectional profile (Figure 3.4d), the gap between the ODS-GNRs was measured to be 3-4 nm, which also matches with the molecular length of the alkyl chains of neighboring GNRs overlapping with one other. The difference is that, instead of the large area assembly of DLC-GNRs shown above, the ODS-GNRs are not showing only short-range self-assembly (see Appendix B, Figure B1). It is well known that the self-assembly of anisotropic colloidal nanostructures is to a large extent determined by the type and nature of the surface modification, in another words, a tailored interaction between the rod-like nanoparticles. The DLC molecules themselves owing to their intrinsic packing in columnar stacks forming a hexagonal columnar phase in a certain temperature interval due to strong π-π stacking drive here the self-assembly of the GNRs.

In order to further demonstrate the π-π stacking assembly model inside the multiple layers of the **DLC-GNR**s, a highly condensed dispersion of these GNRs was prepared and drop-casted on a Kapton® substrate and dried under ambient atmosphere before performing small-angle X-ray scattering (SAXS) experiments. Figure 3.5a shows the 2-dimensional scattering pattern from the X-ray detector. The plot of intensity vs. scattering vector q (Figure 3.5b) shows a broad peak at $q = 0.035$, corresponding to a d spacing of about 18 nm ($d = 2\pi/q$, in Å), which corresponds to the Fourier transform obtained from the TEM images (for example FFT in Figure 3.5b obtained from the TEM image shown in Figure 3.2b using Image J®). Considering the average diameter of the GNRs (11 ± 1 nm), the average gap between **DLC-GNR**s is approximately 7 nm, which agrees perfect-

ly with the number measured by analyzing TEM images, as well as the bimolecular length of the DLCs with overlapping triphenylene cores.

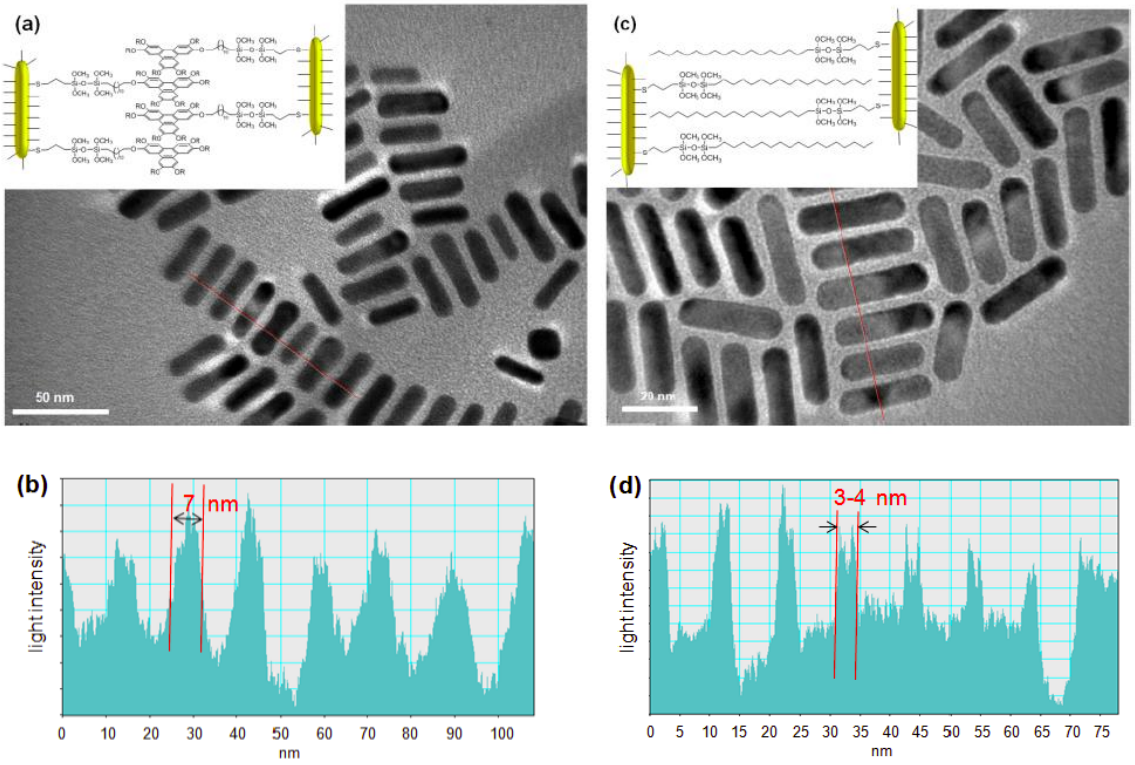

Figure 3.4. (a) TEM image of the DLC-GNRs, (b) cross section profile of (a), (c) TEM image of the ODS-GNRs, (d) cross section profile of (c). Insets show the arrangement of the GNRs in each case.

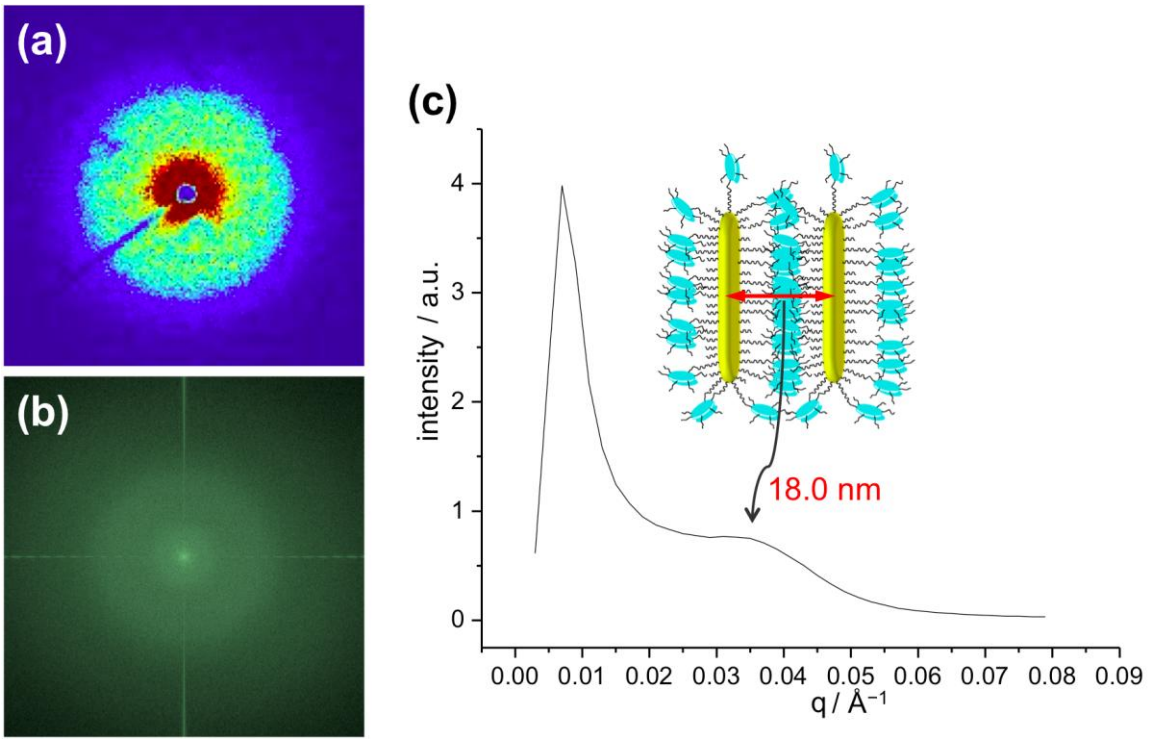

Figure 3.5. (a) 2D SAXS pattern, (b) Fourier transform of the TEM image shown in Figure 2b, and (c) azimuthally averaged intensity data of the scattering vector (q in $Å^{-1}$) from (a).

While the large area self-assembly of the DLC-GNRs on TEM grids is static, the essential π-π interactions should also facilitate alignment of the GNRs in a parent triphenylene host. To study this, we prepared mixtures of the **DLC-GNR**s in two triphenylen-based hexagonal columnar LC hosts, H6TP forming an Col_{ho} (ordered hexagonal columnar) and H4TP forming a Col_{hp} (hexagonal columnar plastic) phase, with the concentrations of the **DLC-GNR**s at 1 or 2 wt% (much higher than reported for many other nanorods in LCs[20]). This concentration will determine the numerical ratio between the H6TP (or H4TP) molecules and the DLC-GNRs. Assuming approximately 7×10^6 free H6TP molecules per GNR (at 1wt% and 10 mg H6TP) in a given mixture, the ratio between free H6TP molecules and anchored discotic mesogens on the GNR surface is about

1,160:1, considering there are approximately 6,000 DLC silane molecules attached to the surface of each **DLC-GNR** (with 10% CTAB) following calculations published by Gelbart *et al*.[21] The **DLC-GNR**s easily disperse in the parent DLC hosts (H6TP, **1**) without showing any discernable aggregation under the polarized light optical microscope (even at 100× magnification). The thermal property observed from differential scanning calorimetry (DSC) measurements (Figure B2 for H6TP) show that the liquid crystal phase transition temperatures are practically identical for the pure hosts and the 1 and 2 wt% doped samples during both heating and cooling process (Table B1 for H4TP).

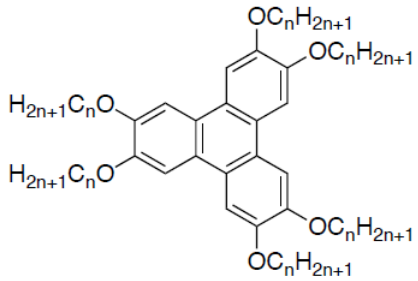

n=4 **H4TP**; Cr 85.6 Col_{hp} 144 Iso
n=6 **H6TP**; Cr 67.6 Col_{ho} 99.0 Iso

At first, temperature-controlled polarized light optical microscopy was performed as this always provides the first clues if a particular nanomaterial tends to aggregate in a liquid crystal host phase. For the given **DLC-GNR**s no such tendency was observed and aggregates that may eventually form at the higher concentration are not visible at magnifications up to 100×. For H6TP, the texture observed by POM for neat H6TP appear virtually unaltered after the addition and dispersion of the **DLC-GNR**s. Figure 3.6a-c shows the typical dendritic (right at the transition from Iso to Col_{ho}) and mosaic-type textures

(deeper into the Col_{ho} phase) textures for neat H6TP and H6TP doped with 1 and 2wt% **DLC-GNR**s.

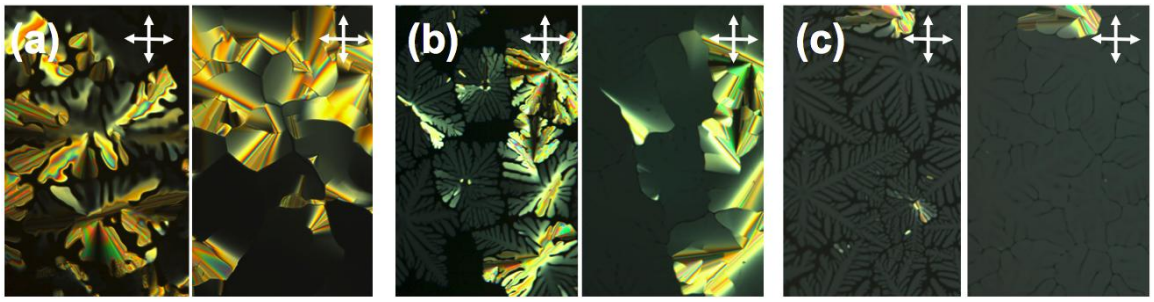

Figure 3.6. POM photomicrographs (crossed polarizers) taken on cooling at 1 ℃/min of: (a) neat H6TP at 99 ℃ (left) and 88 ℃ (right), (b) H6TP doped with 1wt% DLC-GNRs at 98 ℃ (left) and 85 ℃ (right), and (c) H6TP doped with 2wt% DLC-GNRs at 96 ℃ (left) and 85 ℃ (right).

Similar overall trends were also observed for H4TP during POM analysis as shown in Figure 3.7. For H4TP, however, highly birefringent (and rather colorful) textures were observed on cooling in a very narrow temperature interval (~1 to 2 ℃) immediately at the transition from the isotropic liquid to the Col_{hp} phase. Similar textural features have previously been described for tilted, supramolecular chiral (or racemic) columnar phases, and provide the first hint for a potentially induced tilt after inclusion of the GNRs into the hexagonal lattice of the two hosts.

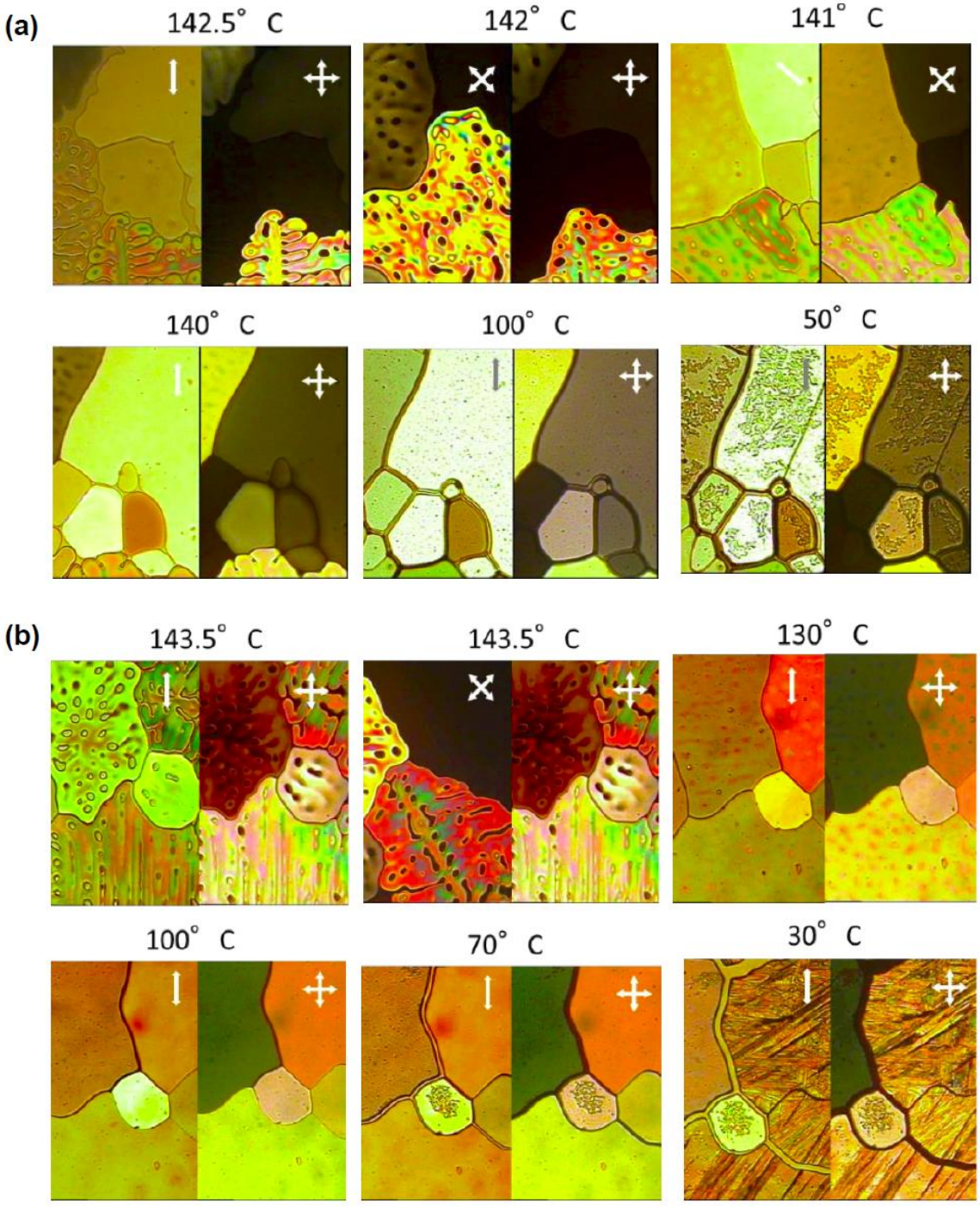

Figure 3.7. POM photomicrographs taken on cooling at 1 ℃/min (left: uncrossed polarizers; right: crossed polarizers): (a) H4TP doped with 1wt% DLC-GNRs and (b) H4TP doped with 2wt% DLC-GNRs at various temperatures. Within a very narrow temperature interval on cooling, highly birefringent and colorful textures are seen immediately below the isotropic liquid phase.

First, however, we wanted to test if the more fluid Col_{ho} of H6TP could be used to macroscopically align the **DLC-GNR**s, a critical aspect for the use of anisometric metal nanorods in potential applications as optical phase retarders or wave plates. To study this in a rather simple approach, the 1wt% **DLC-GNR**s doped H6TP sample was placed between two plain glass slides, and planar alignment of the Col_{ho} phase of H6TP was achieved by shearing the cover slide in one direction at a temperature of 85 °C. Polarized optical microscopy images of the alignment obtained for this cell are shown in Figure 3.8. Under crossed polarizers, when the shearing direction was parallel to the polarizer (director *n* of the aligned H6TP molecules, yellow arrow), the aligned cells gave the weakest birefringence (Figure 3.8a). The birefringence reached the maximum when the shearing direction was 45 ° with respect to both polarizers (Figure 3.8b) indicating the planar alignment of H6TP in these non-treated cells. In order to investigate the orientation (alignment) of the **DLC-GNR**s doped in the superstructure of H6TP, the planar aligned cell was studied using linearly polarized UV-Vis-NIR spectrophotometry. From the spectra of the polarized absorption experiments (Figure 3.8c), the absorbance band at around 800 nm corresponding to the longitudinal SPR of the GNRs is tunable by rotating the planar aligned thin Col_{ho} film. The intensity of this band decreased when the angle between polarizer and the director *n* is rotated from 0 ° to 90 ° and it reaches the minimum intensity at 90 °, while the polarization of the beam is perpendicular to the transversal direction of the **DLC-GNR**s. This is in principle also true for the transversal SPR band centered around 535 nm (zero absorbance at 0 ° and 10 °, maximum absorbance at 90 °, 45 ° making the logical exception), which indicates that the majority of the **DLC-GNR**s in the

aligned cell follows the director *n* with their long axes a shown in the insert of Figure 3.8c.

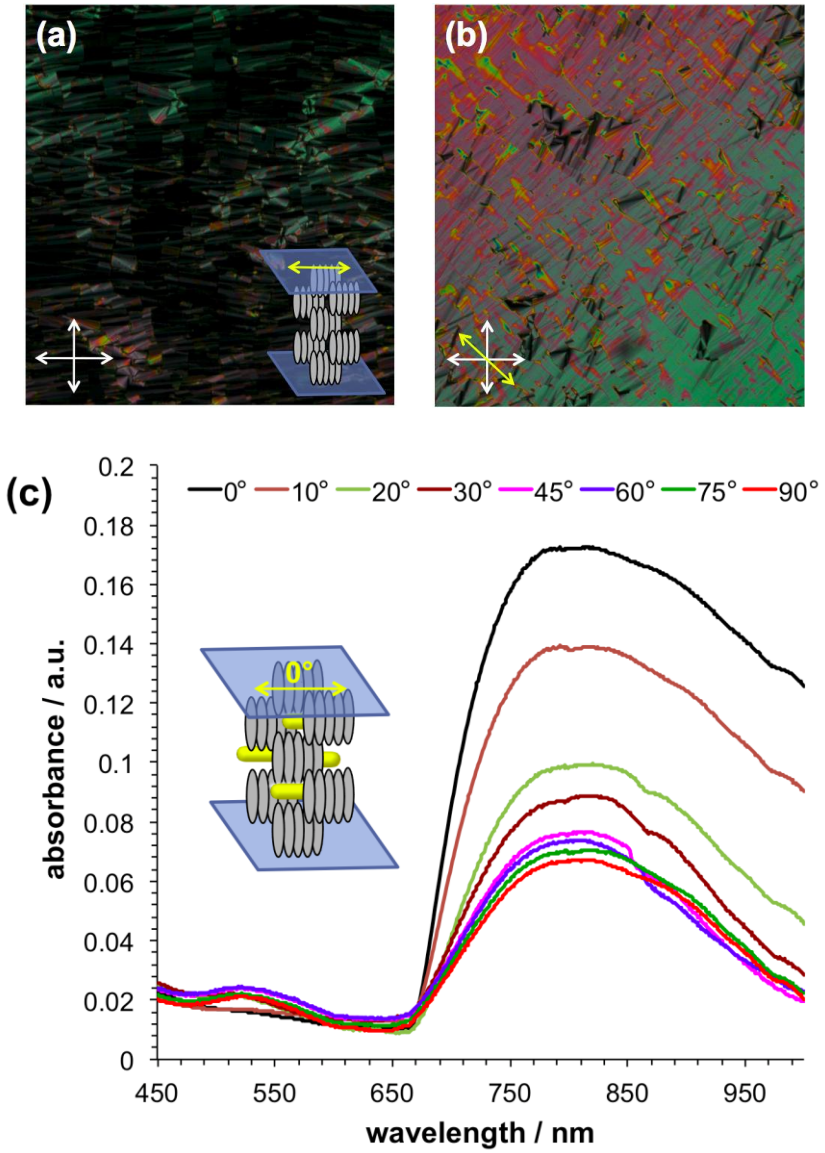

Figure 3.8. (a, b) Polarized optical micrographs of the planar alignment cell of H6TP doped with 1 wt% of DLC-GNRs, (c) polarized UV-Vis-NIR spectra of the DLC-GNRs doped in H6TP (planar aligned cell) at different polarizer rotation angles.

The polarized UV-Vis-NIR spectrum at 90 °shows as expected the weakest absorbance at 800 nm, but not zero, which means that the alignment of H6TP is not perfect (as can actually be seen in Figure 3.8a) but potentially also that a portion of the GNRs is not per-

fectly aligned along the director. As one can see from Figure 3.8a, some areas still have weak birefringence showing as bright domains. The order parameter *S* of the **DLC-GNR**s can be calculated using the following equation: [22]

$$S = \frac{A_{\parallel} - A_{\perp}}{A_{\parallel} + 2A_{\perp}}$$

where $A_{\parallel}$ and $A_{\perp}$is the absorbance measured with the polarizer either parallel or perpendicular to the director *n*, respectively. The resulting order parameter *S* (dichroic ratio) was calculated to be 0.38. Considering that the typical order parameter of planar alignment of columnar phase of discotic LCs achieved by mechanical shearing [23] is in the vicinity of 0.5, the **DLC-GNR**s inserted into the planar alignment columnar phase are aligned along the director *n* with an over 75% efficiency.

With POM and UV-Vis-NIR experiments suggesting that the **DLC-GNR**s are reasonably well dispersed in the hexagonal columnar LC phases of both H4TP and H6TP, we sought to determine if the suspended GNRs have any effect on the organization and structure of the host phase by performing medium and wide-angle X-ray diffraction experiments. While we have not been able to pinpoint and carefully study the potential high-temperature modification exhibiting the bright, highly birefringent textures for the 1 wt% and 2 wt% **DLC-GNR** in H4TP mixtures (too narrow temperature interval), the obtained X-ray diffraction data did reveal some rather unique trends when both hosts are doped with the **DLC-GNR**s. In both cases, we selected the same temperature well below the Iso/Col_h phase transition temperature (since DSC and POM revealed no thermal effect of the addition of the **DLC-GNR**s in the two hosts) on cooling (80 ℃ for H6TP and 125 ℃

for H4TP) and collected x-ray diffraction data, which are shown in Figure 3.9 and summarized in Table 3.1.

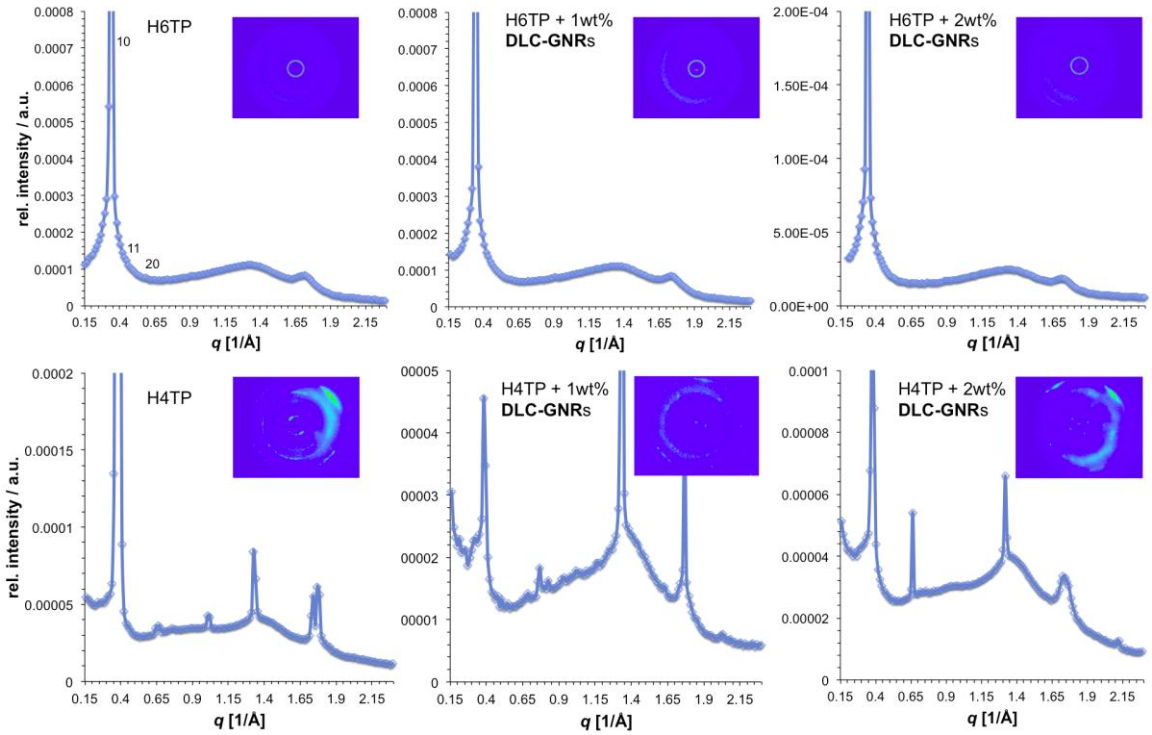

Figure 3.9. X-ray diffraction pattern and azimuthally averaged intensity data of the scattering vector (q in $Å^{-1}$) from the 2D pattern shown as insets.

Table 3.1. Measured scattering vectors (q in $Å^{-1}$) with respective Miller indices, and calculated d spacing as well as lattice parameters of the Col_h phase in nm. The intracolumnar distance refers to the distance between molten hydrocarbon chains, the core-core distance to the distance between the triphenylene cores within the columnar aggregates.

					Stacking periodicities / nm	
Sample	T / ℃	$q_{(hkl)}$ / $Å^{-1}$	d / nm	a_{hex} / nm	*Intra-columnar*	*Core-Core*
H6TP	80	$q_{(100)}$ = 0.3218 $q_{(110)}$ = 0.5447 $q_{(200)}$ = 0.656	1.953	2.252		

		q = 1.27 q = 1.66			0.495	0.379
H6TP + 1wt% **DLC-GNRs**	80	$q_{(100)}$ = 0.3485 $q_{(110)}$ = 0.614 q = 1.316 q = 1.714	1.803	2.082	0.477	0.367
H6TP + 2wt% **DLC-GNRs**	80	$q_{(100)}$ = 0.3231 $q_{(110)}$ = 0.608 q = 1.28 q = 1.658	1.945	2.246	0.491	0.379
H4TP	125	$q_{(100)}$ = 0.3539 $q_{(110)}$ = 0.645 $q_{(200)}$ = 0.7148 $q_{(210)}$ = 0.992 $q_{(220)(211)}$ = 1.311 $q_{(311)(320)}$ = 1.728 $q_{(002)}$ = 1.7557	1.775	2.05	0.479	0.358
H4TP + 1wt% **DLC-GNRs**	125	$q_{(100)}$ = 0.3673 $q_{(110)}$ = 0.6307 $q_{(200)}$ = 0.7415 $q_{(220)(211)}$ = 1.324 $q_{(002)}$ = 1.7534	1.711	1.975	0.475	0.358
H4TP + 2wt% **DLC-GNRs**	125	$q_{(100)}$ = 0.3759 $q_{(110)}$ = 0.6629 $q_{(200)}$ = 0.7176 $q_{(210)}$ = 0.95 $q_{(220)(211)}$ = 1.319 $q_{(311)(320)}$ = 1.729 $q_{(002)}$ = 1.7564	1.672	1.93	0.476	0.363

First, the diffraction pattern of both pure H6TP and H4TP perfectly match data published previously[24] . Second, the packing of H4TP appears to be more significantly impacted by the dispersion of the **DLC-GNR**s than H6TP at least judging from the plot of the scattering intensity vs. *q*, with some with the (311)/(320) diffraction peak disappearing and a completely altered intensity profile. The calculated data for the *d* spacing and the lattice parameter a_{hex} (from d_{100}), however, indicate that there is only a minor decrease in a_{hex} for H4TP, but a significant decrease for H6TP both doped with 1 wt% **DLC-GNR**s, but not for the 2 wt% doped sample. While one would expect an increase in *d* spacing (and lattice parameter) [25] upon insertion of GNRs with a much larger diameter, the lattice parameter for the 1 wt% **DLC-GNR**s in H6TP sample decreases by about 8 %, which at this point could only be explained by a more efficient inter-digitation of the alkyl chains surrounding the triphenylene cores of H6TP. Here, the insertion of the GNRs might lead to packing mismatch between DLC molecules attached to the GNR surface and DLC molecules of the host. At the volume fraction of 1 wt% of **DLC-GNR**s in H6TP, such packing mismatch could lead to packing frustration that might be compensated by a larger degree of inter-digitation. Such process, however, would be more pronounced with H6TP than H4TP because of the longer hydrocarbon chains (see schematics in Figures 3.10 and 3.11). Such inter-digitation would be less significant for H4TP because of the shorter chain length, which is supported by the less significant decrease in *d* (and a_{hex}) for H4TP doped with 1 wt% **DLC-GNR** (see Table 3.1). For H4TP this packing frustration reaches its maximum at 2 wt% DLC-GNRs indicated by a decrease of a_{hex} to 1.93 nm (a 6 % decrease). The intra-columnar spacing however remains virtually identical. For H6TP, both the intra-columnar distance between the molten alkyl chains and

the core-core distance simultaneously decreases, most considerably for the 1 wt% doped H6TP, with a core-core distance decrease from 0.379 to 0.367 nm. However, once the concentration of the DLC-GNRs is doubled to 2 wt%, most likely an onset of aggregation of the GNRs minimizes these packing effects and the lattice relaxes back to the values of the non-doped H6TP host phase. Another possibility to explain a decrease of both a_{hex} and core-core distance would be a molecular tilt of the molecules within the columns (23 ° to be exact), but this can be ruled out as the resulting phase would have a different symmetry. Such molecular tilt would give rise to an elliptical cross-section of the columns leading to an assignment as a rectangular columnar phase (Col_r). In neither case do the powder XRD pattern support such phase symmetry and assignment. However, the insertion of the GNRs, at least at lower volume fractions induces a tighter packing of the host molecules both inter and intra-columnar at 1 wt% for H6TP, which should give rise to a higher charge-carrier mobility in these phases, which we tested next using transient photocurrent measurements. For H4TP exclusively the inter-columnar packing decrease at 2 wt% DLC-GNRs, which should in principle not affect the charge carrier mobility unless other electronic processes or ionic contributions are active.

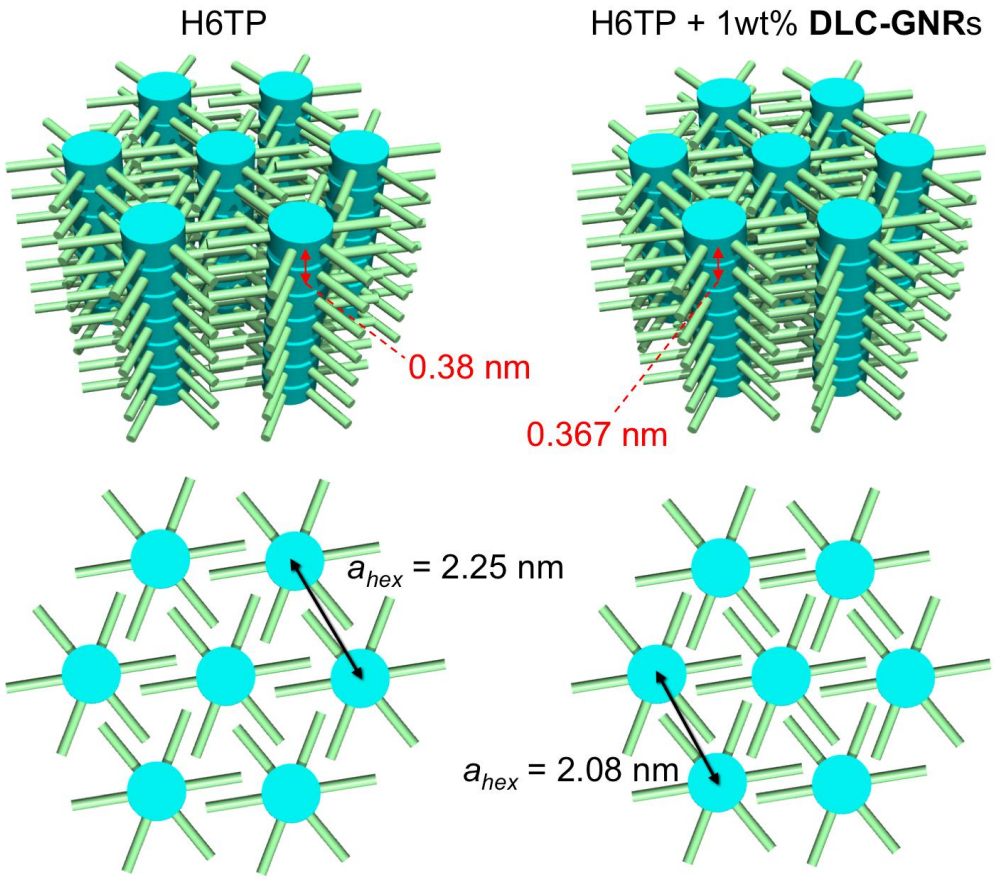

Figure 3.10. Schematic of the Col_{ho} phase of H6TP and H6TP doped with 1wt% DLC-GNRs showing the decrease in lattice parameter as well as intra-columnar packing.

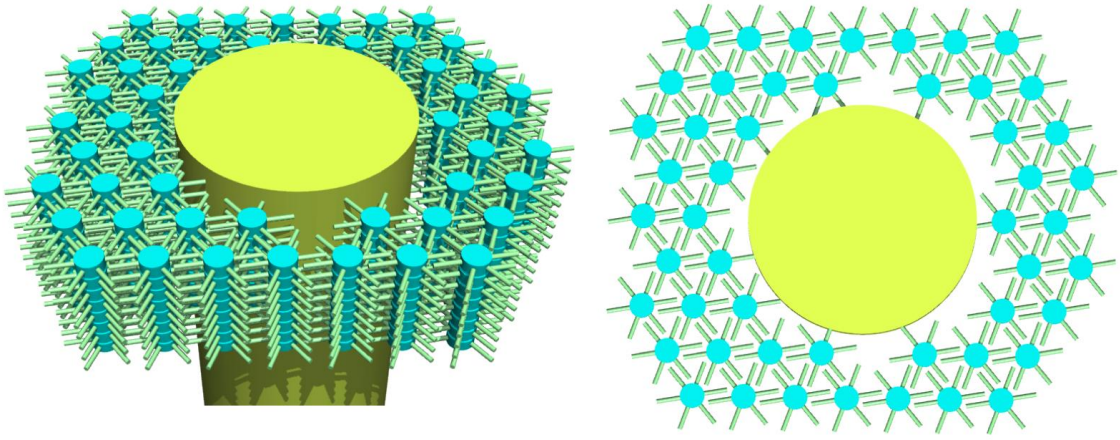

Figure 3.11. Schematic of the H6TP (or H4TP) doped with 1 wt% DLC-GNRs (3D and top 2D view) showing potential packing inefficiencies around a single DLC-capped GNR that are potentially compensated as determined by XRD.

These measurements require extremely pure samples and ideally excellent homeotropic alignment in thin, ITO-coated cells (cell gap: 2-3 μm), and the most reliable data sets were acquired for the ultrapure H4TP synthesized and purified previously by Shimizu and co-workers. [24] The use of thin cells for TOF measurements shows a direct effect on the alignment of the **DLC-GNR** composites. While we were unable to obtain complete homeotropic alignment in cells with a ≈15 μm cell gap, it occurred spontaneously for the 1 wt% **DLC-GNR**/H4TP composite in the ≈3 μm thin cell, and remained present throughout the whole temperature range analyzed on cooling (from 141 to 20 ℃). The 2 wt% composite also shows homeotropic regions albeit significantly smaller (see Figure B3). The presence of homeotropic regions in the **DLC-GNR**s composites contributes to the enhancement of the hole mobility as it reflects an increased uniaxial ordering along the columnar axis that is absent in the pure H4TP sample.

Figures 3.12 and 3.13 show the obtained transient photocurrent decay curves for both hole and electron transports for H4TP doped with 1 and 2 wt% **DLC-GNR** s and H6TP doped with 1 wt% **DLC-GNR** s (hole mobility only). H4TP and H6TP are known to show ambipolar character for the charge transport in electronic processes, [32] and in comparison to those of the pure, undoped compounds, the GNR-doped systems tend to show noisy and less qualified decay curves, although an electric field-independent character of the mobility is still observed (see Figure B4). This may indicate that local disordering of the discotic molecules is induced by the addition of the surface modified **DLC-GNR**s. H4TP and H6TP both exhibit hexagonal columnar (Col_h) phases, however with a slight difference in the molecular ordering. The shorter chain homologue, H4TP shows a 3D-plastic columnar phase with a 2D hexagonal arrangement of columns (Col_{hp} phase), [27]

whilst H6TP displays a Col_{ho} mesophase with some degree of ordering along the columnar axis (see X-ray diffraction data in Figure 3.9). Their hole and electron mobilities are recorded on the order of 10^{-2} and 10^{-4} cm^2 V^{-1} s^{-1} for the Col_{hp} and the Col_{ho} phase, respectively, and both show largely temperature independent character. [24] The temperature dependencies of the charge carrier mobility for the two composites of H4TP are depicted in Figure 3.14. All essentially show a temperature independent nature for both holes and electrons except for a sudden jump at about 115 ℃ for the electron mobility. There is no evidence of a phase transition, although an optical texture change indicates a potential phase or structure modification within these domains around this temperature (see Figure 3.14 b). This change in the optical textures is best described by a slight widening of the domain boundaries (Figure 3.7), although DSC measurements show no first order phase transition in this temperature range. Interestingly, this sudden change in mobility is not seen for the hole mobility, which drops for the 2 wt% mixture, likely due to an onset of aggregation of the DLC-GNRs in H4TP, but otherwise increases below the Cr/Col_{hp} phase transition (rather than decrease for neat H4TP). Overall, the mobilities of both holes and electrons are comparable to those of pure H4TP in the LC phase, and the mixture of 1 wt% DLC-GNRs in H4TP shows a slightly higher value of the mobility. This may indicate that the optimal concentration of the **DLC-GNR** s would exist around this concentration and provide the maximum mobility. For the 1wt% **DLC-GNR** composite with H6TP, the mobility behavior is similar to those of the composites with H4TP. Here, the measured hole mobility measured for the composite is slightly higher than the one of pure H6TP ($\approx 3.2\times10^{-4}$ cm^2 V^{-1} s^{-1} for the composite vs 2.0×10^{-4} cm^2 V^{-1} s^{-1} for neat H6TP over the Col_{ho} mesophase range. [24] The charge carrier mobilities obtained for

undoped H4TP as well as the composites with **DLC-GNRs** are summarized in Table 3.2, and the data for H6TP are collected in the Supporting Information (POM and hole mobility, see Figure B5).

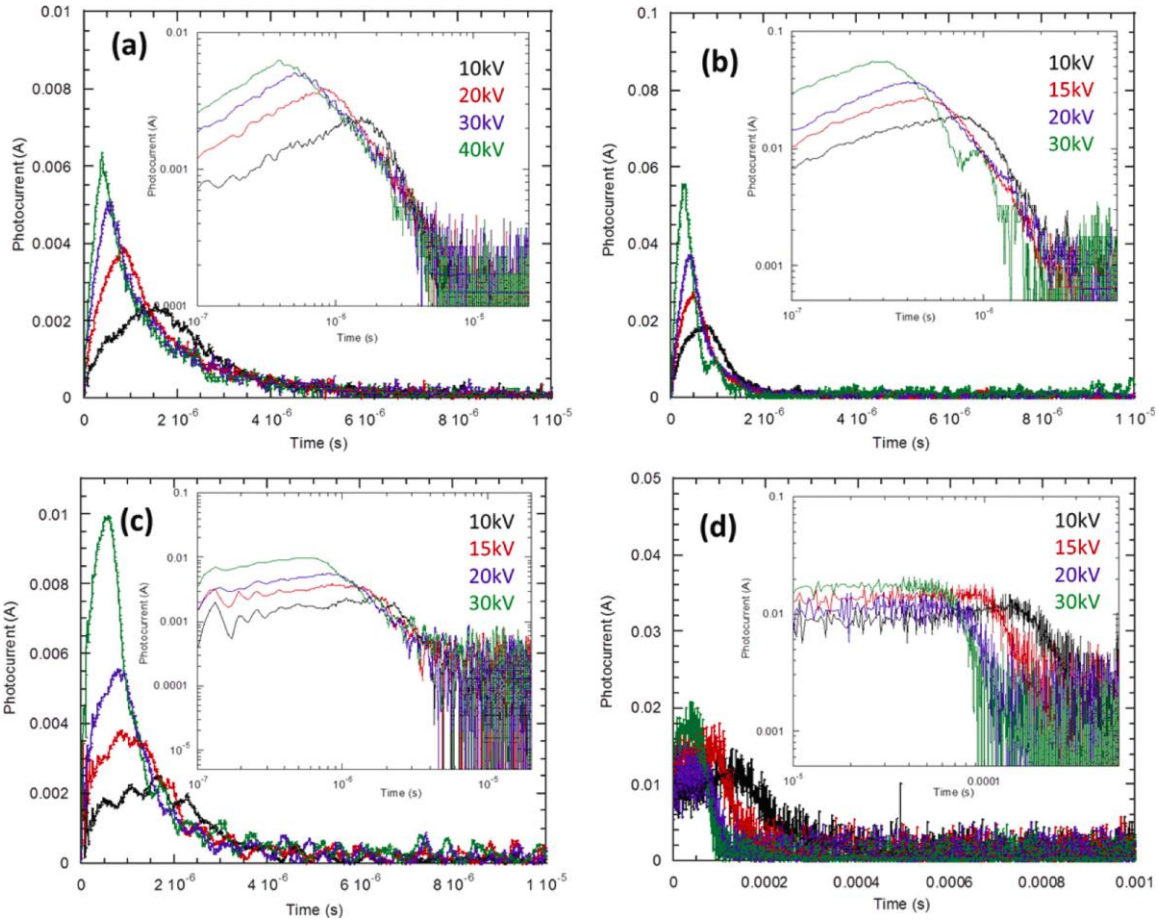

Figure 3.12. Bias dependence of the hole mobility of: a) pure H4TP, b) 1 wt% DLC-GNR s in H4TP, c) 2 wt% DLC-GNR s in H4TP (all three at 140 ℃ in the Col_{hp} phase), and d) 1 wt% DLC-GNRs in H6TP (at 90 ℃ in the Col_{ho} phase).

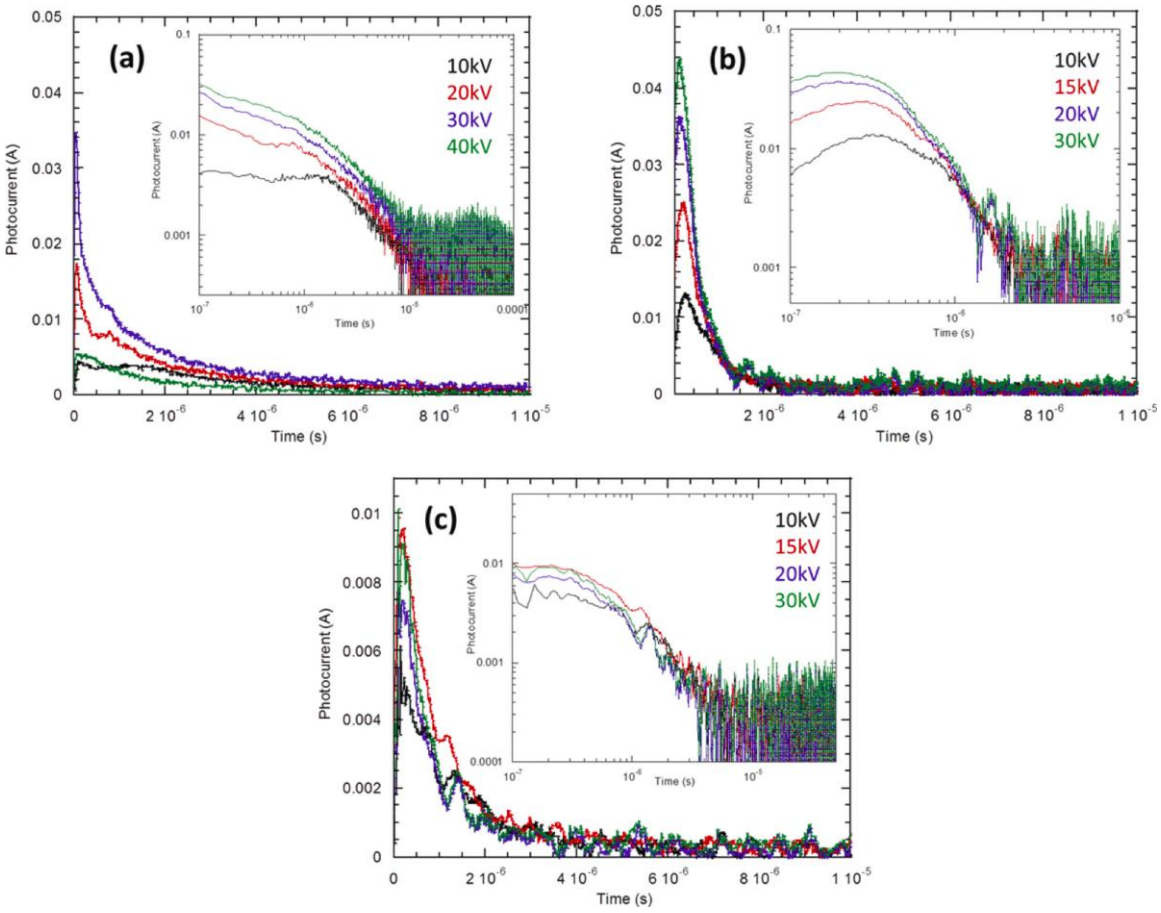

Figure 3.13. Bias dependence of the electron mobility of: a) pure H4TP, b) 1 wt% **DLC-GNR** s in H4TP, c) 2 wt% **DLC-GNR** s in H4TP (at 140 ℃ in the Col_{hp} phase).

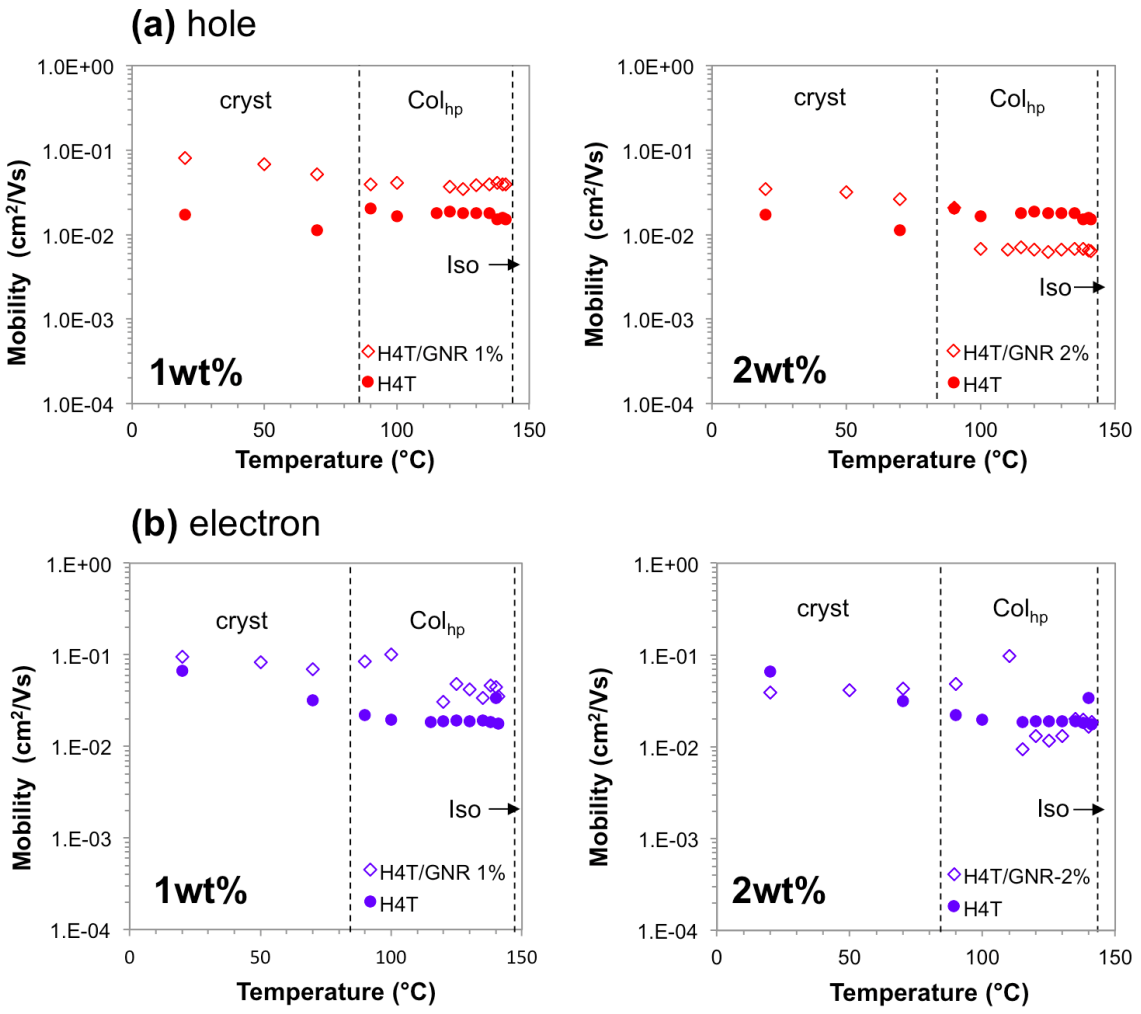

Figure 3.14. Temperature dependence of hole and electron mobilities for: (a) 1 wt% and (b) 2 wt% DLC-GNR in H4TP at 10 kV cm^{-1}.

Kumar *et al.* reported an enhancement of the conductivity with an inclusion of GNRs (1 wt% for H5TP) from 10^{-9} to 10^{-6} Sm^{-1} in the Col_h phase, while the conductivity is higher than in the Iso phase (10^{-7} Sm^{-1}). [25, 28] A related enhancement of the conductivity was also reported for composites with gold nanoparticles dispersed in H6TP. [33] The conductivity is a function of the number of efficient charges in the system and their mobility. Enhancement of the conductivity is thus the result of an increased number of carriers mobile in the system and/or improved mobility of the charge carriers. Hence, in both

composites of 1 and 2 wt% **DLC-GNR**s in H4TP, the enhanced conductivity reported is best explained by an increase in the number of efficient charges. If we assume that the charge conduction in this system is only arising from electronic processes, the doping of GNRs would have to elevate the number of charges. On the other hand, conductivity phenomena essentially include ionic transport processes. In particular, soft states of matter such as LC phases sometimes provide a good ionic charge transport path. [29] Considering that the mobilities measured using the TOF technique are rather high in comparison to those of ionic mobility, and that the temperature dependence obeys Arrhenius formalism, the enhanced conductivity is probably derived from charge transport in ionic processes.

Table 3.2. Carrier mobility for H4TP and H4TP doped with 1 wt% and 2 wt% DLC-GNRs.

Sample	Charge carrier mobility (10^{-2} cm^2/Vs)			
	hole		electron	
	Col_{hp}	Cr	Col_{hp}	Cr
neat H4TP	1.7	1.4	2.0	4.9
H4TP (1wt% **DLC-GNR**s)	3.9	6.7	5.2	8.2
H4TP (2wt% **DLC-GNR**s)	0.7	3.1	2.4	4.1

3.4 Conclusions

In continuation of our earlier experiments on the reconfigurable self-assembly of nematic liquid crystal capped GNRs[10, 16], we here demonstrate that GNRs functionalized with DLC π-π stacking motifs also fosters long-range, bulk self-assembly and permits alignment in a parent DLC host. The as-synthesized **DLC-GNR**s can be homogeneously dispersed in organic solvents such as toluene and chloroform at fairly high concentration. These dispersions, dried on TEM grids, flat substrates, or in the bulk show large area self-assembly of the as observed by TEM and SAXS. However, true liquid crystalline behavior could not be observed. The proposed stacking assembly model is supported by distance measurements using TEM image analysis and SAXS showing identical distances between side-by-side self-assembled GNRs based on π-π molecular stacks between neighboring GNRs. In combination with our earlier data regarding the distances between nematic LC functionalized GNRs[10], the inter-particle distance, i.e. the coupling effect[30], can be fine tuned by the LC packing mode, which shows promise for potential application as metamaterials or field-enhanced spectroscopy units in electric and optical

nanodevices[11,31]. Furthermore, we have demonstrated that the DLC-functionalized GNRs are compatible with parent DLC hosts. The enhanced thermal stability provided by the silane conjugation approach allows us to disperse these DLC-capped GNRs without the risk of thiol desorption from the GNR surface eliminating the risk of free thiols contributing both positively or negatively to the observed effects. Homogeneous dispersion and uniform alignment of the DLC-functionalized GNRs has been achieved in a planar aligned H6TP DLC host over areas as large as several cm^2, employing a very simple and well-established alignment technique for DLCs without any electric or magnetic field. These composites show rather unique structural features particularly at the lower concentration of 1 % by weight. SAXS data reveal that the lattice parameter decreases from 2.25 nm to 2.08 nm for the host featuring longer hydrocarbon chains (H6TP) at 1 wt% of dispersed GNRs and relaxes back to 2.25 nm when the concentration of the GNRs is doubled. This effect is more pronounced for the less viscous H6TP forming the Col_{ho} phase in comparison to the more viscous H4TP forming a plastic Col_{hp} phase. Simultaneously, the intracolumnar distances also decrease at the lower concentration of GNRs especially in H6TP, which gives rise to an increase in the charge carrier mobility for both electrons and holes. These results indicate that the inclusion of the **DLC-GNR**s into the hexagonal columnar LC affects the charge transport efficiency only slightly at the lower concentration range of dispersed GNRs. However, the interdigitation of columnar semiconductors and functionalized metal nanorods as conducting active parts and electrodes, respectively, may provide a simple yet effective strategy for organic photovoltaics.

Acknowledgements

The authors would like to thank the Province of Manitoba for a grant from the Science and Technology International Collaboration Fund, the Natural Science and Engineering Research Council (NSERC) of Canada, the Canada Foundation for Innovation (CFI), and the Manitoba Research and Innovation Fund (MRIF) for financial support. TH also acknowledges financial support from Kent State University and the Government of Ohio's Third Frontier Program for Ohio Research Scholars. TM is grateful for financial support through a JSPS fellowship. LS and YS acknowledge JST for the finical support under the ALCA program. Special thanks go to Dr. Kevin McEleney for his help with the SAXS experiments and to Andre Dufresne for all the help and assistance with TEM imaging.

References

[1] (a) T. Hegmann, H. Qi, V. M. Marx, *J. Inorg. Organomet. Polym. Mater.* **2007**, *17*, 483-508; (b) U. Shivakumar, J. Mirzaei, X. Feng, A. Sharma, P. Moreira, T. Hegmann, *Liq. Cryst.* **2011**, *38*, 1495-1514; (c) O. Stamatoiu, J. Mirzaei, X. Feng, T. Hegmann, *Top. Curr. Chem.* **2012**, *318*, 331-393; (d) G. L. Nealon, R. Greget, C. Dominguez, Z. T. Nagy, D. Guillon, J. L. Gallani, B. Donnio, *Beilstein J. Org. Chem.* **2012**, *8*, 349-370; (e) W. Lewandowski, M. Wójcik, E. Górecka, *ChemPhysChem* **2014**, *15*, 1283-1295; (f) S. Umadevi, V. Ganesh, T. Hegmann, In *Handbook of Liquid Crystals*, 2nd. Edition, J. W. Goodby, P. J. Collings, T. Kato, C. Tschierske, H. F. Gleeson, P. Raynes (Eds.), Vol. 6, pp. 27-76, Wiley-VCH, Weinheim, Germany **2014**.

[2] (a) M. Grzelczak, L. M. Liz-Marzan, *Langmuir* **2013**, *29*, 4652-4663; (b) M. Zorn, R. Zentel, *Macromol. Rapid Comm.* **2008**, *29*, 922-927; (c) C. M. Soukoulis, S. Linden, M. Wegener, *Science* **2007**, *315*, 47-49; (d) V. M. Shalaev, *Nat. Photonics* **2007**, *1*, 41-48; (e) S. Meuer, P. Oberle, P. Theato, W. Tremel, R. Zentel, *Adv. Mater.* **2007**, *19*, 2073-2078; (f) S. Meuer, L. Braun, R. Zentel, *Chem. Commun.* **2008**, 3166-3168; (g) A. B. Golovin, O. D. Lavrentovich, *Appl. Phys. Lett.* **2009**, *95*, 254104; (h) A. B. Golovin, J. Xiang, H. S. Park, L. Tortora, Y. A. Nastishin, S. V. Shiyanovskii, O. D. Lavrentovich, *Materials* **2011**, *4*, 390-416.

[3] (a) J. J. Zhou, G. X. Chen, E. Wu, G. Bi, B. T. Wu, Y. Teng, S. F. Zhou, J. R. Qiu, *Nano Lett.* **2013**, *13*, 2241-2246; (b) T. Wang, X. R. Wang, D. LaMontagne, Z. W. Wang, Y. C. Cao, *J. Am. Chem. Soc.* **2013**, *135*, 6022-6025; (c) Y. Zhao, A. Alu, *Nano Lett.* **2013**, *13*, 1086-1091; (d) X. P. Li, T. H. Lan, C. H. Tien, M. Gu, *Nat. Commun.* **2012**, *3*, 1-5.

[4] X. Y. Zheng, J. Fontana, M. Pevnyi, M. Ignatenko, S. Wang, R. Vaia, P. Palffy-Muhoray, *J. Mater. Sci.* **2012**, *47*, 4914-4920.

[5] Y. Q. Wang, B. Yan, L. X. Chen, *Chem. Rev.* **2013**, *113*, 1391-1428.

[6] (a) E. V. Shevchenko, D. V. Talapin, N. A. Kotov, S. O'Brien, C. B. Murray, *Nature* **2006**, *439*, 55-59; (b) S. C. Glotzer, M. J. Solomon, *Nat. Mater.* **2007**, *6*, 557-562.

[7] (a) Y. J. Min, M. Akbulut, K. Kristiansen, Y. Golan, J. Israelachvili, *Nat. Mater.* **2008**, *7*, 527-538; (b) K. J. M. Bishop, C. E. Wilmer, S. Soh, B. A. Grzybowski, *Small* **2009**, *5*, 1600-1630.

[8] T. S. Sreeprasad, T. Pradeep, *Langmuir* **2011**, *27*, 3381-3390.

[9] A. Guerrero-Martinez, J. Perez-Juste, E. Carbo-Argibay, G. Tardajos, L. M. Liz-Marzan, *Angew. Chem. Int. Ed.* **2009**, *48*, 9484-9488.

[10] S. Umadevi, X. Feng, T. Hegmann, *Adv. Funct. Mater.* **2013**, *23*, 1393-1403.

[11] M. Yamada, Z. R. Shen, M. Miyake, *Chem. Commun.* **2006**, 2569-2571.

[12] (a) S. Kumar, S. K. Pal, P. S. Kumar, V. Lakshminarayanan, *Soft Matter* **2007**, *3*, 896- 900; (b) S. Kumar, H. K. Bisoyi, *Angew. Chem. Int. Ed.* **2007**, *46*, 1501-1503.

[13] J. Mirzaei, M. Urbanski, H. S. Kitzerow, T. Hegmann, *Phil. Trans. R. Soc. A* **2013**, *371*, 20120256.

[14] S. Kumar, M. Manickam, *Synthesis-Stuttgart* **1998**, 1119-1122.

[15] (a) J. L. Schulte, S. Laschat, V. Vill, E. Nishikawa, H. Finkelmann, M. Nimtz, *Eur. J. Org. Chem.* **1998**, 2499-2506; (b) H. Schönherr, F. J. B. Kremer, S. Kumar, J. A. Rego, H. Wolf, H. Ringsdorf, M. Jaschke, H. J. Butt, E. Bamberg, *J. Am. Chem. Soc.* **1996**, *118*, 13051-13057.

[16] S. Umadevi, X. Feng, T. Hegmann, *Ferroelectrics* **2012**, *431*, 164-175.

[17] K. Mitamura, T. Imae, N. Saito, O. Takai, *J. Phys. Chem. B* **2007**, *111*, 8891-8898.

[18] B. Nikoobakht, M. A. El-Sayed, *Chem. Mater.* **2003**, *15*, 1957-1962.

[19] S. L. Pan, Z. J. Wang, L. J. Rothberg, *J. Phys. Chem. B* **2006**, *110*, 17383-17387.

[20] M. R. Thomas, S. Klein, R. J. Greasty, S. Mann, A. W. Perriman, R. M. Richardson, *Adv. Mater.* **2012**, *24*, 4424-4429.

[21] D. V. Leff, P. C. Ohara, J. R. Heath, W. M. Gelbart, *J. Phys. Chem.* **1995**, *99*, 7036-7041.

[22] B. Bahadur, In *Handbook of Liquid Crystals, 1st Edition*, J. W. Goodby, D. Demus, G. Gray, H.-W. Spiess, V. Vill (Eds.), Vol. 2A, pp. 257-302, Wiley-VCH, Weinheim, Germany **1998**.

[23] Q. K. Liu, Y. X. Cui, D. Gardner, X. Li, S. L. He, I. I. Smalyukh, *Nano Lett.* **2010**, *10*, 1347-1353.

[24] H. Monobe, Y. Shimizu, S. Okamoto, H. Enomoto, *Mol. Cryst. Liq. Cryst.* **2007**, *476*, 277-287.

[25] S. Kumar, *NPG Asia Mater* **2014**, *6*, e82.

[26] F. Nekelson, H. Monobe, M. Shiro, Y. Shimizu, *J. Mater. Chem.* **2007**, *17*, 2607-2615.

[27] J. Simmerer, B. Glusen, W. Paulus, A. Kettner, P. Schuhmacher, D. Adam, K. H. Etzbach, K. Siemensmeyer, J. H. Wendorff, H. Ringsdorf, D. Haarer, *Adv. Mater.* **1996**, *8*, 815.

[28] B. S. Avinash, V. Lakshminarayanan, S. Kumar, J. K. Vij, *Chem. Commun.* **2013**, *49*, 978-980.

[29] (a) K. Kishimoto, T. Suzawa, T. Yokota, T. Mukai, H. Ohno, T. Kato, *J. Am. Chem. Soc.* **2005**, *127*, 15618; (b) M. Yoshio, T. Mukai, H. Ohno, T. Kato, *J. Am. Chem. Soc.* **2004**, *126*, 994-995.

[30] K. H. Su, Q. H. Wei, X. Zhang, J. J. Mock, D. R. Smith, S. Schultz, *Nano Lett.* **2003**, *3*, 1087-1090.

[31] (a) J. Aizpurua, G. W. Bryant, L. J. Richter, F. J. G. de Abajo, B. K. Kelley, T. Mallouk, *Phys. Rev. B* **2005**, *71*, 235420; (b) V. M. Shalaev, W. S. Cai, U. K.

Chettiar, H. K. Yuan, A. K. Sarychev, V. P. Drachev, A. V. Kildishev, *Opt. Lett.* **2005**, *30*, 3356-3358.

[32] H. Iino, J. Hanna, D. Haarer, R. J. Bushby, *Jpn. J. Appl. Phys.* **2006**, *45*, 430.

[33] L. A. Holt, R. J. Bushby, S. D. Evans, A. Burgess, G. Seeley, *J. Appl.Phys.* **2008**, *103*, 063712.

[34] (a) M. Grzybowski, K. Skonieczny, H. Butenschçn, D. T. Gryko, *Angew. Chem. Int. Ed.* **2013**, *52*, 9900-9930; (b) H. Naarmann, M. Hanack, R. Mattmer, *Synthesis* **1994**, 477-478; (c) F. Toda, K. Tanaka, F. Iwata, *J. Org. Chem.* 1**989**, *54*, 3007.

Appendix B

Supplimentary Information of Chapter 3

Detailed experimental procedures and analytical data for compounds 1-4:

2,3,6,7,10,11-hexakis(hexyloxy)triphenylene **1** (H6TP): 1,2-Bishexyloxybenzene (11.3 g, 0.04 mol) was dissolved in 40 mL CH_2Cl_2, followed by adding 1 drop of H_2SO_4 (98%). Then $FeCl_3$ (anhydrous, 12.97 g, 0.08 mol) was slowly added in to the solution under stirring. The mixture was kept under stirring for 1 hour before poured into MeOH (300 mL, -18 ℃) under vigorous stirring. The precipitate was separated and purified by chromatographic column using the eluent of petroleum ether/ethyl acetate = 20/1. The product is a white solid. ^{1}H NMR ($CDCl_3$): δ 7.84 (s, 6H, Ar*H*), 4.25 (t, 12H, ArOCH_2R), 1.96 (m, 12H, OCH_2CH_2), 1.3-1.7 (m, 36H, CH_2), 0.96 (t, 18H, CH_3).

3,6,7,10,11-pentakis(hexyloxy)triphenylen-2-ol **2**: A solution of H6TP, **1**, (0.67 g, 0.5 mmol) in anhydrous CH_2Cl_2 (10 mL) was cooled to 0 ℃ before 1.2 eq. (0.12 g, 0.6 mmol) B-bromocatecholborane (dissolved in 1 mL CH_2Cl_2) was added dropwise. The mixture was keeping stirring at room temperature for 72 h before poured on ice water (50 mL), and the water layer was extracted with CH_2Cl_2 (twice with 20 mL). The organic layer was separated, dried, and evaporated. The crude compound was purified by column chromatography (hexanes/ethyl acetate = 30/1). The resulting product is a dark brown crystalline solid. ^{1}H NMR ($CDCl_3$): δ 7.98 (s, 1H, Ar*H*), 7.85 (m, 4H, Ar*H*), 7.79 (s, 1H,

Ar*H*), 5.95 (s, 1H, O*H*), 4.24 (m, 10H, OCH_2), 1.96 (m, 10H, OCH_2CH_2), 1.3-1.7 (m, 30H, CH_2), 0.96 (t, 15H, CH_3).

2,3,6,7,10-pentakis(hexyloxy)-11-(undec-10-en-1-yloxy)triphenylene **3**: Compound **2** (0.18 g, 0.24 mmol) was dissolved in 10 mL THF, and KOH (0.013 g, 0.24 mmol) was added under stirring. The reaction was refluxed for 1 h before 11-bromo-1-undecene (0.174 ml, 0.8 mmol) was injected. The system was kept under reflux for 24 h before poured into 20 mL 1M HCl, and extracted with CH_2Cl_2 (twice 20 mL). The resulting crude compound **3** was purified by recrystallization from *n*-hexane (Cr 30.5 Col 57.5 Iso). ^{1}H NMR ($CDCl_3$): δ 7.84 (s, 6H, Ar*H*), 5.81 (m, 1H, RC*H*=CH_2), 4.98 (t, 2H, RCH=CH_2), 4.24 (t, 12H, OCH_2), 2.10 (m, 2H, RCH_2CH=CH_2), 1.96 (m, 12H, OCH_2CH_2), 1.3-1.7 (m, 42H, CH_2), 0.96 (t, 15H, CH_3).

Trimethoxy(11-((3,6,7,10,11-pentakis(hexyloxy)triphenylen-2-yl)oxy)undecyl)silane **4**[‡]: Compound **3** (0.09 g, 0.1 mmol) was then dissolved in 2 mL dry toluene, and under stirring, 64 μL of trimethoxysilane (0.5 mmol) and 20 μL of Karstedt's catalyst (0.1M in xylene) was added subsequently. The reaction was kept under stirring at room temperature for 24 h. The resulted trimethoxysilane compound **4** was dissolved in $CHCl_3$ and purified by filtration through a 0.45 μm PTFE syringe micro-filter before the silane conjugation reaction to the MPS-coated GNRs. ^{1}H NMR ($CDCl_3$): δ 7.84 (s, 6H, Ar*H*), 4.24 (t, 12H, ArOCH_2), 3.62 (s, 9H, SiOCH_3), 1.96 (m, 12H, $ArOCH_2CH_2$), 1.3-1.7 (m, 46H, CH_2), 0.96 (t, 15H, CH_3), 0.72 (t, 2H, RCH_2Si).

‡ *The hydrosilylation reaction using Karstedt's catalyst always produces a small amount of a side product as a result of the double bond migration (vinyl ⟶ allyl), which has proven impossible to remove by chromatography or recrystallization. However, in the*

silane-hydrolysis/condensation step with the MPS-capped GNRs, this impurity is non-reactive and is removed during the washing and isolation steps of the final DLC-GNRs. The trimethoxysilane-functionalized triphenylene derivative 4 also starts to react with itself (condensation reaction at ambient conditions – formation of a more and more viscous solid), which makes determining phase behavior and phase transition temperatures difficult.

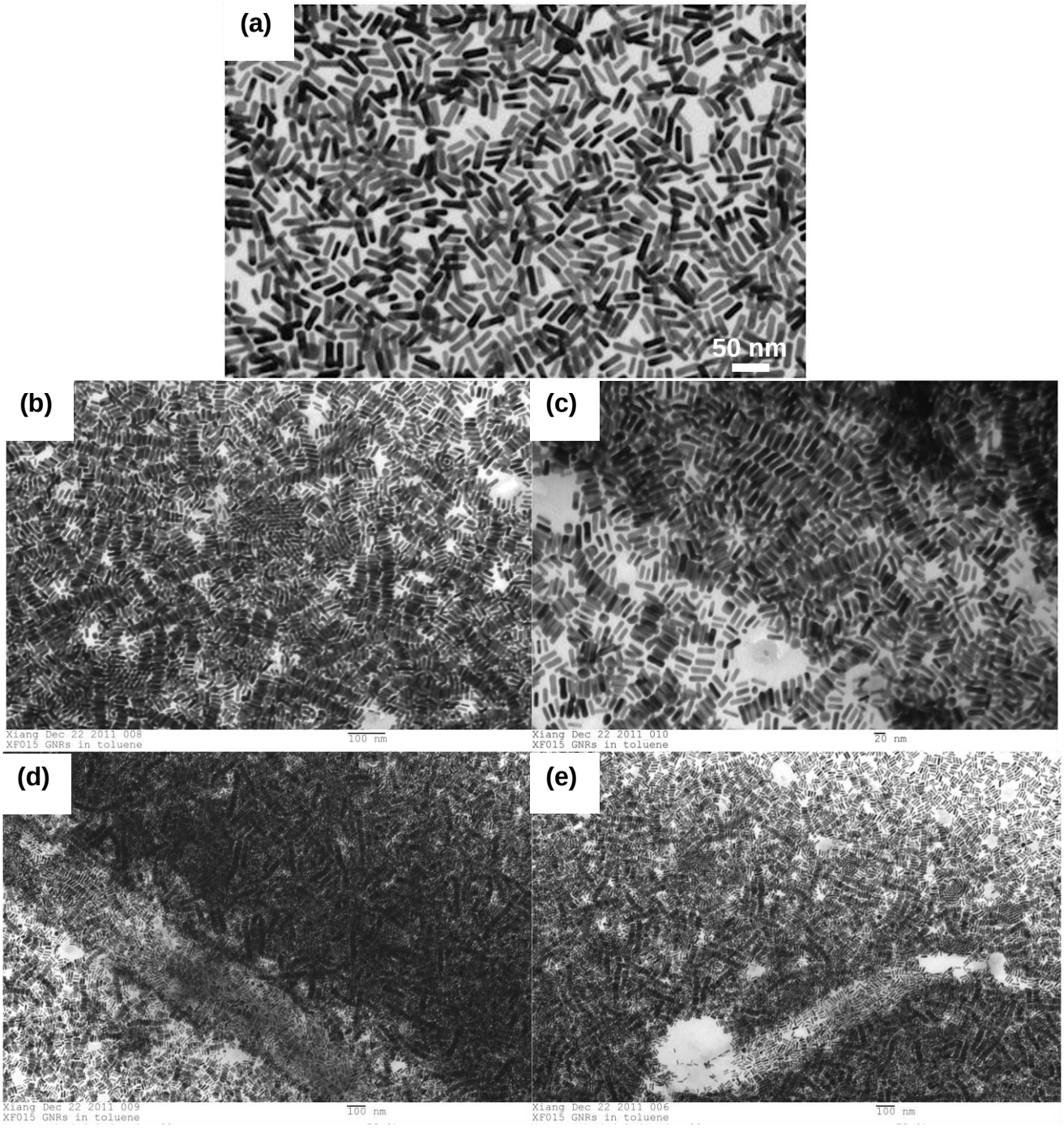

Figure B1. Representative TEM images: (a) TEM image showing the lack of long-range self-assembly or packing of the ODS-GNRs at the same concentration as the DLC-GNRs. At most 5 or 6 GNRs align parallel to one another in any section of the grids we tested with these GNRs. (b-e) Additional images for the DLC-GNRs showing the GNR ribbons.

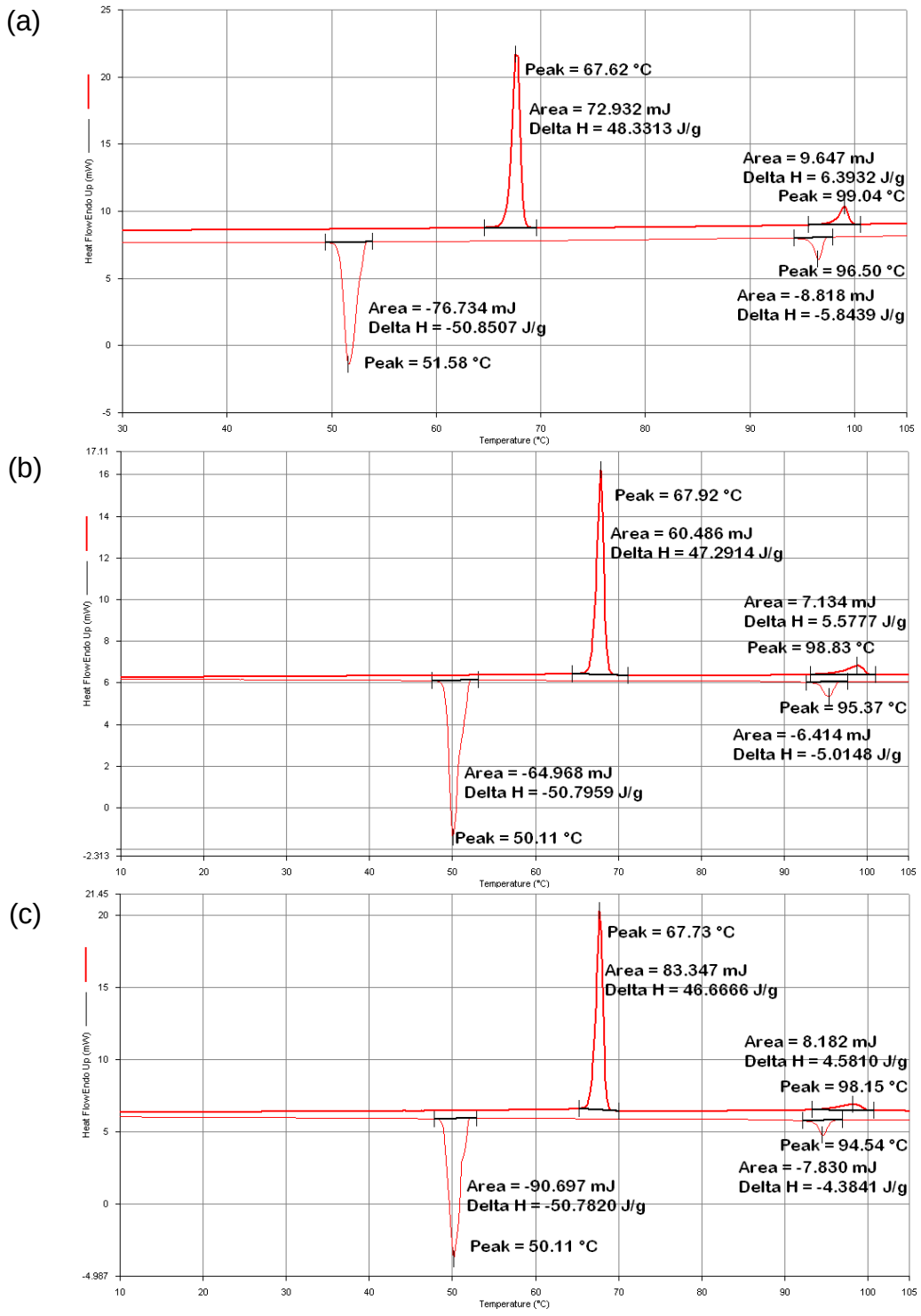

Figure B2. DSC traces of: (a) neat H6TP, (b) H6TP doped with 1 wt% DLC-GNRs, and (c) H6TP doped with 2 wt% DLC-GNRs.

Table B1. Phase transition temperatures and enthalpies of H4TP doped with 1 and 2 wt% DLC-GNRs. These closely match published values for neat H4TP.[B1]

	phase changes	T (°C)	ΔH (kJ/mol)	ΔS (J/mol/K)	sample
Heating	Cr→M1	86.9	26.6	73.8	1%
	M3→I	143.5	15.7	37.5	
	I→M1	143.9	22.6	54.0	
Cooling	M1→Cr	78.8	3.2	9.2	
	Cr→Cr'	49.7	22.0	80.4	
Heating	Cr→M1	87.2	26.3	72.7	2%
	M3→I	144.0	17.4	41.6	
	I→M1	144.2	22.8	54.6	
Cooling	M1→Cr	79.5	3.1	8.8	
	Cr→Cr'	64.5	23.0	67.9	

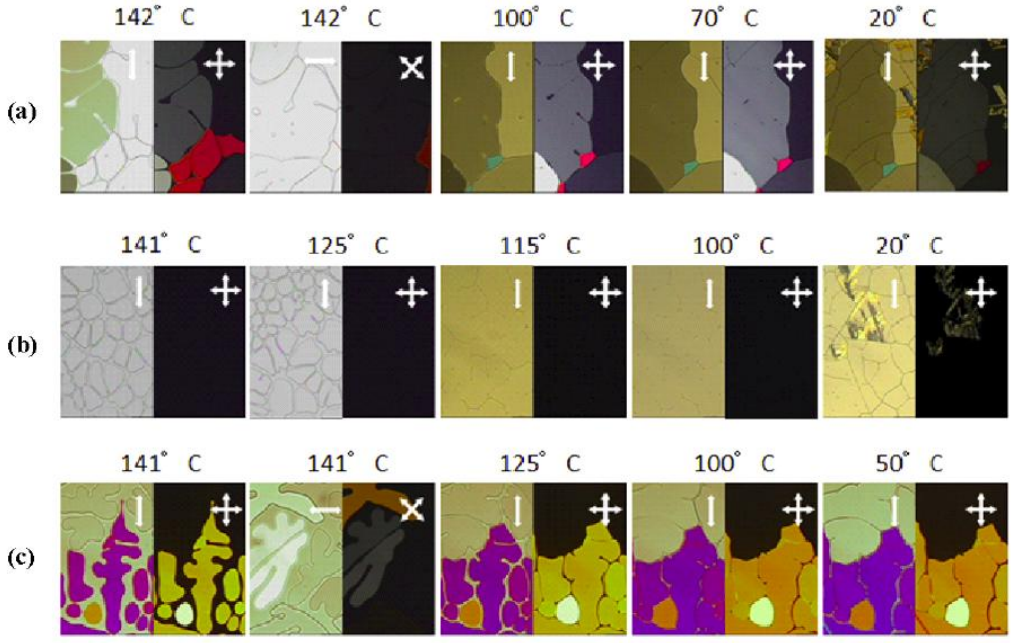

Figure B3. Textures observed under POM (left-open and right-cross polarizer) of the thin films of (a) undoped H4TP, (b) DLC-GNR/H4TP 1wt%, and (c) DLC-GNR/H4TP 2wt%. Spontaneous homeotropic alignment can clearly be observed for the 1wt% mixture.

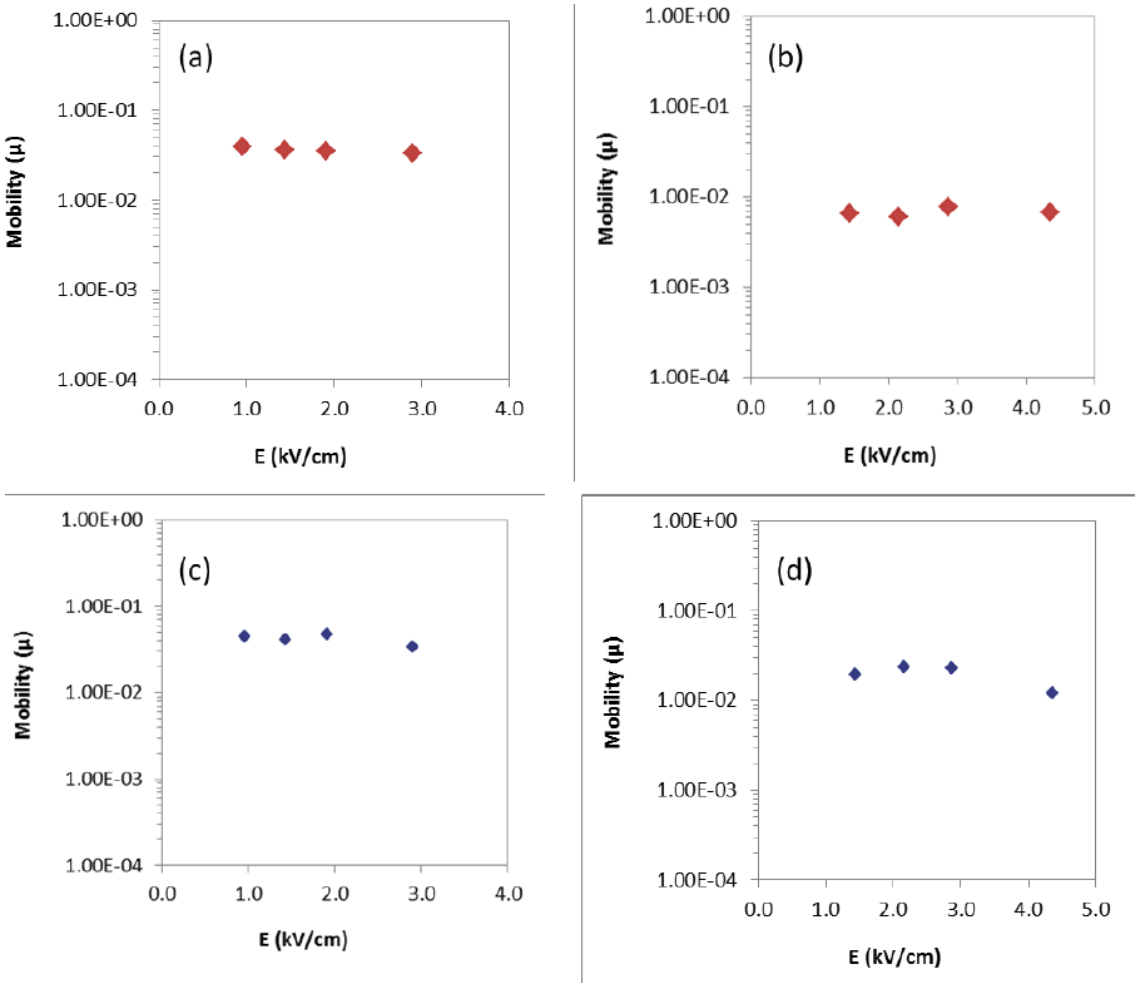

Figure B4. Effect of hole mobility upon increasing bias for: (a) H4TP doped with 1wt% **DLC-GNR**s, (b) H4TP doped with 2wt% **DLC-GNR**s, and effect of the electron mobility upon increasing the bias for: (c) H4TP doped with 1wt% **DLC-GNR**s, (d) H4TP doped with 2wt% **DLC-GNR**s.

(a)

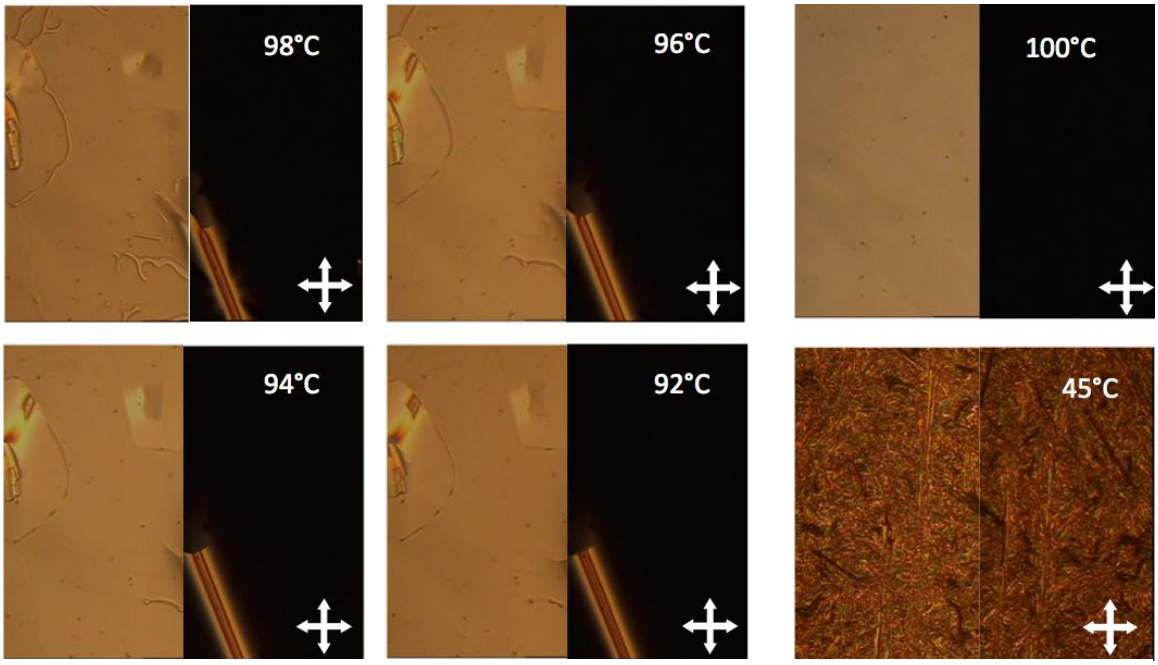

(b)

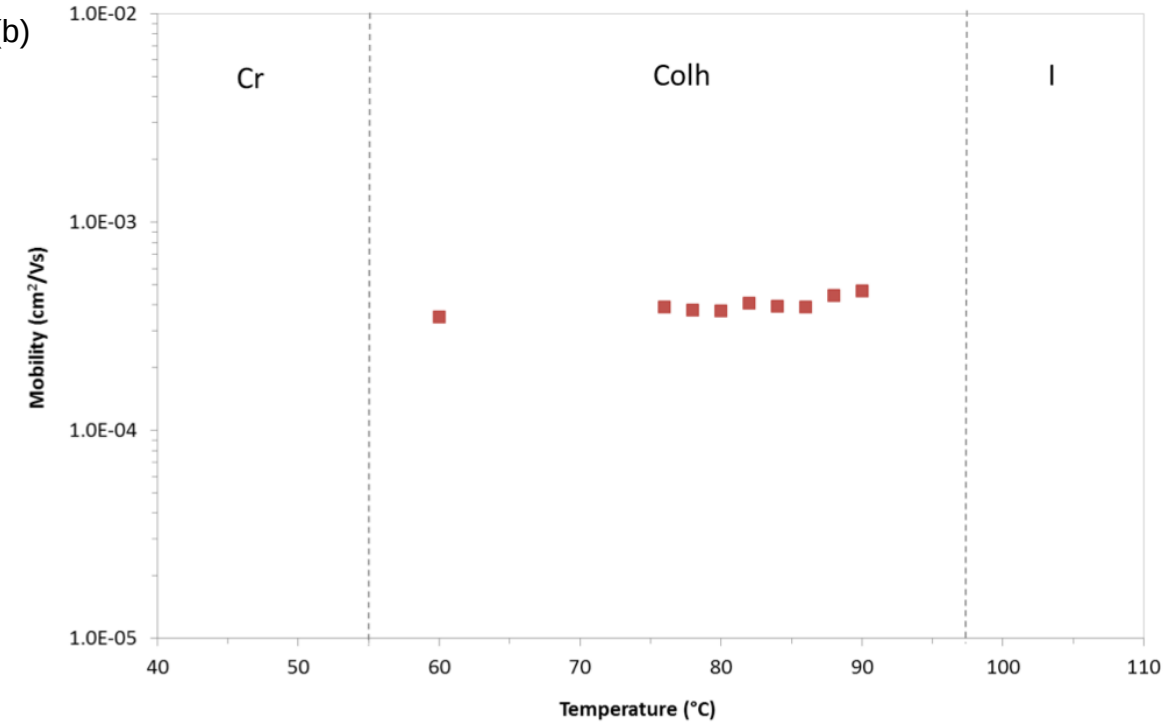

Figure B5. (a) Photomicrographs of textures observed under POM (left: uncrossed and right: crossed polarizers) in the crystalline solid (45 ℃), Col_{ho} phase (notice the much better homeotropic alignment for the less viscous H6TP), and at the isotropic liquid phase

(100 ℃). (b) Hole mobility in the Col_{ho} phase of H6TP over the entire mesophase range at about 2×10^{-4} cm^2/Vs measured in a ITO-coated cell with a cell gap of 12.4 μm.

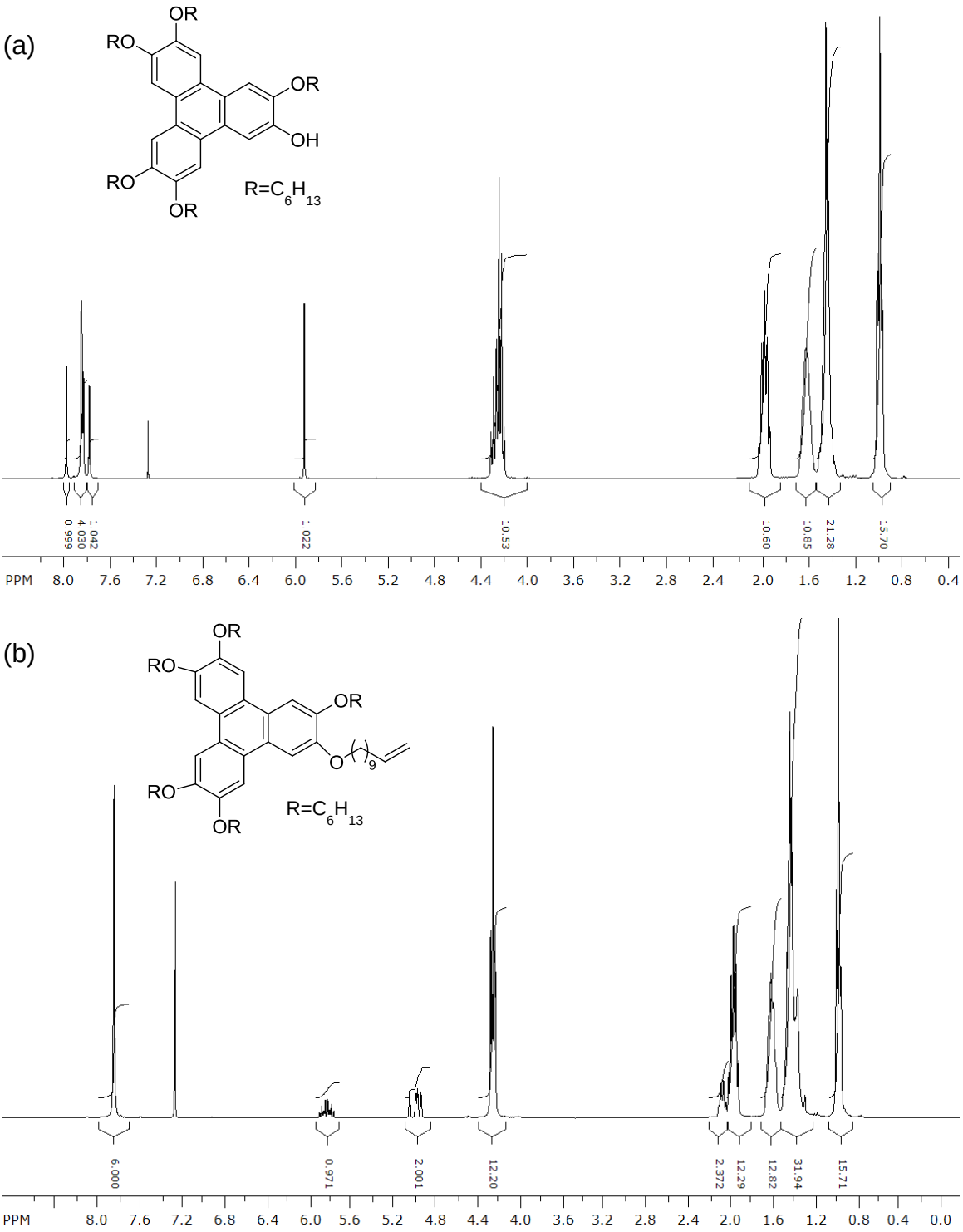

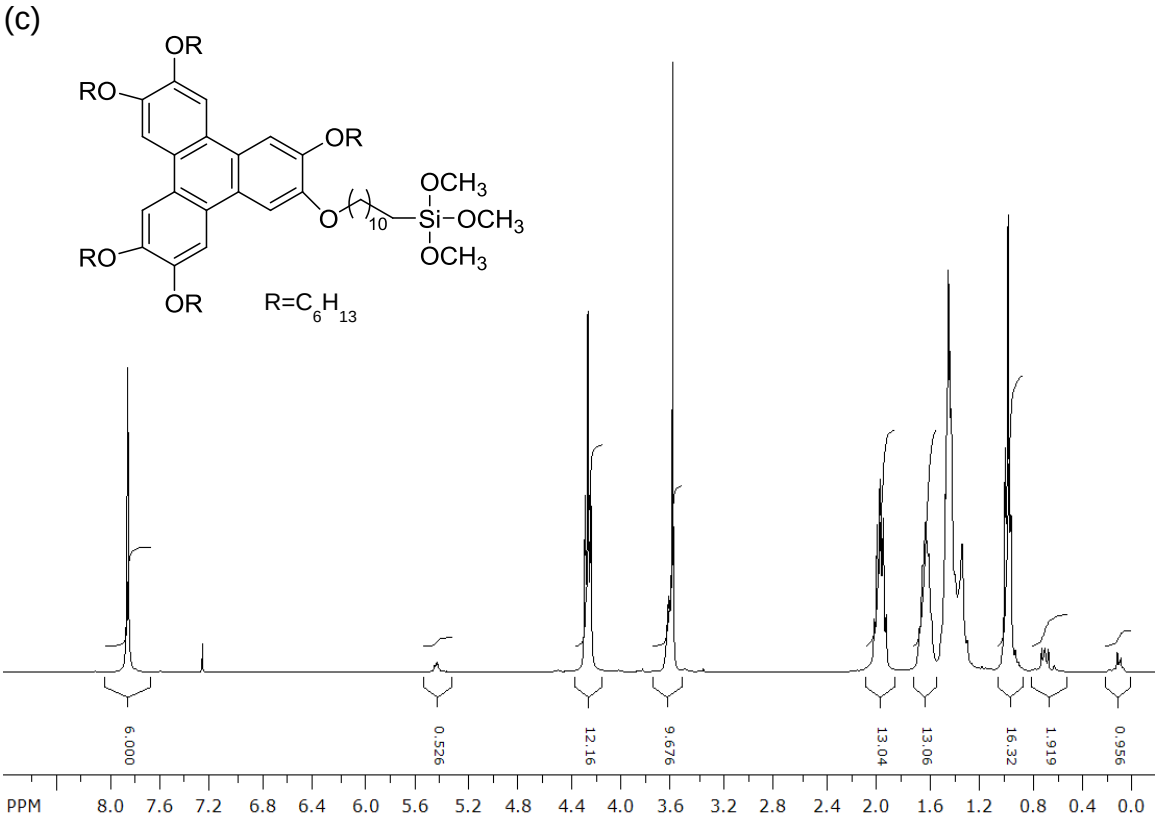

Figure B6. ^{1}H NMR spectra of compound: (a) **2**, (b) **3**, and (c) **4**.

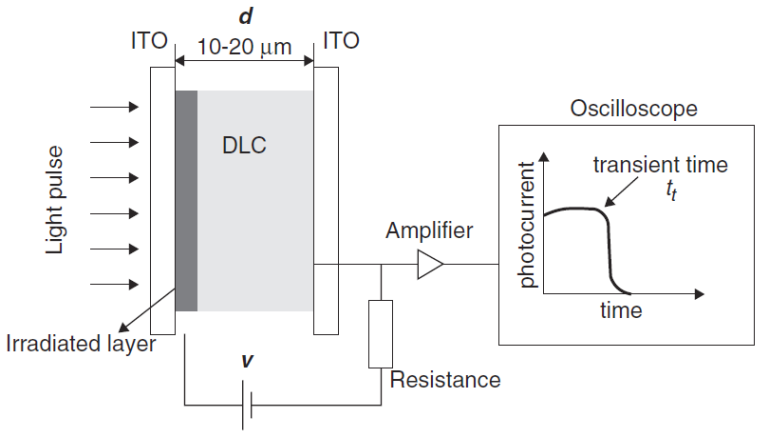

Figure B7. Schematic representation of the TOF experiment. The mobility μ depends on the applied voltage *V* and transit time t_t according to the equation $\mu = v/E = d^2/V t_t$, where v is the drift velocity, *d* is the film thickness, and *E* is the applied electric field. [B2]

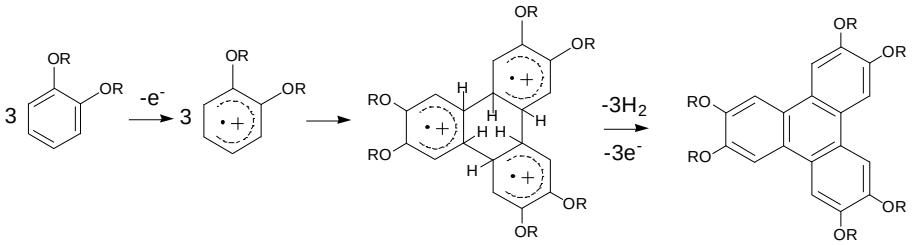

Figure B8. Radical mechanism of aromatic oxidative coupling reaction. [B3]

References:

[B1] H. Monobe, Y. Shimizu, S. Okamoto, H. Enomoto, *Mol. Cryst. Liq. Cryst.* **2007**, *476*, 31-41.

[B2] M. Mathews, Q. Li, *Self-Organized Discotic Liquid Crystals as Novel Organic Semiconductors*, pp. 90, In *Self-Orgnaized Organic Semiconductors – From Materials to Device Applications*, Q. Li, John Wiley & Sons, Inc., Hoboken, New Jersey **2011**.

[B3] M. Grzybowski, K. Skonieczny, H. Butenschön, D. T. Gryko, *Angew. Chem. Int. Ed.* **2013**, *52*, 9900-9930.

Chapter 4

Summary and outlook

The purpose of the work presented in this thesis is to demonstrate a versatile approach for the fabrication, functionalization and manipulation of hydrophobic inorganic nanoparticles with liquid crystal ligands. The assembly of nanoparticles, especially the ordered assembly of anisotropic nanoparticles, has risen as a technology challenge for advanced applications of nanomaterials, derived from collective properties of nanoparticles such as plasmon coupling, surface-enhanced Raman scattering, resonance energy transfer enhanced photoconductivity, negative refraction index and magnetic coupling.[1-6] The functionalized nanorods presented in this thesis possess enhanced self-assembly behavior in both monolayer and bulk conditions, and excellent dispersibility in many organic solvents and compounds (e.g. liquid crystals as discussed), which allow them to be further manipulated in organic media.

The contributions of this thesis to the field of nanorod self-assembly, as distinguished by chapters, can be described as two parts. The fabrication of nematic LC-functionalized GNRs, as presented in chapter 2, provided an effective approach for the self-assembly of nanorods. Two types of nematic LC functional groups were used, terminal LC (LC1) and lateral LC (LC2), corresponding respectively to LC ligands with the trimethyloxysilane anchoring group on the end of one terminal alkyl chain (parallel to the long molecular axis) or on the lateral side chain (perpendicular to the long molecular axis). Both LC1- and LC2- functionalized GNRs exhibit large area 3D self-assembly with nematic-like order, verified by TEM and SAXS. Plots of SAXS data also reveal a preferential packing mode of the nanorods, which are decided by the interaction of coated LC ligands. More importantly, the nematic LCs functionalized GNRs are demonstrated to be able to align under the stimulation of external magnetic field, which opens a new way for the manipu-

lation of non-magnetic nanostructures, although macroscopic alignment of ordered nanorods may need the assistance of a certain amount of mixed-in LC free molecules to increase the coupling energy between the LC ligands and the magnetic field.

Discotic LC functionalized GNRs also show enhanced large area self-assembly properties facilitated by discotic π-π stacking interaction. TEM and SAXS results verify monolayer and bulk side-by-side packing mode of DLC-GNRs, with the triphenylene motifs interdigitated with each other from different nanorod surfaces. The measured space distance from TEM and SAXS are consistent with the scale of the bi-molecular stack length. Here, along with nematic LC-GNRs, the demonstrated tunable space distance decided by the coating molecules is a promising direction for achieving space-determined collective effects of nanoparticles [7-9]. More importantly, macroscopic alignment of GNRs doped into thermotropic LC media has been achieved for the first time as determined by polarized UV-Vis-NIR. The planar alignment is realized through a simple and commonly used mechanical shearing of a DLC cell. One of the key factors of the prerequisites of this co-alignment is the homogeneous dispersion of DLC-GNRs in the parent DLC. Triphenylene based DLCs used in this work turn out to be an excellent and stable host for the DLC-GNRs compared with their nematic counterparts. The concentration of DLC-GNRs can go up to 2% by weight without showing any sign of aggregation. This highly stable and compatible mixture is attributed to the strong π-π stacking interaction and the higher viscosity of the mesophase. Interestingly, SAXS data reveal changes of lattice parameters of DLC after the insertion of GNRs. Unlike normally expected increasing values [10], both the inter-column and intra-column distance of the columnar phases decreased as much as 8%, which might be due to the phase compensation to the

packing mismatch created by the insertion of DLC-GNRs, leading to a larger degree of inter-digitation of the host molecules. The photocurrent conductivity measurements using a time-of-flight technique support a higher charge carrier mobility of the DLC-GNRs doped samples compared with the neat DLCs. It is not difficult to understand that with smaller intra-column distance and tighter overlapping of π orbitals, the hopping of charges along the DLC stacking columns should be much easier and faster.

Despite the systematic work presented in this thesis, there are still several aspects that could be addressed in future work. First, electro-optic tests of the mixtures of the nematic LC-GNRs doped into nematic and smectic LC phases could be performed. The Hegmann group demonstrated that spherical nanoparticle as additives modify the electro-optical properties of LCs to a significant extent. Yet, the effects of nanorod doping have not been investigated in the same detail. With the shape similarity of nanorods and calamitic LC host, the doping might create rather interesting properties.

Functionalization of nanorods with higher aspect ratios for alignment and manipulation purposes is also an interesting topic. Nanorods with higher aspect ratio should experience higher elastic torque in the LC host [11], which will facilitate the re-orientation in a highly predictable way.

The alignment of DLC-GNRs under the stimulation of magnetic fields should be a better way for the orientation of GNRs compared with the nematic LC functionalized GNRs because of the higher magnetic susceptibility or diamagnetic anisotropy of DLCs [12, 13]. Thus, a macroscopic co-alignment of DLC-GNRs doped DLC could be easily achieved through a magnetic field.

References

[1] M. Grzelczak, J. Vermant, E. M. Furst, L. M. Liz-Marzan, *ACS Nano* **2010**, *4*, 3591-3605.

[2] Y. J. Min, M. Akbulut, K. Kristiansen, Y. Golan, J. Israelachvili, *Nat. Mater.* **2008**, *7*, 527-538.

[3] Z. H. Nie, A. Petukhova, E. Kumacheva, *Nat. Nanotechnol.* **2010**, *5*, 15-25.

[4] S. Srivastava, N. A. Kotov, *Soft Matter* **2009**, *5*, 1146-1156.

[5] K. J. Stebe, E. Lewandowski, M. Ghosh, *Science* **2009**, *325*, 159-160.

[6] Y. N. Xia, Y. J. Xiong, B. Lim, S. E. Skrabalak, *Angew. Chem. Int. Edit.* **2009**, *48*, 60-103.

[7] K. H. Su, Q. H. Wei, X. Zhang, J. J. Mock, D. R. Smith, S. Schultz, *Nano Lett.* **2003**, *3*, 1087-1090.

[8] J. Aizpurua, G. W. Bryant, L. J. Richter, F. J. G. de Abajo, B. K. Kelley, T. Mallouk, *Phys. Rev. B* **2005**, *71*, 235420.

[9] V. M. Shalaev, W. S. Cai, U. K. Chettiar, H. K. Yuan, A. K. Sarychev, V. P. Drachev, A. V. Kildishev, *Opt. Lett.* **2005**, *30*, 3356-3358.

[10] S. Kumar, H. K. Bisoyi, *Angew. Chem. Int. Edit.* **2007**, *46*, 1501-1503.

[11] C. Lapointe, A. Hultgren, D. M. Silevitch, E. J. Felton, D. H. Reich, R. L. Leheny, *Science* **2004**, *303*, 652-655.

[12] J. H. Lee, S. M. Choi, B. D. Pate, M. H. Chisholm, Y. S. Han, *J. Mater. Chem.* **2006**, *16*, 2785-2791.

[13] B. R. Kaafarani, *Chem. Mater.* **2011**, *23*, 378-396.